MODELLING THE ONSET OF DYNAMIC FRICTION
A Study of Rupture Velocities

by

DAVID SKÅLID AMUNDSEN

THESIS

for the degree of

MASTER OF SCIENCE

(Master i Fysikk, studieretning Computational Physics)

Faculty of Mathematics and Natural Sciences
University of Oslo

June 2011

Det matematisk-naturvitenskapelige fakultet
Universitetet i Oslo

Abstract

The onset of dynamic dry friction between two blocks of PMMA has recently been studied experimentally. Technological advances enable the study of the onset of sliding at high temporal resolutions, resulting in new insights regarding how slip occurs at a local scale along the interface. In this thesis, spring-block models are used to study the onset of dynamic dry friction. These models have been used to study earthquakes for a long time, and have later been adopted to study friction on a laboratory scale. The agreement with the mentioned experimental results has, however, up until now been rather poor.

In these models, which are fully resolved in time, the local friction law has to be imposed. Using a local Amontons–Coulomb friction law, the one-dimensional model shows qualitative agreement with the experimental results. A quantitative comparison, however, reveals serious discrepancies. Studies reveal the importance of dimensionality to the kinetics, i.e. the states where slip nucleates and arrests, of the system. An example is the length of precursors as a function of the applied tangential load, which appears to be improved by including two-dimensional effects in the one-dimensional model.

Both dimensionality and the local friction law are seen to be crucial for the dynamics of the system, e.g. micro-slip front propagation. In the one-dimensional model, a specific relationship between the rupture velocity, the initial shear to normal stress ratio and the local friction coefficients is derived. This reveals the importance of the interfacial strength to the rupture velocities in addition to the stress ratio which has been suggested in the experimental papers.

A (2 + 0)D model, where both horizontal dimensions of the system are included, is also studied. It is shown that details of how the driving force is applied are crucial. As an illustration, a precursor has in a (2 + 0)D system both a length and a size. The development of these two quantities as a function of the applied tangential load can significantly deviate from each other depending on how the driving force is applied. The lack of experimental results studying these effects, however, makes the analysis difficult.

Acknowledgements

I would first and foremost like to thank my two supervisors, Prof Anders Malthe-Sørenssen and Dr Julien Scheibert. They have provided excellent advice and feedback through the whole year, and I am truly grateful for their help and support. I would also like to thank them for our trip to Lyon in March 2011, where we got to present our work at LTDS and attend a talk by Prof Jay Fineberg.

I am also very grateful to all the people at LTDS for letting us visit them and present our work. That they also took the time to show us what they are doing is highly appreciated.

I would also like to thank Kay Jörg Wiese from LPT, ENS in Paris for discussions about the calculation of rupture velocities in the one-dimensional model.

I also thank my fellow Master's students Kjetil Thøgersen and Jørgen Trømborg. We have worked closely together for the past year, and through our cooperation and discussions, I have learned much more than I could have managed on my own.

Last, but not least, I thank my family for their unabated support through my whole life.

Oslo, 1 June, 2011
David Skålid Amundsen

Contents

Abstract **3**

Acknowledgements **5**

List of symbols **11**

1 Introduction **13**
1.1 Motivation 13
1.2 The structure of this thesis 14

2 Background **17**
2.1 Introduction to dry friction 17
2.1.1 A short history of dry friction 17
2.1.2 The microscopic picture 18
2.1.3 Friction laws 20
2.1.4 Steady sliding and stick-slip 21
2.2 Stress, strain and elastic moduli 22
2.2.1 Stress and strain: Young's modulus 22
2.2.2 Poisson's ratio 23
2.2.3 Some additional remarks 24
2.3 Solving ODEs numerically 24
2.3.1 The Euler method 25
2.3.2 The fourth order Runge–Kutta method 25

3 Friction experiments and modelling today **27**
3.1 Experimental setup 27
3.2 Experimental results 29
3.3 Modelling activity and open questions 33

4 The one-dimensional spring-block model **35**
4.1 The one-dimensional model with side driving 36
4.2 Spring constants, normal loading and local friction 37
4.2.1 Choosing the material spring constant: Young's modulus 37
4.2.2 Non-uniform normal loading 38
4.2.3 The local friction law 39
4.3 The initial condition 39
4.4 Analytical analysis of the one-block model 40
4.5 First model results 42

4.5.1 Verification of the code . . . 42
4.5.2 Oscillations and viscous damping . . . 43
4.5.3 Stick-slip behaviour . . . 45
4.5.4 Shear force profile . . . 48
4.6 Precursor lengths . . . 49
4.6.1 Comparison between the model and experimental results . . . 49
4.6.2 Prediction of the length of a precursor . . . 50
4.7 Time dependence of slip . . . 52
4.8 Rupture velocities . . . 52
4.9 Shear torque . . . 54
4.9.1 Theoretical background . . . 55
4.9.2 The effect of shear torque on the length of precursors . . . 56
4.10 Initial shear force profile . . . 57
4.11 Scaling with the number of blocks . . . 58
4.12 The one-dimensional model with top driving . . . 60
4.13 First model results . . . 61
4.13.1 Stick-slip behaviour . . . 61
4.13.2 Shear force profile . . . 63
4.14 Precursor lengths . . . 64
4.14.1 Model results . . . 64
4.14.2 Prediction of the length of a precursor . . . 64
4.15 Rupture velocities . . . 65
4.16 Scaling with the number of blocks . . . 68
4.17 Robustness of the results . . . 68
4.18 Summary and conclusion . . . 69

5 Rupture velocities 71
5.1 Uniform prestress . . . 72
5.1.1 Simulation results . . . 72
5.1.2 Analytical calculation . . . 75
5.2 Non-uniform prestress . . . 82
5.2.1 Discrete jumps in the initial state of the interface . . . 82
5.2.2 Continuous variations in the initial state of the interface . . . 82
5.3 Special case: all blocks at the dynamic friction level . . . 86
5.3.1 Numerical results . . . 86
5.3.2 Analytical calculation . . . 86
5.4 Summary and conclusion . . . 90

6 Two new local friction laws 93
6.1 The spring-to-track static friction law . . . 93
6.1.1 Motivation . . . 93
6.1.2 The model . . . 94
6.1.3 Solving the static equations . . . 95
6.1.4 Verification and consequences . . . 97
6.1.5 Summary and conclusion . . . 100
6.2 A viscous dynamic friction law . . . 101
6.2.1 Motivation . . . 101
6.2.2 The one block model . . . 102
6.2.3 In a chain of blocks . . . 104

6.2.4 Comparison with experimental viscosities . . . 105
6.2.5 Consequences to the global behaviour . . . 106
6.2.6 Summary and conclusion . . . 108

7 The (2 + 0)D spring-block model 111
7.1 The model . . . 112
7.2 Driving . . . 113
7.3 Choosing the spring constants: Young's modulus and Poisson's ratio . . . 115
7.4 Oscillations and relative viscous damping . . . 115
7.5 First model results . . . 116
7.5.1 Verification of the code . . . 116
7.5.2 Verification of Young's modulus and Poisson's ratio . . . 116
7.5.3 Stick-slip behaviour . . . 118
7.5.4 Shear force profile . . . 118
7.6 Length and size of precursors . . . 121
7.7 System size and two-dimensional effects . . . 122
7.8 Robustness of the results . . . 122
7.9 Summary and conclusion . . . 123

8 Summary and conclusions 125
8.1 Summary . . . 125
8.2 Alternative approaches and future research . . . 127
8.3 Conclusions and ending remarks . . . 128

A Additional details of the one-dimensional model 131
A.1 Relative viscous damping . . . 131
A.1.1 Viscous damping in a one block system . . . 131
A.1.2 Relative viscous damping in a chain of blocks . . . 132
A.2 Numerical aspects . . . 133
A.2.1 Integration time step and scaling . . . 134
A.2.2 How to start and stop a block moving on a 1D surface . . . 134
A.2.3 Skipping simulation of stick in intervals . . . 135

B Additional details of the (2 + 0)D model 137
B.1 Calculation of Young's modulus and Poisson's ratio . . . 137
B.2 Numerical aspects . . . 139
B.2.1 Integration time step and scaling . . . 139
B.2.2 How to start and stop a block moving on a 2D surface . . . 139
B.2.3 Skipping simulation of stick intervals . . . 140
B.2.4 Symmetry and numerical errors . . . 141

List of symbols

α	Absolute viscosity	102
α_{III}	Absolute viscosity in phase III with the new viscous dynamic friction law	102
α_{II}	Absolute viscosity in phase II with the new viscous dynamic friction law	102
$\bar{\tau}$	Dimensionless, scaled initial stress ratio	73
δt	Time between the triggering of two neighbouring blocks	78
δ	Local slip	32
η	Relative viscous damping coefficient	37
μ	General friction coefficient	19
μ_d	Dynamic friction coefficient	20
μ_s	Static friction coefficient	20
ρ	Mass density	77
σ	Local normal stress	32
τ	Local shear stress	32
τ_c	Characteristic time in transition from α_{II} to α_{III}	102
θ	Imposed degree of non-uniformity in w_n	39
$\tilde{u}_n$	Transformed position of block n	77
$\mathbf{f}_n$	Friction force on block n in the (2 + 0)D model	113
$\mathbf{F}_n^K$	Driving force on block n in the (2 + 0)D model	113
$\mathbf{r}_n$	Position vector of block n in the (2 + 0)D model	113
$\mathbf{r}_n^0$	Initial position of block n in the (2 + 0)D model	114
$\mathbf{V}$	Driving velocity vector in the (2 + 0)D model	114
$\mathbf{v}_n$	Velocity vector of block n in the (2 + 0)D model	113
A	General macroscopic area	18
a	Lattice spacing in the 1D model	37
A_r	Real contact area	18
c_L	Longitudinal wave speed	32
c_R	Rayleigh wave speed	32
c_S	Shear wave speed	32
E	Young's modulus	23
ν	Poisson ratio	23
$F_\perp$	Force applied orthogonally to a surface	22
F_f	Total friction force	18
f_n	Friction force on block n in the 1D model	36
F_n^η	Relative viscous damping force on block n in the 1D model	37
$F_n^{\mathrm{n.f.}}$	Shear force on block n in the 1D model	37
f_n^d	Dynamic friction force on block n in the 1D model	39
F_n^K	Driving force on block n in the 1D model	36
f_n^s	Static friction force on block n in the 1D model	39

F_X	Applied driving force	18
F_Z	Applied normal load	28
g	Degree of non-uniformity in w_n due to shear torque in the 1D model	54
h	The height at which the tangential load is applied	55
K	Driving spring constant	29
k	Material spring constant in the 1D model	36
k	Material spring constant, nearest neighbours in the (2 + 0)D model	112
k'	Material spring constant, next-nearest neighbours in the (2 + 0)D model	112
K_n	Driving spring constant of driving spring connected to block n	37
k_t	Spring constant of spring connecting one block to the track	94
L	Length of object along one dimension	22
l_0	Characteristic length used with the spring-to-track static friction law	94
l_1	Equilibrium distance to nearest neighbours in the (2 + 0)D model	113
l_2	Equilibrium distance to next-nearest neighbours in the (2 + 0)D model	113
L_p	Length of precursors	30
M	Total slider mass	36
m	Mass of one block	36
N	Total number of blocks	36
N_{sliding}	Number of sliding blocks	46
N_d	Number of driven blocks	114
n_p	Length of precursor in block number in the 1D model	51
N_x	Number of blocks in the x-direction in the (2 + 0)D model	113
N_y	Number of blocks in the y-direction in the (2 + 0)D model	113
s	Degree of non-zero initial shear force in the 1D model	57
t	Time	24
Δt	Integration time step	25
t_c	Cooling time	102
u_n	Position of block n relative to its equilibrium position in the 1D model	36
u'_n	Position of block n relative to its initial position	76
V	Velocity of driving point	29
v	Velocity of a block	18
v_c	Rupture velocity in the 1D model	53
v_s	Velocity of sound in the 1D model	53
W	Total normal force	18
w, w_n	Normal force on each block	36

Chapter 1

Introduction

Friction is the resistance encountered by a surface or object when moving over another. It is a part of the broader field of tribology, defined as '... The science and technology of interacting surfaces in relative motion and the practices related thereto.' [27]. The focus of this thesis is modelling dry friction, i.e. friction between two solid surfaces in contact. Other types of friction usually involve gases or liquids, e.g. the motion of a solid object through a gas or fluid (skin friction), or the relative motion of two solid objects separated by a fluid (lubricated friction).

1.1 Motivation

Most people have an idea of what friction is, and it's such a common phenomenon that we can easily take it for granted. However, friction is important in almost every aspect of our lives: it's responsible for our ability to walk by pushing our body forwards with our feet and crucial for bees sitting on a flower petal. In machines, low friction (e.g. in the engine of the car where parts are moving fast relative to each other) or high friction (e.g. between the wheels of a car and the asphalt) may be desired. Friction is also related to wear, the damage and erosion by friction or use, which is important in both nature and engineering.

Another example of a phenomenon where friction is important is earthquakes. The similarities between a frictional behaviour seen in the lab called stick-slip, where two surfaces in contact alternate between sticking and sliding, and earthquakes was realised by Bryce and Byerlee in 1966 [11]. The short time intervals where there are relative movement between the surfaces are thought of as small earthquakes, where potential energy which has been built up with time is released. After this realisation, much work has gone into understanding the nature of these instabilities and under what conditions they occur. Earthquakes can have enormously devastating consequences, but if an earthquake could in some way be predicted, many lives could be saved and the damage could be limited. These are only some examples where understanding the origin of friction is crucial.

Friction is caused by electromagnetic interactions between atoms and molecules. Because of the complexity of these interactions, calculating friction from first principles is as of yet impossible. In applications, empirical friction laws are therefore used instead. In dry

friction these empirical laws have been more or less unchanged for the last 200 years, but there are still many unanswered questions [57]:

- Why is static friction so universally observed between solid objects?
- What is the exact relation between friction and wear?
- How are static and dynamic friction and the transition between the two related to microscopic atomic, asperity and grain interactions?
- Is static and dynamic friction marked by different phases of the interfaces?
- Is there some hidden information in the chaotic motion that can be used for e.g. earthquake prediction?
- How is friction best controlled? Can materials be designed to have certain frictional properties?

What makes friction an even more interesting field of study is its complexity. As mentioned, friction originates in electromagnetic interactions at the nanometre level. However, due to the complexity of these interactions, a model of two surfaces in frictional contact at the atomic level cannot be used to model surfaces visible to the naked eye. The computational effort is too great. Different models then have to be developed at different scales. These models should then be related to each other in some way, together comprising a more complete picture of the frictional process.

Due to the availability of new experimental techniques in recent years, there has been an increased interest in experimental activity regarding friction. As new observations are made, new questions arise that need to be answered. This has caused an increased modelling activity: attempts are made to reproduce and understand experimental results using simplified models [16, 37]. Theoretical approaches more focused on bridging the gap between the atomic scale and the continuum limit are also made [30]. Experimental and theoretical activities are the two main driving forces behind research, and one cannot live without the other. It is essential to link theoretical activity to real observations, and vice versa.

1.2 The structure of this thesis

In this thesis, spring-block models are used to study dry friction. Results are compared to recent experimental results, and further insight into the experiments is gained. Answers to the fundamental questions posed above were not found, but that was not the goal of this work, either. This thesis is one of three Master's theses on this subject completed the spring of 2011 at the University of Oslo.

The second chapter deals with the necessary background material on friction, which includes a short introduction to dry friction, simple elasticity theory and the numerical solution scheme used. The present state of friction experiments and modelling are then presented in chapter 3, where the focus is on the activity of direct relevance to the rest of this thesis.

In chapter 4 a one-dimensional model is introduced. Even though the model is simple, it is shown to exhibit quite complex behaviour. The model results are compared to the

experimental results, and this leads to further investigation of the rupture phenomenon, which is the topic of chapter 5. An improved static friction law and an attempt at improving the dynamic friction law are presented in chapter 6. In chapter 7, a two-dimensional model is introduced, and chapter 8 then summarises the new insights gained from all the model results.

Chapter 2

Background

In this chapter, the background material for this thesis is presented. First, a short introduction to dry friction is given, where the emphasis is on the parts that are relevant for the work presented here. This part is mainly based on [2, 42, 51].

Then some basic elasticity theory is presented. Some knowledge in this field is needed later in order to make the models used in this thesis physically reasonable. This part is mainly based on [54, 59]. The last section of this chapter introduces the numerical solution scheme used to solve the equations of motion for the models that are introduced later. This part is mainly based on [36].

2.1 Introduction to dry friction

This section begins with a short historical introduction to dry friction. For a more comprehensive presentation, the reader is referred to the book by Dawson [27]. The current microscopic picture of the mechanism of friction due to Bowden and Tabor [10] will then be discussed, followed by a short discussion of different friction laws used in dry friction.

2.1.1 A short history of dry friction

The use of friction as a tool to accomplish means such as creating a fire by rubbing two wooden blocks together, dates back about 200,000 years. It may not even be humans who came up with the idea first: the Neanderthals managed to create fires this way, clearly showing the beginning of a qualitative understanding of the friction phenomena.

Another example is the Egyptians, who about 4,000 years ago used lubricants in order to more easily move heavy stone objects. A painting showing this process has been found in the tomb of Tehuti-Hetep, El-Bershed, clearly showing a person pouring a liquid on the ground right in front of a statue being towed by a considerable number of men. The manipulation and utilisation of the frictional process is therefore not new, but a more quantitative understanding dates back to the work by da Vinci in the 16th century.

Da Vinci wrote that [10]

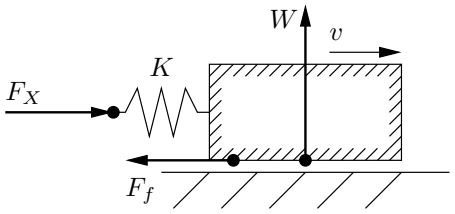

Figure 2.1: A block sliding on a surface with velocity v due to an applied force F_X. W is the normal force, and F_f is the friction force. If the velocity is constant, $F_f = -F_X$.

1. 'Friction produces double the amount of effort if the weight be doubled.'
2. 'The friction made by the same weight will be of equal resistance at the beginning of the movement although the contact may be of different breadths of lengths.'

Since the term "force" was not yet well defined (Isaac Newton resolved this in the 17th century, almost 200 years later), the wording may seem a little strange by modern standards. However, the two passages clearly indicate an understanding of what is today called the Amontons–Coulomb laws of friction.

Figure 2.1 shows a typical sketch illustrating dry friction. A block experiencing a normal force W slides on a surface with velocity v due to a force F_X applied through a spring with spring constant K. The block will then also experience a friction force F_f directed opposite to the direction of motion. If the velocity v is constant, then $F_f = -F_X$.

In the late 17th century, the French engineer Guillaume Amontons rediscovered the observations made by da Vinci. Namely, that the friction force is proportional to the normal force, and that the friction force is independent of the (apparent) area of contact between two bodies. These observations were met with scepticism in the scientific community because there was no generally accepted explanation for them.

In the late 18th century, Charles Augustin Coulomb, best known for his contributions to electromagnetism, verified Amontons results and also made the distinction between static (the force required to initiate motion) and dynamic (the force required to sustain a constant velocity) friction. In addition he also noticed that the static friction force appears to increase with time. The generally accepted explanation for these results is usually credited to Bowden and Tabor [10], who explained the macroscopic laws of friction by a microscopic picture of contacts and the breaking of these contacts.

2.1.2 The microscopic picture

Bowden and Tabor imagined all real surfaces as being rough on a microscopic scale, with the protrusions on the surface called asperities, see Figure 2.2. When two such surfaces are brought into contact, they will not be in contact over the whole interface of area A, but only at a few points or asperities. The real area of contact, A_r, is therefore usually much smaller than the apparent area of contact A, and it is the real area of contact that is responsible for friction.

By introducing the real area of contact, Bowden and Tabor were able to explain the Amontons–Coulomb laws of friction through a rather simple model. They said that, as two rough surfaces are pressed together, the real area of contact grows until it is high enough to sustain the normal load. By assuming that the asperities yield plastically, the relation

$$W = pA_r, \tag{2.1}$$

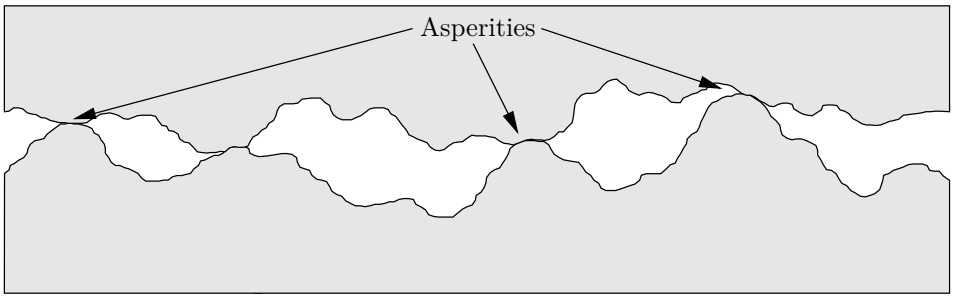

Figure 2.2: Schematic illustration of two rough surfaces in frictional contact. The real area of contact A_r between these two surfaces will dominate the frictional behaviour.

where W is the normal force and p is the penetration hardness, which is then a measure of the strength of the material, holds.

Since the normal force must be supported by the relatively small real area of contact, it is natural to assume that the pressure on these points will be high. Bowden and Tabor imagined that adhesion occurred at these points, making the interlocking asperities stick to each other. For any significant motion to occur, these junctions must be sheared through. The frictional force is then proportional to the real area of contact,

$$F_f = sA_r, \tag{2.2}$$

where F_f is the friction force and s is a measure of the shear strength of the interface. Combining these two results, a coefficient of friction μ can be defined as

$$\mu = F_f/W = p/s, \tag{2.3}$$

and the friction law can now be stated as

$$F_f = \mu W, \tag{2.4}$$

which says that the friction force is proportional to the normal force with a factor of proportionality μ. This is consistent with da Vinci's first observation, although he did not use the term "force". Da Vinci's second observation is also explained by this picture, because the friction force is not determined by the apparent area of contact. It is the real area of contact that is important, and the real area of contact is proportional to the normal load and independent of the apparent area of contact.

This picture is, however, not complete. For example, inserting realistic values for p and s often leads to predictions of μ that are significantly different from the measured values [51]. There are several reasons for this, and they all originate in the fact that the above presented picture is too simple. For example, the real area of contact may increase with shearing, and the linearity in equation (2.2) may not hold if asperities do not yield plastically but instead by e.g. brittle fracture.

The Bowden and Tabor picture may then only serve as a conceptual framework, and it is important to keep in mind that alternations and modifications will be necessary in order to obtain a complete description of friction. Despite this, it both explains what is now called Amontons–Coulomb's laws of friction and gives very useful insights into the microscopic processes that are responsible for friction. It has also been shown [31] that the above picture is valid if the asperities deform purely elastically. This offers further support to the validity of the Amontons–Coulomb laws of friction for a broad range of materials.

2.1.3 Friction laws

As stated above, the friction laws observed by da Vinci were rediscovered and extended by Amontons and Coulomb. These laws are today known as the Amontons–Coulomb laws of friction, and can be stated as follows [2]:

- No motion occurs as long as F_X, the applied tangential force, is smaller than a finite threshold $\mu_s W$, where W is the normal force. μ_s is the constant of proportionality usually called the static coefficient of friction.
- The friction force is independent of the apparent area of contact.
- When motion occurs, the friction force is also proportional to the normal load, and equal to $\mu_d W$, where W again is the normal force. μ_d is the constant of proportionality usually called the dynamic coefficient of friction.

The dynamic and static friction coefficients, μ_d and μ_s, are in general not equal. In most cases $\mu_s > \mu_d$. The Amontons–Coulomb laws of friction are strictly speaking only valid in cases of no sliding (static friction) and steady sliding (dynamic friction), and do not say anything about the how transition from no sliding to steady sliding back to no sliding occurs, but these transitions are usually considered to be fast. These laws are remarkably simple, and are in many situations a good enough description of friction for engineering purposes. However, deviations from Amontons–Coulomb's laws of friction are observed, and the most noticeable are:

- μ_s is not constant, but actually a slowly increasing function of the waiting time t_w defined as the duration of static contact before sliding is initiated. It is observed to increase logarithmically.
- In stationary sliding, μ_d is not constant either, but is actually a slowly decreasing function of the velocity for low enough velocities (typically less than 100 μm/s).

The first observation is due to an effect called ageing. Thermally activated contact growth causes the frictional strength of the interface to increase with time. The second observation can also be explained by ageing: for a lower velocity, contacts get more time to age before they are broken, and the frictional interface is therefore said to rejuvenate upon sliding.

Empirical friction laws have been developed in order to take into account the observed deviations from Amontons–Coulomb's laws of friction. These usually include a rate variable, usually the sliding velocity v, and a time dependent state variable ϑ. These laws are therefore called rate and state variable friction laws.

The rate and state friction law that best fits the experimental data at present is the Dieterich–Ruina law [51]:

$$\mu = \mu(v, \vartheta) = \mu_0 + \mathfrak{a} \ln\left(\frac{v}{v_0}\right) + \mathfrak{b} \ln\left(\frac{v_0 \vartheta}{d_c}\right), \tag{2.5}$$

$$\dot{\vartheta} = 1 - \frac{v\vartheta}{d_c}, \tag{2.6}$$

where v_0 is a characteristic velocity, d_c is a characteristic distance, and $\mathfrak{a}$ and $\mathfrak{b}$ are constants. In the static case $\vartheta = t$ from equation 2.6, which means that, provided $\mathfrak{b} > 0$, the static coefficient will increase logarithmically with time as observed in experiments.

According to equation (2.5), the friction force can be both velocity strengthening and weakening, and both these behaviours are observed.

It is mainly the Amontons–Coulomb laws of friction that are used in this thesis. However, it is important to keep in mind that modifications to these laws exist. Both the Amontons–Coulomb and rate and state dependent friction laws are averaged laws, meaning that they are only valid on a macroscopic scale: they describe the friction force on bodies visible to the naked eye. These laws can be extended to the mesoscopic scale, typically on the order of micro metres, where the number of asperities is still large.

The microscopic scale is the scale of the intermolecular interactions, and is the scale at which friction can be said to originate. The averaged friction laws discussed above is consequently not valid, because they need a large number of asperities to be averaged over. The interplay between the microscopic, mesoscopic and macroscopic scales in friction is still not completely understood. This is illustrated by the fact that empirical friction laws are used on a macroscopic scale. One goal of the research being done nowadays is to be to be able to calculate the coefficients of friction from first principles. This is much beyond the scope of this thesis, which will focus on the relationship between the mesoscopic and macroscopic scale.

2.1.4 Steady sliding and stick-slip

In experiments, three different kinds of frictional behaviours are observed depending on the details of how the force F_X is applied. Figure 2.1 depicts a system where a block is sliding on a surface with a velocity v, which may or may not be constant. The driving force F_X is applied at a point, which then moves at a constant velocity V. This point is the left end of the driving spring K, whose right end is attached to the block.

Three different behaviours are seen depending on the driving velocity V and the driving spring constant K:

- Steady sliding: After motion has initiated, the block moves with a constant velocity v, leading to a constant tangential force F_X. This behaviour is seen if the driving spring is stiff enough and/or the driving velocity is high enough.
- Periodic stick-slip: The block alternates between no motion (stick) and motion (slip) in a periodic way. The tangential force is seen to drop rapidly when the block moves, and increase linearly when it does not. This behaviour, as chaotic stick-slip, occurs if the driving spring is soft enough and the driving velocity is low enough.
- Chaotic stick-slip: The block alternates between no motion (stick) and motion (slip) in a chaotic way, but is in other aspects similar to periodic stick-slip. The chaotic behaviour may result from e.g. surface inhomogeneities.

An illustration of the tangential force F_X as a function of time, t, for these three cases is shown in Figure 2.3, with the general form of a kinetic phase diagram shown in Figure 2.4.

By applying the Amontons–Coulomb laws of friction to the system depicted in Figure 2.1, calculations (see section 4.4) show that regular stick-slip always occur, independently of how K and V are chosen. It is therefore easy to motivate that, as discussed

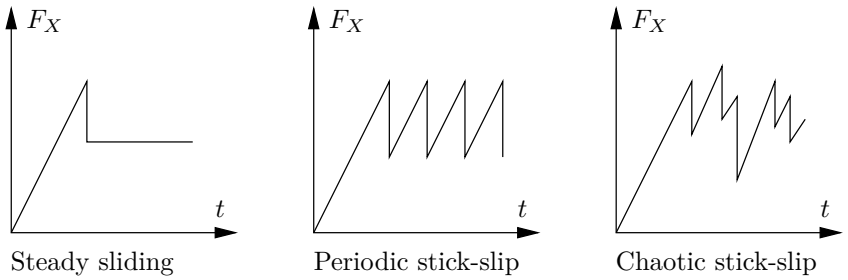

Figure 2.3: Schematic illustration of the applied tangential load as a function of time, $F_X(t)$, for steady sliding, periodic stick-slip and chaotic stick-slip.

Figure 2.4: The general form of a kinetic phase diagram. The grey area represents values for the driving spring constant K and driving velocity V which result in stick-slip behaviour.

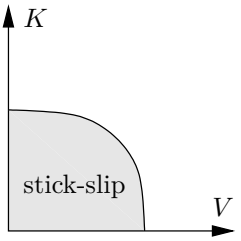

in the previous section, deviations from the Amontons–Coulomb laws of friction exist. Even though steady sliding is seen at the global level, stick-slip may occur locally along the interface between the block and the track, where surface asperities alternate between attaching and detaching. For more details on this subject, the reader is referred to [2, 42, 51].

This concludes the discussion of the theory of friction. The next section deals with the basic theory of elasticity, i.e. how materials behave under different kinds of loading. This will be needed later on in order to make physically reasonable models of the bulk of a block.

2.2 Stress, strain and elastic moduli

This section deals with how solid objects deform and become internally stressed due to an applied load, which in turn can give information about the interfacial stresses. The relationship between applied pressure, stress, and the corresponding deformation, strain, is discussed, but a detailed description will not be given. For a more comprehensive discussion, the reader is referred to the book by Timoshenko and Goodier [54].

2.2.1 Stress and strain: Young's modulus

The first type of stress introduced here is tensile stress. Figure 2.5 shows an object with sides of length L_x, L_y and L_z and a cross-sectional area A in the yz-plane. This area is then given by $A = L_y L_z$. A force $F_\perp$ is applied to each side perpendicular to the surfaces, as shown in the figure. These two forces are oppositely directed, which ensures that the object's centre of mass is stationary.

The tensile stress is then defined as the force per cross sectional area, $\sigma_x = F_\perp/A$, where the subscript x denotes that it is the stress on a side with the surface normal in the x-

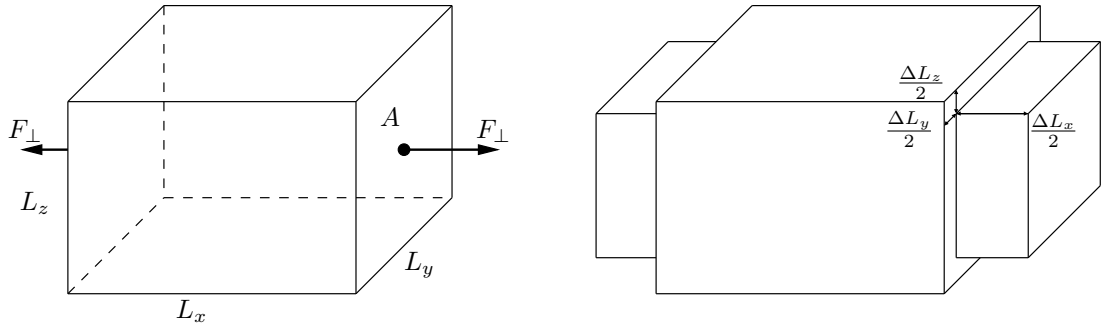

Figure 2.5: Schematic illustration of the deformation of an object subject to tensile stress. A force $F_\perp$ is applied to the sides with cross-section A (left), and this causes the dimensions of the object to change (right). Credit for this figure goes to Jørgen Trømborg.

direction. Correspondingly, stresses in the y- and z-direction are denoted by σ_y and σ_z, respectively. This will cause an elongation of the object in the direction perpendicular to the cross-sections and the corresponding elongation is denoted as ΔL_x, as illustrated in the right part of Figure 2.5. The tensile strain is defined as the relative change in length, given by $\epsilon_x = \Delta L_x / L_x$, where the subscript letter is used in the same way as for the stresses.

Here, only linear, isotropic elastic materials are considered. The relationship between stress and strain is then linear, and the constant of proportionality is independent of the direction of the applied load. For tensile and compressive stress and strain, this constant is called Young's modulus, defined by

$$\boxed{E = \frac{\sigma_x}{\epsilon_x} = \frac{F_\perp / A}{\Delta L_x / L} = \frac{F_\perp L_x}{A \Delta L_x}.} \tag{2.7}$$

There exist other kinds of deformations as well, and one of them is shear stress and strain. Shear stress arises when a load is applied tangentially to a surface, and this is what happens at the interface of two bodies in frictional contact. As seen in Figure 2.1, the friction force is acting tangentially on the lowermost surface, causing shear stress and consequently shear strain.

2.2.2 Poisson's ratio

When an object is under tensile or compressive stress, the object changes length in the direction of the applied load, as discussed above. The object will also change length in the two directions orthogonal to the applied load, as shown to the right in Figure 2.5. A simple example is incompressible materials, which given a compressive strain in one direction would have to expand in another in order to keep the volume constant. This is called the Poisson effect.

The relative change in length in the two orthogonal directions, $\epsilon_y = \Delta L_y / L_y$ and $\epsilon_z = \Delta L_z / L_z$ in Figure 2.5, are of equal size, and Poisson's ratio ν is given by

$$\boxed{\nu = -\frac{\epsilon_y}{\epsilon_x} = -\frac{\epsilon_z}{\epsilon_x}.} \tag{2.8}$$

2.2.3 Some additional remarks

This concludes the brief introduction of the behaviour of linear isotropic elastic materials. These materials will return to their original size when the load is removed. For real objects, this is true only for small deformations: if the deformations are too great, plastic deformations may occur, causing a permanent change in the object's dimensions. However, such deformations will not be studied here.

An additional remark should be made in order to avoid confusion later. In discrete models, such as the ones that will be used here, it may also be meaningful to talk about local forces instead of stresses. These forces then act on discrete objects or points, but can easily be converted to stresses by calculating the force per unit area.

2.3 Solving ODEs numerically

The models used here will, as so many other physical models, result in a set of differential equations. Solving these equations analytically in general will be extremely difficult, maybe impossible, and a numerical solution strategy is therefore used. In this section, the numerical method used to solve the differential equations describing the system is presented. Many other solution strategies exist, but the method discussed here is commonly used and well suited for the systems considered in this thesis.

First, the simple Euler method is presented. This method is used to introduce the fourth order Runge–Kutta method, which is the method used to obtain all results throughout this thesis. Many of the details will not be discussed here, and for a more comprehensive discussion the reader is referred to Numerical Recipes [43].

A first order ordinary differential equation is generally given by

$$\dot{u}(t) = f[t, u(t)]. \tag{2.9}$$

Of course, not all differential equations are of the first order. However, all N-th order differential equations can be rewritten in terms of N coupled first order differential equations. An example of this is the second order differential equation

$$\ddot{u}_1(t) + u_1(t) = 0, \tag{2.10}$$

where $\ddot{}$ denotes the second derivative with respect to t. The equations of motion describing the models used in this thesis are typically of second order. The equation above can be rewritten in terms of two coupled first order linear differential equations by introducing a new variable $u_2(t)$:

$$\begin{aligned} \dot{u}_1(t) &= u_2(t), \\ \dot{u}_2(t) &= -u_1(t). \end{aligned} \tag{2.11}$$

It is then sufficient to discuss the solution strategy for a system consisting of N linear differential equations on the form

$$\dot{u}_n(t) = f_n\left[t, u_1(t), u_2(t), \ldots, u_N(t)\right] = f_n\left[t, \{u(t)\}\right], \quad n = 1, 2, \ldots, N. \tag{2.12}$$

2.3.1 The Euler method

By considering the Taylor expansion

$$u_n(t+\Delta t) = u_n(t) + \frac{\dot{u}_n(t)}{1!}\Delta t + \frac{\ddot{u}_n(t)}{2!}\Delta t^2 + \cdots = \sum_{j=0}^{\infty} \frac{u_n^{(j)}(t)}{j!}\Delta t^j, \tag{2.13}$$

where $u_n^{(j)}(t)$ denotes the j-th derivative and Δt the chosen step size, one finds by ignoring higher order terms an equation for $u_n(t+\Delta t)$ by using that $\dot{u}_n(t) = f_n\left[t, \{u(t)\}\right]$, given by

$$u_n(t+\Delta t) = u_n(t) + f_n\left[t, \{u(t)\}\right]\Delta t + \mathcal{O}(\Delta t^2). \tag{2.14}$$

This is called Euler's method, and is a first order method, meaning that the local error is on the order of Δt^2, while the accumulated error is of order Δt. Knowing the initial condition, the solution to the differential equation can be found for integer time steps by using this formula. If Δt tends to zero, this will be an increasingly good approximation. However it turns out that this is a rather poor approximation because it tends to produce systematic errors in the solution [36]. For example, it can be shown that for a harmonic motion, Euler's method results in a solution that increases the energy of the system with time no matter how small Δt is chosen to be. In addition, Δt cannot in practice be chosen infinitely small both because of limited computer power and because for small enough Δt, loss of precision begins to dominate (the computer does not have enough significant digits to do the calculations). For these reasons, the fourth order Runge–Kutta-method is often preferred.

2.3.2 The fourth order Runge–Kutta method

The fourth order Runge–Kutta method is more complicated than the simple Euler's method, requiring more evaluations of the functions $f_n\left[t, \{u(t)\}\right]$. However, since it is a fourth order method, the error is significantly reduced for a given Δt compared to Euler's method. The fourth order Runge–Kutta method can be summed up in the following way:

$$\boxed{\begin{aligned} u_n(t+\Delta t) &= u_n(t) + \bar{k}_n\Delta t + \mathcal{O}(\Delta t^5), \\ \bar{k}_n &= \frac{1}{6}\left(k_n^{(1)} + 2k_n^{(2)} + 2k_n^{(3)} + k_n^{(4)}\right), \\ k_n^{(1)} &= f_n\left[t, \{u(t)\}\right], \\ k_n^{(2)} &= f_n\left[t + \Delta t/2, \left\{u(t) + k^{(1)}\Delta t/2\right\}\right], \\ k_n^{(3)} &= f_n\left[t + \Delta t/2, \left\{u(t) + k^{(2)}\Delta t/2\right\}\right], \\ k_n^{(4)} &= f_n\left[t + \Delta t, \left\{u(t) + k^{(3)}\Delta t\right\}\right], \end{aligned}} \tag{2.15}$$

where the short form notation

$$\left\{u(t) + k^{(1)}\Delta t/2\right\} = \begin{Bmatrix} u_1(t) + k_1^{(1)}\Delta t/2 \\ u_2(t) + k_2^{(1)}\Delta t/2 \\ \vdots \quad \vdots \quad \vdots \quad \vdots \\ u_N(t) + k_N^{(1)}\Delta t/2 \end{Bmatrix}$$

has been used, with similar notation for $k^{(2)}$, $k^{(3)}$ and $k^{(4)}$. At first sight, this may seem very complicated, but in reality it is not that difficult to understand.

First, the gradient of $\{u(t)\}$ is found at t, and stored in $k^{(1)}$. Second, an estimated gradient is found at $t + \Delta t/2$ by using Euler's method with $k^{(1)}$, which is stored in $k^{(2)}$. Third, a second estimated gradient at $t + \Delta t/2$ is found by using Euler's method with $k^{(2)}$, and is stored in $k^{(3)}$. Fourth, an estimated gradient at $t + \Delta t$ is found by using Euler's method with $k^{(3)}$, and is stored in $k^{(4)}$. All these estimates are calculated by starting at $(t, \{u(t)\})$.

Doing this, one has four gradients in the interval between t and $t + \Delta t$, $k^{(1)}$ to $k^{(4)}$. A weighted average $\bar{k}$ is then calculated, which is an estimated mean gradient in this interval. Euler's method is then used to go from $\{u(t)\}$ to $\{u(t + \Delta t)\}$ by using this mean gradient.

This procedure is then repeated until the value of $\{u(t)\}$ has been obtained for all integer time steps in the solution time interval. The local error is now on the order of Δt^5, meaning that the accumulated error is on the order of Δt^4, which for small Δt is much less than the error in the Euler method. It is because of the fact that the global error is of order Δt^4 that this method is called the fourth order Runge–Kutta method.

Chapter 3

Friction experiments and modelling today

In this chapter, the experiments and the experimental results that the models studied in this thesis are compared with are presented and discussed. However, only examples of the different experimental data available will be presented here, the specific plots that are used for the comparison are presented with the model results. As a rule, all framed figures are from the experimental papers. Recent modelling activity related to these experiments is also presented, where the focus is on features seen in experiments that are not yet understood.

A research group in Israel started doing the experiments some years ago, with the first paper used in this thesis published in 2004 [45]. They later published several other papers with results from the same kind of experiment [5, 6, 46–48]. In 2010, a research group in Japan [37] published a variant of the experiments done by the group in Israel. These groups only represent part of the experimental research being done on friction [3, 4, 7, 8, 24, 25, 28, 50, 58], but it is the results from these experiments that will be used for comparison with the models. These experiments have lead to theoretical activity trying to understand the results [16, 37, 49], and a similar approach as used in these will be used here. These represent only one approach in the modelling of friction nowadays, see e.g. [12, 30] for other approaches.

First, the experimental setup is explained, and second, the measures available in the experiments are discussed. Many of the experimental details are not presented here, since they are not of immediate importance to the modelling. For a more complete description of the experiments, the reader is referred to the papers referenced above. Third, the modelling activity related to these experiments is discussed.

3.1 Experimental setup

In the experiments, friction between two blocks of poly(methyl methacrylate) (PMMA) separated by a rough interface is studied, see Figure 3.1a. The rough interface is illustrated in the inset of this figure. As discussed previously, the blocks are not in contact

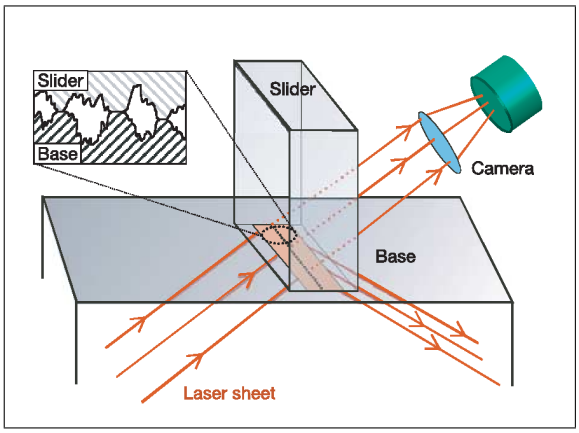

(a) A sketch of the experimental setup, depicting the two blocks of PMMA, the laser sheet and the camera. The inset is a schematic illustration of the interface between the two blocks. From [45], Figure 1.

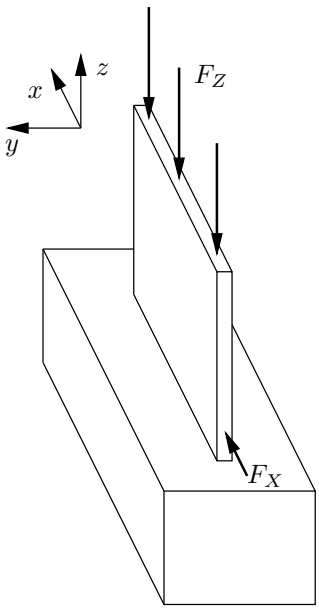

(b) A sketch of the system with the coordinate system and arrows indicating the direction of the tangential force F_X and the applied normal load F_Z.

Figure 3.1: Two illustrations of the experimental system depicting the laser sheet, camera and directions of loading. A typical system size is the one used in [6], with slider block dimensions $200 \times 6 \times 100$ mm and base block dimensions $300 \times 30 \times 28$ mm, meaning that the two illustrations above are not to scale.

throughout the whole interface, small pockets of air exist between the interlocking asperities.

PMMA is a brittle acrylic material and it is transparent. The blocks have a typical size of $200 \times 6 \times 100$ mm for the slider and $300 \times 30 \times 28$ mm for the base [6]. A laser sheet is directed towards the interface between the two blocks, incident at an angle greater than the critical angle for total internal reflection. If light from the laser hits two interlocking asperities, that is, it hits a PMMA-PMMA interface, light is transmitted through the slider and detected by a fast camera. However, if the laser light hits a PMMA-air interface, the light is totally reflected. As a consequence, the intensity of the laser light detected by the camera is a measure of the real area of contact.

A normal load F_Z is applied on the slider, as depicted in Figure 3.1b. In the experiments done by the group in Israel, the normal load is applied uniformly, though the magnitude is varied. In the experiment done by the group in Japan, the normal load is controlled through two loading points, one at the trailing edge and one at the leading edge. The normal force on these two points can be varied separately, causing the possibility for a non-uniform normal load.

Different ways of applying the tangential force F_X are used. One of them is depicted in Figure 3.1b, where the tangential force is applied on the slider, while the base is

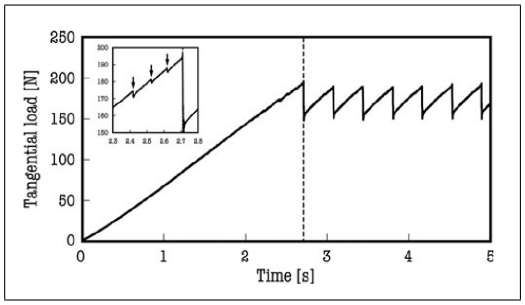

(a) Tangential force F_X as a function of time. An approximate linear increase with small bumps (precursor events) are followed by a regime with regular large drops in F_X (global events). From [37], Figure 4.

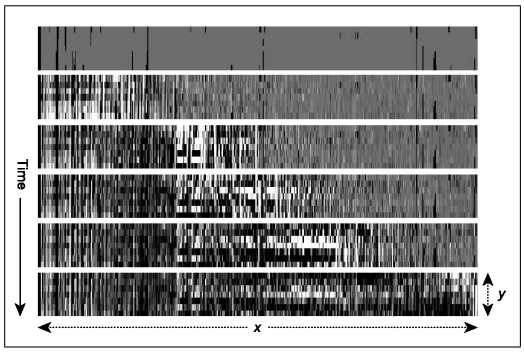

(b) Normalised area of contact at six different times for a single event. The top image shows the area of contact right before the event started. Darker (lighter) shades indicate a decreased (increased) contact area. From [45], Figure 3.

Figure 3.2: Two examples of data obtained in the discussed experiments. Even though these two figures are from two different experiments, the rightmost figure shows what happens to the area of contact in one of the large drops in the tangential force seen in the leftmost figure.

stationary. This driving mechanism is used in e.g. [5, 37, 45]. Another way of driving the system is to hold the slider stationary, and then apply the tangential load on the base block. This mechanism is used in e.g. [5, 6].

The tangential force F_X is usually applied through an elastic loader characterised by a spring constant K of order 10^6 N/m, where one end is connected to the base or slider. The other end is driven at a velocity V of order 10^{-4} m/s, causing an increased force F_X on the slider/base.

By attaching strain gauges at the side of the slider adjacent to the interface, data for the shear and normal stresses near the interface have been obtained [5]. Local slip along the interface at a chosen location has been obtained by using a displacement sensor based on a metallic grid placed at the side of the slider and measuring the diffraction pattern produced by a laser beam focused on this grid [6].

3.2 Experimental results

The experimental system is in the stick-slip regime, as can be seen in Figure 3.2a, where the time development of the applied tangential force F_X is shown. This curve can easily be compared with the schematic drawing in Figure 2.3. The drops in the tangential force appear to occur regularly, and the system shows periodic stick-slip behaviour.

Due to the high temporal resolution of the camera, the dynamics of each successive slip can be followed. Such slips are observed not to occur homogeneously along the interface, but rather through micro-slip front propagation. The propagation of one such front can be seen in Figure 3.2b, which depicts the time development of the local contact area. The passage of a micro-slip front is marked by a rapid change in this area, causing darker and lighter shades for decreased and increased areas, respectively. These fronts start

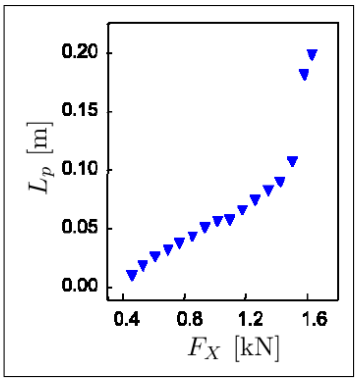

(a) The length of the precursors L_p plotted as a function of the tangential load F_X for $L_x = 0.2$ m and $F_Z = 3.3$ kN. From [47] Figure 2b.

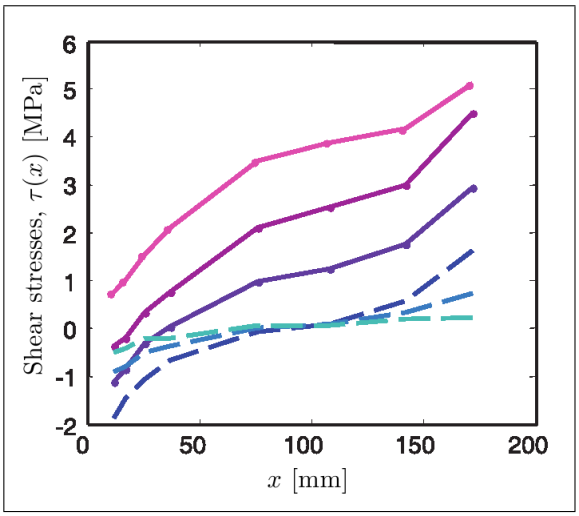

(b) Experimental shear stress profile. Dashed lines are for increasing normal load and no tangential load. The drawn lines are for constant normal load and increasing tangential load. From [5], Figure 1C.

Figure 3.3: The length of precursors are obtained through data from the camera such as that shown in Figure 3.2b, but information about the stresses are obtained through strain gauges placed adjacent to the interface, which is then converted to stress.

at the trailing edge and propagate to the leading edge. During these events, the whole block moves, causing the tangential load F_X to be reduced.

In the initial loading phase, F_X is seen to increase approximately linearly. However, small drops in the tangential load can be seen even before the periodic stick-slip begins. These small drops are called precursor events. They are also characterised by a rapid change in the local contact area starting at the trailing edge, but these micro-slip fronts do not reach the leading edge. During these events, the trailing edge of the block moves, decreasing the tangential load F_X, but the leading edge is still attached. Therefore, the whole block does not move during precursor events. It is only after a series of such precursors, each coming closer to the leading edge, that the first global event occurs: the micro-slip front finally reaches the leading edge, the whole block moves, and a large drop is seen in the tangential load.

Where the fronts are nucleated seems to depend on the driving mechanism. When the driving force is applied to the slider, events are seen to nucleate at the trailing edge only. However, when the driving force is applied to the base, and the slider is stationary, fronts are seen to nucleate not only at the trailing edge, but also at points between the trailing and the leading edge. If this happens, the front propagates both towards the trailing and the leading edge from the point of nucleation.

The length of the precursors can be plotted as a function of the applied tangential load right before the respective events are triggered. A typical result can be seen in Figure 3.3a. A series of precursors, each reaching further towards the leading edge, is seen for increasing tangential loads. There appears to be an abrupt change in this behaviour when the precursors have reached about halfway towards the leading edge. The fronts

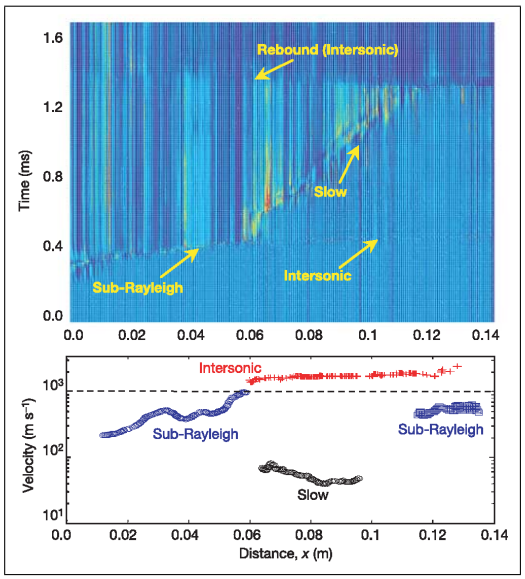

(a) Area of contact as a function of space and time (top). Hot and cold colours represent increased and decreased net contact area, respectively. Rupture velocities can be extracted from the slope of the change in contact area (bottom). From [45], Figure 4a.

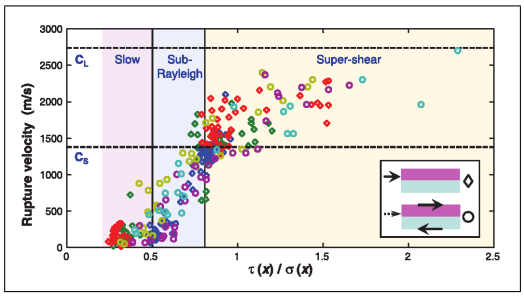

(b) The velocity of the rupture fronts as a function of the local shear to normal stress ratio. Different markers represent different drivings, and different colours indicate different positions along the interface. c_L and c_S are the longitudinal and shear wave velocities in PMMA, respectively. From [5], Figure 3.

Figure 3.4: By averaging over the y-dimension in Figure 3.2b, the local area of contact can be plotted as a function of both space and time, and rupture velocities can be extracted (left). Combining this with local stress data, the rupture velocity can be plotted as a function of different shear to normal stress ratios.

reach much further towards the leading edge for only a slightly larger tangential force.

As mentioned above, strain gauges are placed on the slider, enabling the measurement of the local strain, which is then converted to stress. The result of such measurements can be seen in Figure 3.3b, where the local shear stress is plotted as a function of position along the interface between the slider and the base.

To get a better picture of the dynamics of an event, the local area of contact is usually averaged over the y-dimension seen in Figure 3.2. The averaged local area of contact is then plotted as a function of both time and position along the interface, and a typical result can be seen in Figure 3.4a. The front propagating towards the leading edge is characterised by an abrupt change in the local area of contact, which in Figure 3.4a can be seen as an abrupt change in colour. The front is not propagating at a constant velocity, but is rather propagating at several different velocities that differ by almost two orders of magnitude. These velocities are compared to the velocity of sound in PMMA.

In solids, there are two types of bulk sound waves: longitudinal waves and shear waves. Longitudinal waves are the only type of sound waves in gases and liquids, and are characterised by compression and decompression in the direction of travel. These waves propagate with a velocity c_L, which in PMMA has been measured to be $c_L = 2730 \pm 50$ m/s [5, supplementary]. Shear waves are characterised by elastic deformations of the medium perpendicular to the direction of travel. These waves propagate with a speed c_S, which

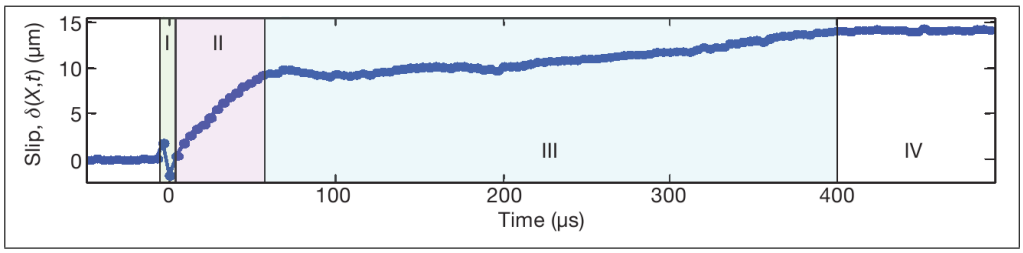

Figure 3.5: Local slip δ measured at a point X adjacent to the interface as a function of time for one precursor. From [6], Figure 2a.

in PMMA has been measured to be $c_S = 1370 \pm 50$ m/s.

These are the two types of sound waves that travel in the bulk. In addition, there are Rayleigh waves, which are waves propagating on the surface of the object, and are characterised by both a longitudinal and a vertical shear wave component. The velocity of Rayleigh waves, c_R, has been measured in PMMA to be $c_R = 1280 \pm 40$ m/s, which is quite close to the shear wave velocity.

By comparing the local rupture velocities to the local shear to normal stress ratio, an apparent dependence of one on the other is observed. Small stress ratios seem to favour small rupture velocities, and large stress ratios seem to favour large rupture velocities. This observation has been investigated quantitatively by plotting the local rupture velocity as a function of the local shear to normal stress ratio τ/σ for a given set of measurement points. The result can be seen in Figure 3.4b.

There appears to be a clear trend that higher stress ratios result in higher rupture velocities even though the spread in the data points is quite large: slow rupture velocities occur only for small shear to normal stress ratios and supershear only for quite high stress ratios. Another observation that can be made from Figure 3.4b is that the local stress ratio can greatly exceed the global static friction coefficient, which for PMMA is about 0.5.

The observed rupture velocities have been organised into three regimes: slow ruptures, characterised by velocities much less than the material wave speeds, sub-Rayleigh ruptures, with velocities less then the Rayleigh wave speed c_R, and the supershear ruptures, where the velocities exceed the shear wave speed c_S.

As mentioned above, the local slip δ as a function of time for precursor events has also been measured. The result can be seen in Figure 3.5, where the local slip measured at a point X along the interface is given as a function of time. The slip does not occur at a constant rate, but is rather divided into four phases. Phase I, called the detachment phase, is marked by an abrupt decrease in the local area of contact and oscillations in the local slip as a consequence of the rupture front passing by. Phase II is called the rapid slip phase, and is characterised by a rapid increase in the local slip. Then follows phase III in which slip occurs at a lower rate, about an order of magnitude less. In phase IV, the slip is constant, the sample is again locally attached to the base. The duration of phases II and III was observed to be surprisingly constant for different precursors. Phase II was observed to last about 60 μs and phase III for about 140 μs. This is illustrated by the rough data collapse seen in Figure 3.6

In [6], where the result in Figure 3.5 was presented, a qualitative explanation for the

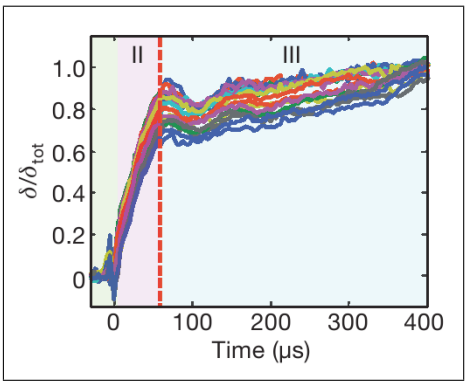

Figure 3.6: Normalised local slip δ measured at a point X adjacent to the interface as a function of time for 16 different precursors. From [6], Figure 2c.

temporal evolution of slip was proposed. It was proposed that the breaking of the micro contacts occurring in phase I leads to a significant release of heat that increases the local temperature above the glass temperature. This causes local shear strength weakening, and rapid slip then occurs (phase II). As the heat dissipates, the temperature decreases, causing an increased shear strength, which then leads to a smaller slip rate (phase III). It was shown that an estimate of the released heat per area results in cooling times compatible with the observed duration of phase II.

3.3 Modelling activity and open questions

It is now possible to speak more concretely about what is currently not understood in these experimental results. There are mainly three different modelling papers that have been trying to replicate the experimental results. New insights have been obtained through these, but there are still many unanswered questions to be addressed.

The Japanese group presented a model which they compared to their experimental results [37]. They used a one-dimensional spring-block model, where a chain of blocks is connected by springs and the friction between the blocks and the track is given by Amontons–Coulomb's laws of friction. By applying a force through a spring on the leftmost block, they observed a series of precursor events, which then lead to a global stick-slip behaviour. They then compared the loading curve and the length of the precursors as a function of tangential force to their experimental results for different normal loadings.

They saw a similar loading curve from the model as that in their experiments, but with some small deviations. The most striking difference was in the plot of the length of precursors, where there was a quite large deviation between the model and experimental results for all types of normal loading.

The transition from static friction to stick-slip motion was also studied in [49], where a minimalistic quasistatic one-dimensional model was presented and discussed. The model allows an analytical solution, and the kinematics of both the precursors and the stick-slip motion is dependent on the torque induced by the applied force F_X and the friction force F_f.

These two models are focused on understanding the effect of loading conditions and the subsequent stress distributions on the length of precursors. They show that non-

homogeneity, which may arise from e.g. loading conditions and/or friction induced torque, must be explicitly taken into account. However, a quantitative comparison between the results from these models and the experiments reveal serious discrepancies.

The wide range in the measured rupture velocities has surprised many, and is still not understood. Especially the very high velocities above the shear wave speed, and the very small velocities much smaller than the shear wave speed, have caused debate. In [16], a similar one-dimensional spring block model as that used by the Japanese group was presented. This model is based on the models in [15, 29], and presents a new time dependent friction law in place of the Amontons–Coulomb friction laws between the blocks and the track. The rupture dynamics was studied, and both slow and fast ruptures were observed, but no quantitative analysis of their results were performed.

Gaining further understanding of the length of precursors and the rupture velocities is the main objective of this thesis. The one-dimensional spring block model presented in [37] will be used as a starting point in order to do further investigations on both precursors and ruptures. The hope is that the models, since they are usually easier to understand than experimental results, can provide new insights into the transition from static friction to stick-slip motion.

Chapter 4

The one-dimensional spring-block model

The models studied in this thesis are usually called spring-block models, because they consist of of blocks connected by springs. This type of models has recently been applied to modelling the transition from static friction to stick-slip [16, 37], as mentioned in the previous chapter. They have also been applied by Persson [40, 41] in modelling sliding of an elastic block on a lubricated substrate, but they actually date back to the 1960s.

In their paper in 1967, Burridge and Knopoff [19] presented a spring-block model that they used to '... explore the role of friction along a fault as a factor in the earthquake mechanism.'. This model, today called the Burridge–Knopoff model, has since been used extensively in the modelling of earthquakes [23]. Statistical properties such as the rate and different size distributions of events are usual objects of study. It is a slight variation of this model that has recently been applied to friction. A master equation approach that allows the system to be solved analytically in some cases has recently been presented [12–14]. The usual approach is, however, to study these models through computer simulations, and it is that approach which is utilised here.

In this chapter, two different one-dimensional spring-block models are presented. They are actually the same model driven in two different ways, but I will refer to them as the side driven model and the top driven model. The side driven model is presented first, going from the model, through the equations of motion to the results, which are then compared with results from experiments. The top driven model, which is actually the Burridge–Knopoff model, will then be presented, where the focus will be on results that are different from the side driven model.

Considering the experimental setup, shown in Figure 3.1, it might seem strange to consider the system one-dimensional. The slider is long and thin, but it is also very high. Since the slider is thin, it is natural to ignore the y-dimension dimension at least in the first steps of an analysis. However, ignoring the vertical dimension, as will be done in the one-dimensional models, seems strange. On the other hand, the importance of this dimension is not yet understood. A reasonable way of attacking this problem is then starting out with the simplest model, the one-dimensional, and investigating how it compares to the experiments. If necessary, the vertical dimension should then be included in the next step of the analysis.

4.1 The one-dimensional model with side driving

The slider is modelled as N blocks with masses m serially connected by massless linear springs with spring constant k, as shown in Figure 4.1. The mass of each block is $m = M/N$, where M is the total slider mass. The system depicted in this figure is driven from the side, meaning that a point P is connected to the leftmost mass by a massless linear spring with spring constant K. This point moves at a constant velocity V, thereby moving the sample. Open boundary conditions are used.

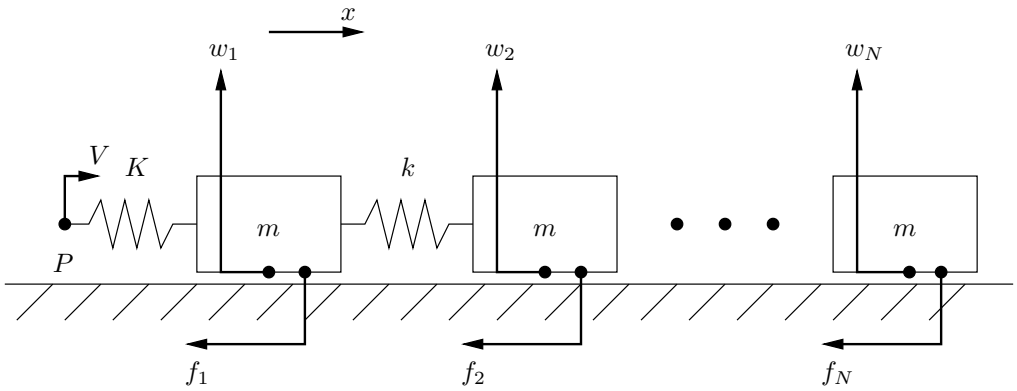

Figure 4.1: Sketch of the one-dimensional side driven model. The system is driven by the the point P moving with a constant velocity V connected to the first block through a spring with spring constant K.

The system is loaded by a total vertical force F_Z, which is distributed among the blocks. Each block will be subject to a normal force w_n as illustrated in Figure 4.1. An imposed friction force f_n acts on all blocks, and the right edge is free.

By using Newton's laws, the equations of motion for this system are given by

$$\begin{array}{ll} m\ddot{u}_1 = k(u_2 - u_1) + f_1 + F_1^K & \text{for } n = 1, \\ m\ddot{u}_n = k(u_{n-1} - 2u_n + u_{n+1}) + f_n + F_n^K & \text{for } 2 \leq n \leq N, \\ m\ddot{u}_N = k(u_{N-1} - u_N) + f_N + F_n^K & \text{for } n = N, \end{array} \tag{4.1}$$

where $\dot{}$ denotes the time derivative, $u_n = u_n(t)$ is the position of block n with respect to its initial position, F_n^K is the driving force on block n, and f_n is the local friction force from the track on block n. The introduction of F_n^K may seem unnecessary since only the first block will have a non-zero driving force, but this will be useful later on. For the side driven model, this driving force is given by

$$\boxed{F_n^K = \begin{cases} F_1^K = K(Vt - u_1), & n = 1 \\ F_n^K = 0, & n = 2, \ldots, N. \end{cases}} \tag{4.2}$$

The total driving force, also called the tangential load, is then given by

$$F_X(t) = \sum_{n=1}^{N} F_n^K. \tag{4.3}$$

A simple modification to equation (4.1) is needed in order to get physically reasonable results [33]. It has been shown that equation (4.1) induce large oscillations in e.g. the

shear force with wavelength $2a$, where a is the lattice spacing. This is very unfortunate, because physical quantities such as the shear stress will then oscillate in a way that is highly dependent on the number of blocks. To reduce these oscillations, a relative viscous damping force is introduced in the equations of motion. This damping force damps out relative movement between the blocks, and takes the form

$$F_n^\eta = \begin{cases} \eta(\dot{u}_2 - \dot{u}_1) & n = 1 \\ \eta(\dot{u}_{n+1} - 2\dot{u}_n + \dot{u}_{n-1}) & n = 2, \ldots, N-1 \\ \eta(\dot{u}_{N-1} - \dot{u}_N) & n = N. \end{cases} \tag{4.4}$$

The equations of motion are then modified to include this damping force:

$$\boxed{\begin{array}{ll} m\ddot{u}_1 = k(u_2 - u_1) + F_1^K + f_1 + F_1^\eta & \text{for } n = 1, \\ m\ddot{u}_n = k(u_{n-1} - 2u_n + u_{n+1}) + F_n^K + f_n + F_n^\eta & \text{for } 2 \leq n \leq N-1, \\ m\ddot{u}_N = k(u_{N-1} - u_N) + F_N^K + f_N + F_N^\eta & \text{for } n = N. \end{array}} \tag{4.5}$$

The shear force, that is, the sum of all forces except friction on a block, is then given by

$$\boxed{F_n^{\text{n.f.}} = \begin{cases} k(u_2 - u_1) + F_1^K + F_1^\eta & n = 1 \\ k(u_{n+1} - 2u_n + u_{n-1}) + F_n^K + F_n^\eta & 2 \leq n \leq N-1 \\ k(u_{N-1} - u_N) + F_N^K + F_N^\eta & n = N. \end{cases}} \tag{4.6}$$

The abbreviation n.f. stands for "no friction", indicating that $F_n^{\text{n.f.}}$ is the sum of all forces acting on block n excepting the friction force.

The value of η should be chosen so that the impact on the dynamics is as small as possible, but at the same time effectively reduce the unwanted oscillations. In the simulations, the value $\eta = \sqrt{0.1}\sqrt{km}$ is used, and an explanation of how this value is chosen is given in Appendix A.1. The value of the parameters used is given in Table 4.1. If other parameter values are used, this is explicitly stated. Some numerical notes on how to solve (4.5) are given in Appendix A.2. How a block is stopped and started and a way to speed up the calculations are given too.

Details on how the time step is chosen are also given in Appendix A.2. In the results given here, a time step $\Delta t = 1 \times 10^{-7}$ s has been used for $N = 100$, which is less than the period of oscillation for $N = 100$, given by equation (A.15), which is 7×10^{-7} s. The time step used for other N is calculated using the scaling given in equation (A.15).

4.2 Spring constants, normal loading and local friction

The values of the spring constant k and the normal loads w_n now have to be chosen, and this has to be done in a physically reasonable way. In addition, a local friction law between the blocks and the track has to be imposed. This is the focus of this section.

4.2.1 Choosing the material spring constant: Young's modulus

The values of the spring constants k should be chosen in accordance with equation (2.7), meaning that the blocks will behave as PMMA when subjected to tension or compression.

Physical quantity	Symbol	Value in simulation
Total slider mass	M	0.012 kg
Young's modulus	E	2.5 GPa
Sample size in x-direction	L_x	100 mm
Sample size in y-direction	L_y	5 mm
Sample size in z-direction	L_z	20 mm
Static friction coefficient	μ_s	0.70
Dynamic friction coefficient	μ_d	0.45
Relative viscous damping	η	$\sqrt{0.1}\sqrt{km}$
Applied normal load	F_Z	400 N
Driving point velocity	V	0.1 mm/s
Driving spring constant, side driven model	K	0.8 MN/m
Driving spring constant, top driven model	K_n	K/N

Table 4.1: Overview of the physical constants and parameters used in the simulation. These are chosen to be the same as in [37] in order to make simulation results comparable to the experiment.

It is then necessary to obtain a relationship between the spring constant k and Young's modulus E. According to equation (2.7)

$$E = \frac{F_\perp}{A}\frac{L_x}{\Delta L_x}, \tag{4.7}$$

where $F_\perp$ is the applied force, $A = L_y L_z$ is the area of the cross section the force $F_\perp$ is applied to, L_x is the length and ΔL_x is the length difference. For massless springs connected in series, the total spring constant is given by [59]

$$\frac{1}{k_{\text{tot}}} = \sum_{n=1}^{N-1}\frac{1}{k} = \frac{N-1}{k}, \tag{4.8}$$

meaning that the whole system will behave as one spring with the spring constant k_{tot}, $F_\perp = k_{\text{tot}}\Delta L$. Combining these two results leads to the relation

$$E = \frac{k_{\text{tot}} L_x}{A}, \tag{4.9}$$

which inserted for k_{tot} can be solved for k:

$$\boxed{k = (N-1)EL_yL_z/L_x.} \tag{4.10}$$

This equation then provides a relation between Young's modulus E and the material spring constant k.

4.2.2 Non-uniform normal loading

As mentioned in chapter 3, the group in Japan varied the normal load systematically. This non-uniform normal load is modelled as a linear trend in the normal load on each block, w_n, given by

$$\boxed{w_n = \frac{F_Z}{N}\left(1 + \frac{2n-N-1}{N-1}\theta\right).} \tag{4.11}$$

The parameter $\theta \in [-1, 1]$ is then a measure of the non-uniformity, where $\theta = 0$ corresponds to equal weights for all blocks and $\theta > 0$ leads to a decreased normal load on the trailing edge and an increased normal load on the leading edge.

The non-uniform normal load is then modelled as in [37]. In the experiments, the applied normal load might be approximately linear at the top of the sample because of the loading mechanism, but there is no guarantee of linearity in the normal stress on the side in contact with the base. This is a two-dimensional effect, and will be discussed further at a later point in this chapter.

4.2.3 The local friction law

The other part of the model is the friction law that has to be imposed between the blocks and the base (sometimes called track). In this chapter, the Amontons–Coulomb laws of friction are used, meaning that two local friction coefficients must be introduced, μ_d and μ_s. The friction force on block n is then given by

$$\boxed{f_n = \begin{cases} f_n^s & \text{when } \dot{u} = 0 \\ -f_n^d & \text{when } \dot{u} > 0 \\ f_n^d & \text{when } \dot{u} < 0. \end{cases}} \tag{4.12}$$

f_n^s and f_n^d are the (local) static and dynamic friction on block n, respectively. The local static friction takes values in the range

$$-\mu_s w_n = -f_n^{s,\max} \leq f_n^s \leq f_n^{s,\max} = \mu_s w_n, \tag{4.13}$$

in order to keep the block from moving. If the total force (except friction) on a block exceeds the maximum static friction force $f_n^{s,\max}$, the block starts moving under the influence of dynamic friction, which is given by

$$f_n^d = \mu_d w_n. \tag{4.14}$$

This is, of course, only an example of a friction law that can be applied to the system. It is not expected that a simple law such as the Amontons–Coulomb law will reproduce all the features seen in experiments. A quite different friction law was used in [16], and two different friction laws will be introduced in chapter 6.

One of the interesting parts will be to see if one can predict from a given local friction law, the global friction law of the system. It will be shown that this can indeed be done to some extent given a locally applied Amontons–Coulomb friction law.

4.3 The initial condition

The equations of motion (4.5) are N coupled second order ordinary differential equations. This means that in order to obtain a unique solution, $2N$ initial conditions must be given, e.g. the velocities and positions of all blocks at the time initial t_0 where the simulation is to start (not necessarily at $t = 0$ with zero driving force). Throughout this work, the initial velocity of all blocks will be set to zero. The initial position of the blocks

determines the initial shear force on each block, and it may be of interest to provide the initial shear force on all blocks initially. The reason for this is that the Poisson effect in a two- and three-dimensional system causes a non-zero initial shear force (this is explained in section 4.10). A way of calculating the position of all blocks from the shear force is then needed. An iterative scheme for doing so for the side driven model is presented in this section.

The shear force on the blocks is given by equation (4.6). The initial position of block 1 is assumed to be $u_1(t_0) = 0$. The sum of all external forces is also assumed to be zero, meaning that the driving force must equal the sum of all friction forces. Since all blocks are at rest, the friction force on each block equals the shear force on that block. The initial driving force $F_X(t_0)$ is then given by

$$F_X(t_0) = \sum_{n=1}^{N} F_n^{\text{n.f.}}(t_0) = KVt_0. \tag{4.15}$$

From this equation, the initial time t_0 can be calculated. It may seem strange to calculate the initial time from the initial condition, but it is just a consequence of the explicitly chosen form of the driving force F_X. t_0 is the time needed to build up a large enough force in the driving spring to compensate for the friction forces when the driving spring is relaxed at $t = 0$.

Equation (4.6) can now be used to calculate the initial positions of the blocks. This equation can be solved with respect to the position of the block with the highest index, leading to the relation

$$\boxed{u_n = \begin{cases} 0 & n = 1 \\ u_1 + (F_1^{\text{n.f.}} - F_X)/k & n = 2 \\ 2u_{n-1} - u_{n-2} + F_{n-1}^{\text{n.f.}}/k & n = 3, 4, \ldots, N. \end{cases}} \tag{4.16}$$

This formula can then be used to calculate the position of all blocks, starting with block 2, and iterating to block N, using the positions calculated for the blocks with a lower index. It may seem strange that the shear force on block N, $F_N^{\text{n.f.}}$, is not used in this formula. However, it is taken into account because it is included in the driving force F_X, making sure that the shear force profile generated from equation (4.16) is the correct one.

A point worth mentioning is that if zero driving force is desired, then the shear forces must sum up to zero. This is just a consequence of the fact that without an external driving force, the sum of all the friction forces must be zero in order to ensure that the external forces sum to zero.

In most simulations the initial shear force on each block is zero. If the method described here is used in order to obtain non-zero initial shear forces, it is explicitly stated, and the initial shear force profile used is then also given.

4.4 Analytical analysis of the one-block model

It is always useful to study a system analytically as well as numerically. Through an analytical calculation one usually gains both increased understanding of the system and a way to verify that the numerical solution is in fact correct.

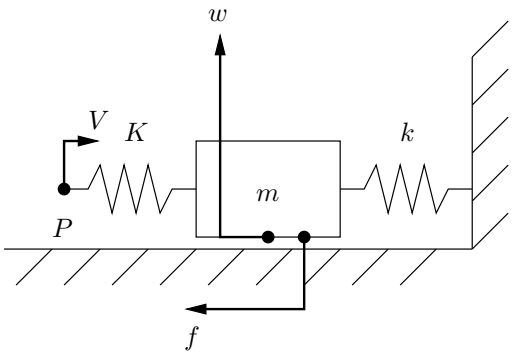

Figure 4.2: Sketch of the system depicted in Figure 4.1 with only 1 block. This block is attached to a rigid wall by a spring with spring constant k which can be removed by setting $k = 0$.

The N block system is rather difficult, maybe impossible, to solve analytically, and a simplified version that consists only of one block is depicted in Figure 4.2. The block is driven from the left through a spring with spring constant K and attached to a rigid wall on the right through a spring with spring constant k. Setting $k = 0$ will result in the one-block version of the side driven model depicted in Figure 4.1. This spring is, however, included for later convenience. Viscous damping is ignored.

The two springs are assumed to be relaxed at $t = 0$. The equation of motion is then given by

$$\ddot{u}(t) + \omega^2 u(t) = \frac{KV}{m}t - \frac{\mu_d w}{m}, \qquad \omega = \sqrt{\frac{K+k}{m}}, \tag{4.17}$$

where $u(t)$ is the position of the block relative to its initial position as a function of time. The equation of motion is valid from $t = t_0$, where t_0 is the time the block starts to move, to $t = t_1$, when the block stops (if such a time exists). The time t_0 is given by the fact that the driving spring force is equal to the maximum static friction force:

$$KVt_0 = \mu_s w \quad \Rightarrow \quad t_0 = \frac{\mu_s w}{KV}. \tag{4.18}$$

Equation (4.17) has a homogeneous solution on the form

$$u_h(t) = C\sin(\omega t - \phi), \tag{4.19}$$

where C and ϕ are constants given by the initial conditions, and a particular solution given by

$$u_p(t) = \frac{KVt - \mu_d w}{K+k}, \tag{4.20}$$

which means that the solution of equation (4.17) is given by

$$u(t) = u_h(t) + u_p(t) = C\sin(\omega t - \phi) + \frac{KVt - \mu_d w}{K+k}. \tag{4.21}$$

Since $x = 0$ is the equilibrium position, and the block is not moving at $t = t_0$, the initial conditions are

$$u(t_0) = 0, \qquad \dot{u}(t_0) = 0. \tag{4.22}$$

The velocity of the block,

$$\dot{u}(t) = C\omega\cos(\omega t - \phi) + \frac{KV}{K+k},$$

will become zero at the time $t_1 = t_0 + 2\pi/\omega$ at the latest because of the periodicity of the cosine function and the fact that $\dot{u}(t = t_0) = 0$ from the initial condition. The block has then stopped, and needs to be loaded up to the static friction level again. As a consequence, this system, including the special case $k = 0$, will only result in periodic stick-slip motion, meaning that chaotic stick-slip and steady sliding will not occur for any set of parameters.

The constants C and ϕ will now be found for the initial conditions given in equation (4.22). Applying the solution in equation (4.21) to these initial conditions and using equation (4.18) for t_0 results in the two equations

$$C \sin(\omega t_0 - \phi) = -\frac{(\mu_s - \mu_d)w}{k + K}, \tag{4.23}$$

$$C\omega \cos(\omega t_0 - \phi) = -\frac{KV}{k + K}. \tag{4.24}$$

Multiplying the upper equation by ω, then squaring both and summing them and using the identity $\sin^2\theta + \cos^2\theta = 1$ results in

$$C = \pm\sqrt{\left[\frac{(\mu_s - \mu_d)w}{k + K}\right]^2 + \left[\frac{KV}{(k + K)\omega}\right]^2}.$$

The phase ϕ can now be found from either of equations (4.23) and (4.24), resulting in

$$\phi = \arcsin\left[\frac{(\mu_s - \mu_d)w}{(k + K)C}\right] + \omega t_0.$$

In order to determine the sign of C, the obtained expressions for C and ϕ should be inserted back into equations (4.23) and (4.24). As it turns out, both signs of C are applicable, because ϕ is changing accordingly (the two solutions are equivalent). The solution of the equation of motion for one block is then given by

$$\boxed{\begin{aligned} u(t) &= C\sin(\omega t - \phi) + \frac{KVt - \mu_d w}{K + k}, \\ C &= \sqrt{\left[\frac{(\mu_s - \mu_d)w}{k + K}\right]^2 + \left[\frac{KV}{(k + K)\omega}\right]^2}, \qquad \phi = \arcsin\left[\frac{(\mu_s - \mu_d)w}{(k + K)C}\right] + \omega t_0. \end{aligned}} \tag{4.25}$$

4.5 First model results

In this section, the first results obtained from simulations of the side driven model will be presented. First, the code is verified using the analytical solution obtained in section 4.4. Second, the need for the relative viscous damping is investigated by looking at the shear force profile with and without this damping. Third, the loading curve from the model is compared to the experimental loading curve, and fourth, the shear force profile is investigated.

4.5.1 Verification of the code

Verifying that the code is actually working is important. The code should then be run for a system that is solvable analytically, and the result should be compared to the

analytical solution. The most important parts of this code are the starting and stopping of blocks, the skipping of stick periods (discussed in Appendix A.2), and the integration algorithm itself.

From $t = 0$, the force on the first block will increase because of the increased driving force. When the force has reached the maximum static friction level, the first block begins to move. If it moves far enough, increasing the force on the second block to above the static friction level, this will also begin to move. This situation is similar to that discussed in section 4.4, but there the second block was a rigid wall which will never begin to move. However, from the solution given in equation (4.25), it is possible to calculate if the force has exceeded the static friction level. This can be done by calculating the shear force on the wall at $t = t_1 = t_0 + \pi/\omega$, which is the time when the block stops. The position of the block at this time is given by equation (4.25), and inserting $t = t_1$ results in:

$$\begin{aligned} u(t_1) &= C\sin(\omega t_1 - \phi) + \frac{KVt_1 - \mu_d w}{K + k} \\ &= C\sin(\omega t_0 - \phi + \pi) + \frac{KV(t_0 + \pi/\omega) - \mu_d w}{K + k} \\ &= -C\sin(\omega t_0 - \phi) + \frac{KVt_0 - \mu_d w}{K + k} + \frac{\pi/\omega}{K + k} \\ &= \frac{2(\mu_s - \mu_d)w}{k + K} + \frac{\pi/\omega}{K + k}, \end{aligned}$$

where equations (4.18) and (4.23) have been used. The shear force on the wall is then given by

$$ku(t) = \left[2(\mu_s - \mu_d)w + \pi/\omega\right] \frac{k}{k + K}. \tag{4.26}$$

Using $N = 10$, $\theta = g = 0$ and the parameters given in Table 4.1, the shear force on the wall is approximately 19 N, which is less than the static level $\mu_s w = 28$ N. This means that in a simulation with similar parameters and $\eta = 0$, the second block will not begin to move. $u_1(t)$ obtained from the numerical simulation with $\eta = 0$ should then equal $u(t)$ given in equation (4.25) when $t \in [t_0, t_1]$, and the first event will therefore involve only the first block. This can be used to verify the code, because it will include both the starting and stopping of blocks in addition to the skipping of stick periods.

The numerical and analytical solutions are plotted in Figure 4.3. By comparing the two solutions more closely, one finds that both the starting and stopping of the blocks, and the skipping of stick periods is working. The absolute error in the numerical solution is shown in the lowermost plot in Figure 4.3, and by comparing this to the position shown in the uppermost plot, one sees that the error is orders of magnitude less than the value of the position itself. The relative error is not plotted because $u(t_0)$ is zero. In addition, the error does not keep increasing, but is actually decreasing in the second half of the time span shown. This indicates that the Runge–Kutta algorithm of the fourth order is an appropriate integration algorithm for this system.

4.5.2 Oscillations and viscous damping

The equations of motion for the system without the relative viscous damping were said to induce oscillations of wavelength $2a$, where $a = L_x/(N - 1)$ is the equilibrium distance

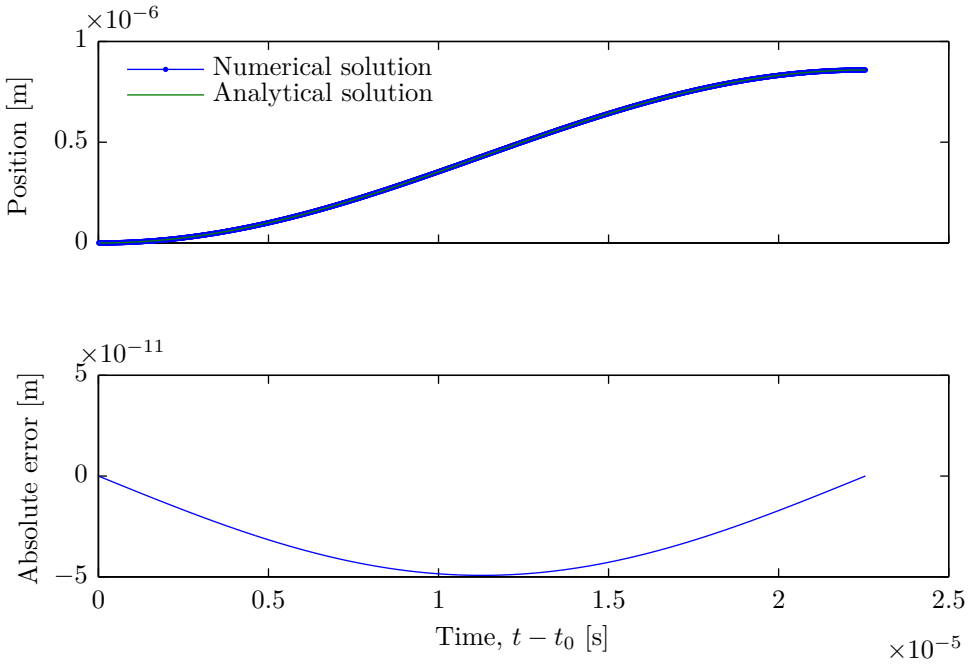

Figure 4.3: The uppermost plot shows the position of block 1 as a function of time for the first event in the side driven model, where both the numerical and analytical solutions are shown. The lowermost plot shows the absolute error in the numerical solution as a function of time. $N = 10$, $\theta = g = 0$ and $\eta = 0$. Other parameters are as in Table 4.1.

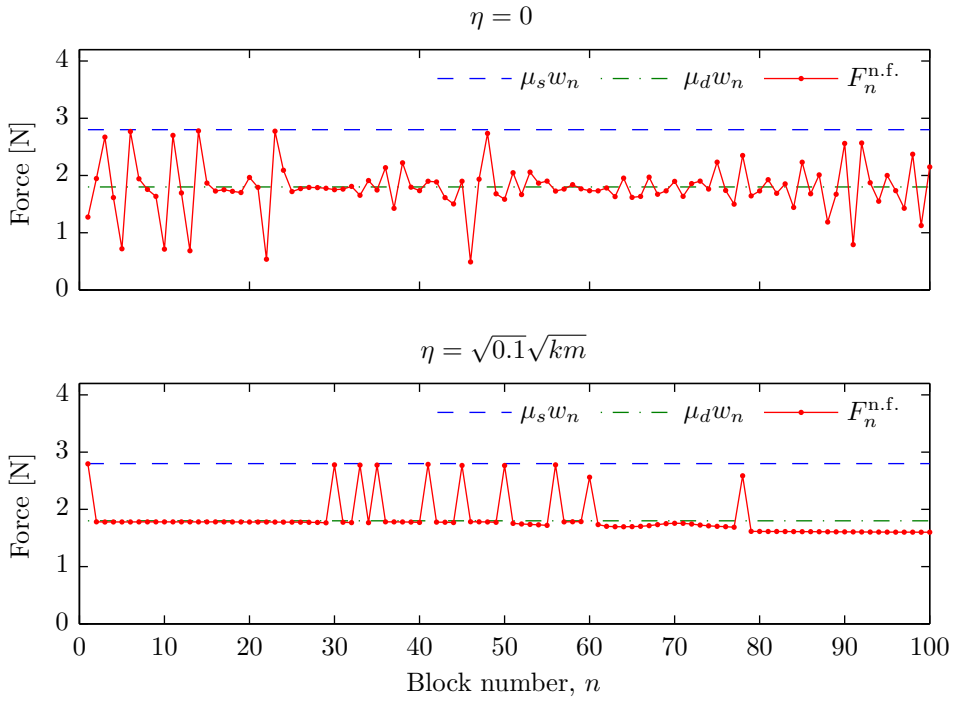

Figure 4.4: This figure illustrates the shear force profile at $t = 4$ s for a simulation done with $N = 100$, $\theta = 0$ and $g = 0$ for the side driven model. The topmost plot is without viscous damping, and the lowermost plot has $\eta = \sqrt{0.1}\sqrt{km}$.

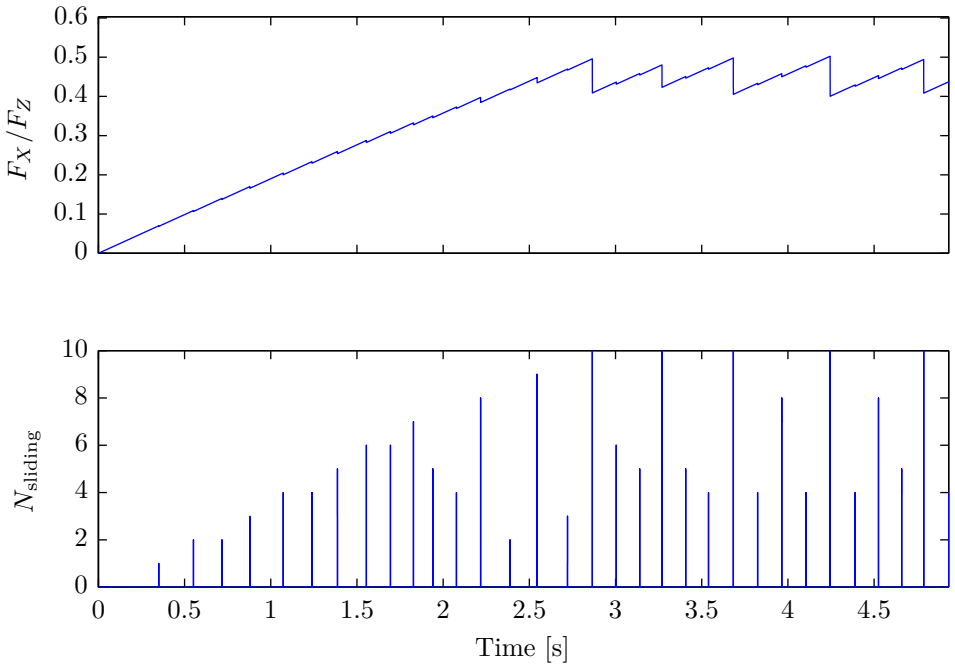

Figure 4.5: The uppermost shows tangential force as a function of time normalised by the total normal load for $N = 10$, $\theta = 0$ and $g = 0$. The lowermost plot shows the number of sliding blocks as a function of time.

between the blocks. As an illustration of these oscillations, consider Figure 4.4. In these two plots, the shear force in the sample is plotted without viscous damping in the uppermost plot and with viscous damping in the lowermost plot.

In the uppermost plot, there are oscillations in the shear force on the scale of the lattice spacing. This is not physical, because then the shear force profile will depend highly on the resolution, the number of blocks used. These effects are significantly reduced with the introduction of the viscous damping force, as can be seen in the lowermost plot.

As long as η is not chosen to be close to the critical damping value of $\sqrt{km}$, the results given here does not depend to a great extent on the chosen value of η. This will, however, be discussed in greater detail in section 4.17.

4.5.3 Stick-slip behaviour

The first results obtained from the model will now be presented. The result from a simulation with $N = 10$, $\theta = 0$ and $g = 0$ can be seen in Figure 4.5. The parameter g will be properly introduced later, but $g = 0$ corresponds to the system discussed up until now. The model exhibits stick-slip behaviour where the number of sliding blocks increases until global slip is achieved. The topmost graph shows resemblance with Figure 3.2a, which shows the corresponding experimental result for the used parameter set. The first global event appears to happen at roughly the same time, and the tangential load stabilises at roughly the same level. The model system, however, shows chaotic stick-slip behaviour, while the experimental system showed periodic stick-slip.

A clarification of the term "global event" is now needed. In the experiments, a global event is an event where the rupture front reaches the leading edge. In the model, this is translated to mean that it is the distance from the trailing edge to the position of the block closest to the leading edge that moved during the event. However, this is in fact not the same as the length of the spikes seen in the lowermost plot of Figure 4.5, which shows the instantaneous number of blocks sliding, N_{sliding}, as a function of time. The height of one of these spikes is the largest number of blocks sliding at the same time in an event.

In theory, an event could consist of a front propagating towards the leading edge, where some of the blocks behind the front stop moving. The number of blocks sliding will then not reflect how far towards the leading edge the front reached before it stopped. This is, however, a minor effect rarely seen in the model results. For example, all global events in Figure 4.5 involve all blocks moving at the same time. However, the length of a precursor in the model is defined as the distance between the trailing edge and the block closest to the leading that moved as a part of the event.

The result shown in Figure 4.5 is compatible to the simulation result given in Figure 10 of [37]. The match is not perfect for several reasons. Firstly, the result presented in [37] has no relative viscous damping included, leading to a slightly different time development of the system. Secondly, the exact placement of the events is sensitive to numerical details. How blocks are started and stopped is going to affect the exact location in time of the events, therefore leading to slightly different results. This however, does not affect the overall dynamics of the system, meaning that it does not affect the qualitative behaviour seen in Figure 4.5 with precursors and global events.

Variation of the static friction coefficient μ_s, keeping μ_d constant, shows that the value of μ_s determines the height of the drops in the tangential force during an event. For higher values of μ_s, the resulting drops are larger. The reason is that with a higher difference between the friction coefficients, the force drop when a block starts to move is higher. The acceleration of a block will therefore be increased with increasing μ_s, resulting in a larger displacement in an event, and consequently a larger drop in the driving force.

Variation of the dynamic friction coefficient μ_d keeping μ_s constant shows that the mean of the F_X/F_Z curve will always be approximately equal to μ_d. The reason for this will become clear when considering the shear force profile, which is done in the next section.

The most obvious difference between the model result shown in Figure 4.5 and the experimental result shown in Figure 3.2a is possibly the small events between the global ones. The reason for this deviation is at this point unclear, however, a possible reason will be discussed in section 4.18.

The vertical lines in the lowermost plot in Figure 4.5 hides complicated dynamics, as can be seen in Figure 4.6, which is a zoomed in version of Figure 4.5. The number of sliding blocks increases to the maximum level in a non-trivial way.

This is also illustrated in Figure 4.7, where the velocities of all the blocks are plotted as a function of time and space. A front is propagating from the trailing edge to the leading edge, and blocks accelerate and decelerate several times during an event as a consequence of sound waves propagating between the trailing and leading edge.

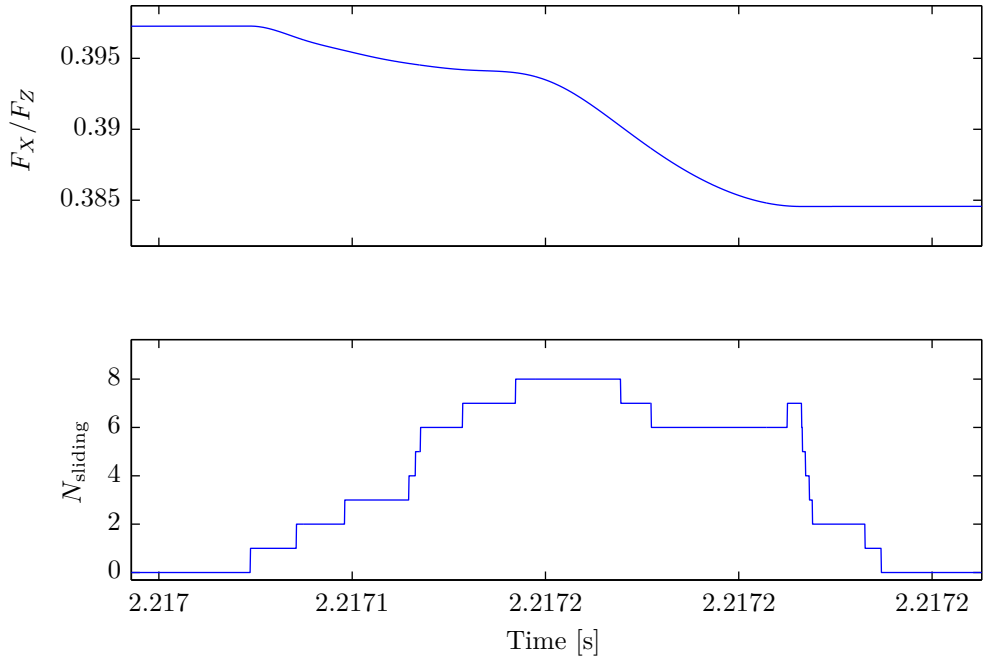

Figure 4.6: This is the same plot as shown in Figure 4.5, but zoomed in on the second global slip event. This shows that a slip event as shown in Figure 4.5 hides complicated dynamics.

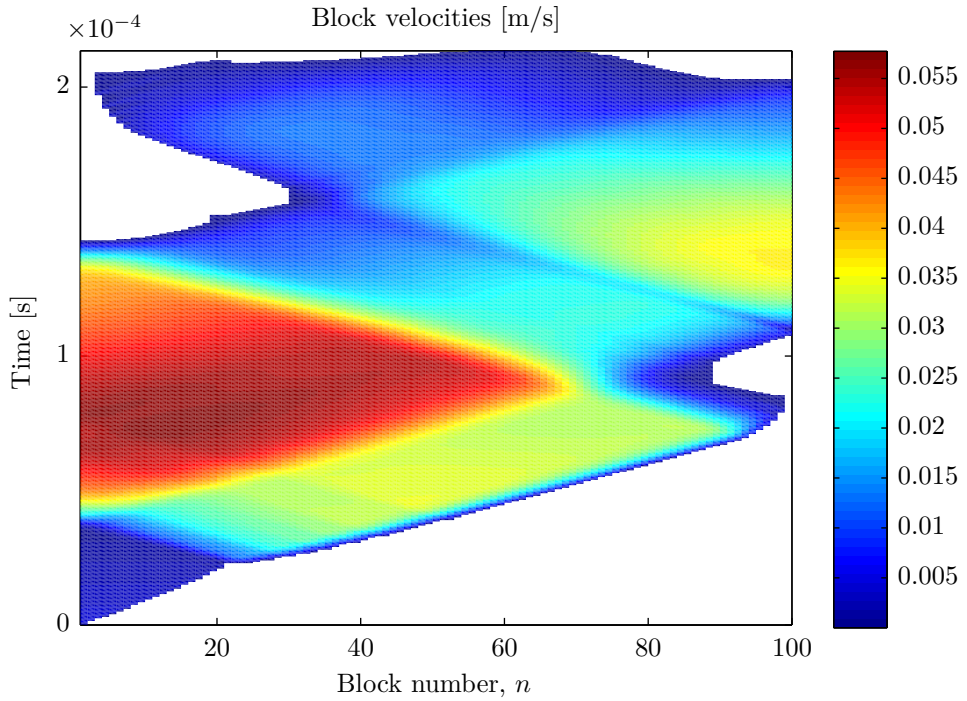

Figure 4.7: The velocity of the blocks plotted as a function of both space and time for the first global event. A front is seen to nucleate at the trailing edge and propagate towards the leading edge. Waves are then reflected back and forth between the trailing and leading edge before the event ends, and the blocks stop moving. Simulation is done with $N = 100$, $\theta = g = 0$, and other parameters as in Table 4.1.

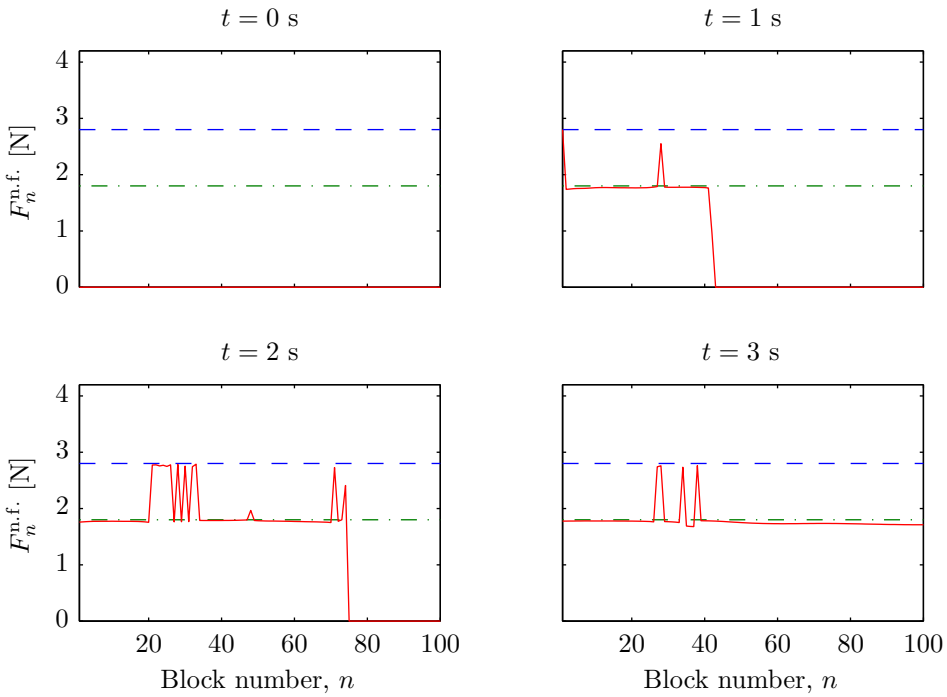

Figure 4.8: Plots of the shear force profile in the sample at different times for $N = 100$ and $\theta = g = 0$ for the side driven model. The long dashed line (blue) is the level of local static friction, the dashed-dotted line (green) is the level of local dynamic friction, and the drawn line (red) is the shear force profile. The time development of the driving force can be seen in Figure 4.17.

It is worth noting that in this model, all events must nucleate at the trailing edge because while all blocks are stationary, only block 1 is affected by the driving. This model is most similar to the experiments where the driving force is applied at the slider, which means that all events should nucleate at the trailing edge. This is then also a feature seen in experiments that is reproduced by the model, but in a rather imposed way.

In the next section, the shear force profile is investigated, and it will be shown in section 4.6 that this can be used in order to predict the length of a precursor in the model.

4.5.4 Shear force profile

Plots of the shear force at different times for the side driven model can be seen in Figure 4.8 for $N = 100$ and $\theta = g = 0$. Since only the trailing edge block is affected by the driving, the shear force (drawn line) on this block will in the beginning increase. When the level of maximum static friction is reached (dashed line), then the block starts sliding and this in turn increases the shear force on the block next to it.

As can be seen from Figure 4.8, the shear force on the blocks that have moved is approximately equal to the local dynamic friction (dashed-dotted line). The shear force on the blocks that have not moved is equal to the initial shear force, in this case zero. The exception is the block closest to the trailing edge that has not moved, since this

block will feel an increased force from its left neighbour. This might in turn result in a peak in the shear force profile.

The mean level of the F_X/F_Z curve observed in the previous section can now be understood. In the global event regime, the shear force on all blocks is approximately equal to the local dynamic friction level. When the blocks are stationary, the static friction force must be of equal magnitude, leading to a sum of friction forces approximately equal to $\mu_d F_Z$. When the whole system is stationary, the sum of the external forces must sum to zero, which means that the driving force must also be approximately equal to $\mu_d F_Z$ with a direction opposite to that of the friction forces.

The shear force in Figure 4.8 does not resemble the shear stress profile obtained in experiments, given in Figure 3.3b. This is to be expected, since the highly non-linear shear stress profile observed in experiments is a two-dimensional effect. When the normal load is exerted on the slider, Poisson expansion leads to a slight elongation in the x-direction along the interface. However, the interface is stuck because of friction, leading to an anti-symmetric shear force profile like the one given in Figure 3.3b. This is the first indication of the importance of the vertical dimension.

4.6 Precursor lengths

One of the experimental results presented in chapter 3 is the length of the precursors L_p as a function of the tangential load F_X right before the event. In the model the length of the precursor is the distance between the trailing edge and the position of the block closest to the leading edge that moved during the event. The corresponding tangential load F_X right before the event can be extracted from the model result easily.

As mentioned in chapter 3, the distribution of the normal load was varied in [37]. This can also be done in the model, and the result will be compared to the experimental data available. It will be shown that the shear force profile observed in the previous section can be used to predict how long a precursor will be for a given tangential load.

4.6.1 Comparison between the model and experimental results

The model result for different degrees of non-uniform normal loading is shown in Figure 4.9a. As seen in experiments, an increased tangential force leads to a longer precursor. The precursors keep increasing in length until they reach the leading edge, and this appears to happen at $F_X/F_Z \approx 0.45$, which incidentally is the dynamic friction coefficient. The reason for this is that right before the first global event, all blocks except the ones very close to the trailing edge, have a shear force equal to the local dynamic friction level, leading to $F_X/F_Z \approx 0.45$ by the same reasoning as used above.

Figure 4.9a also shows that the normal loading has a quite large effect on the length of precursors. $\theta < 0$ means an increased normal load on the trailing edge. The static and dynamic friction levels are then increased compared to the uniform loading, and a greater tangential force is needed in order to initiate a precursor of the same length. However, the first global event happens for approximately the same tangential force.

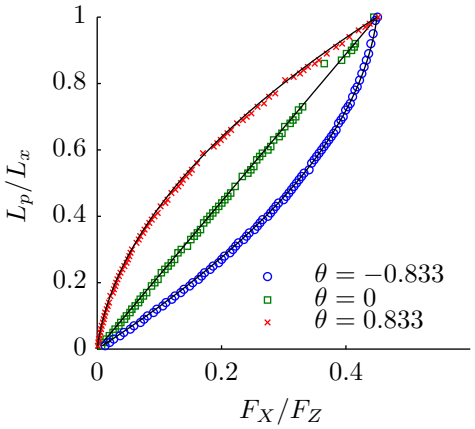

(a) Simulation result with $N = 100$ and $g = 0$ for different degrees of non-uniform normal loading θ. Black drawn lines are the curves calculated by equation (4.27).

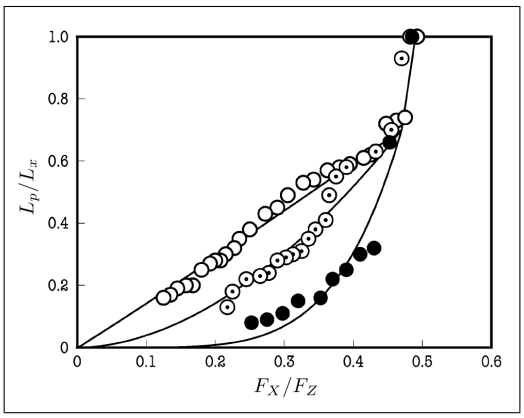

(b) Experimentally obtained result. Solid circle: $\theta = -0.833$, dotted circle: $\theta = 0$, open circle: $\theta = 0.833$. From [37], Figure 8.

Figure 4.9: The length of the precursors as a function of the applied tangential load right before the event in the model (left) and the experiments (right).

The opposite happens when $\theta > 0$. The static and dynamic friction levels are reduced at the trailing edge and increased at the leading edge. A lower tangential force is therefore needed in order to initiate a precursor of the same length. However, again the tangential force needed in order to initiate the first global event is approximately unchanged.

The corresponding experimental result is shown in Figure 4.9b, which shows a similar qualitative behaviour. However, looking at the values on the axes one discovers that the quantitative fit is quite bad. As mentioned in chapter 3, there appears to be a transition in the length of precursors at $L_p/L \approx 0.5$, but the model result contain no such transition. Generally, precursors get much further in the model than in the experiments for a given tangential load.

It should be noted that in the numerical result, precursors reaching as far as the previous one or shorter have been removed from the plot in order to make it cleaner. All points then correspond to a precursor that was longer than all the previous ones. This has not been done in the experimental results, where the number of precursors is equal to the number of dots of a specific type. It can now be seen quite clearly, that the number of precursors in the model is much too large compared to the experimental one.

Possible reasons for the deviation may be two-dimensional effects such as the Poisson effect mentioned in the previous section and the torque applied to the slider as a consequence of the tangential force F_X and the friction force. These possibilities will be discussed in more detail later.

4.6.2 Prediction of the length of a precursor

An analytical form for the function $L_p(F_X)$ can be found for the model using the observed shear force profile in Figure 4.8. When the system is at rest, the sum of all external forces has to be zero. This means that the driving force will equal the sum of all friction

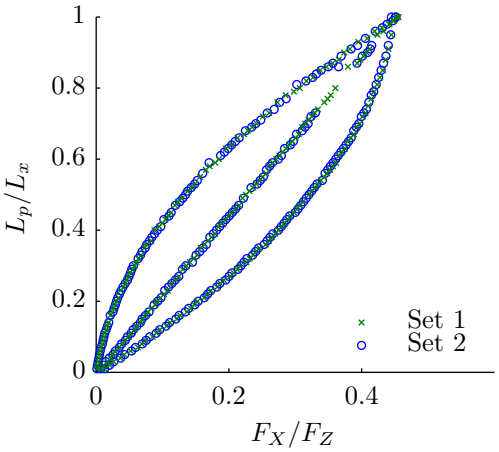

Figure 4.10: Length of precursors as a function of tangential load for two different parameter sets showing data collapse for $\theta = -0.833$, 0 and 0.833. Set 1 has $L_x = 50$ mm and $F_Z = 800$ N, while set 2 has $L_x = 100$ mm and $F_Z = 400$ N. Other parameters are as in Table 4.1.

forces from all blocks. At the same time, the sum of all internal forces in the system is zero because of Newton's third law. Therefore, the sum of the shear forces on each block equals the sum of the friction forces on each block, which in turn equals the driving force.

By assuming that the shear force is equal to the local dynamic friction on all blocks that have moved, and equal to the initial shear force for all blocks that have not moved, the driving force F_X can be found for a given precursor length. This assumption is quite good, as can be seen from Figure 4.8. With n_p being the block closest to the leading edge that moved during the event, all blocks from 1 to n_p have a shear force equal to the local dynamic friction, and the rest of the blocks have their initial shear force. The driving force is then

$$\boxed{F_X(n_p) = \sum_{n=1}^{n_p} \mu_d w_n + \sum_{n=n_p+1}^{N} F_n^{\text{n.f.}}(t=0),} \tag{4.27}$$

where the length of a precursor is given by

$$\boxed{L_p = \frac{n_p}{N} L.} \tag{4.28}$$

In Figure 4.8, the initial shear force on all blocks is zero, so the curves in Figure 4.9a are actually the sum of the dynamic friction forces on each block. This prediction is quite good, as can be seen from Figure 4.9a, where the curve predicted by equation (4.27) is plotted as black drawn lines.

Equations (4.27) and (4.28) also predicts data collapse for $L_p(F_X)$ for systems with different L_x and F_Z by plotting L_p/L_x as a function of F_X/F_Z, given that both w_n and $F_n^{\text{n.f.}}(t=0)$ are proportional to F_Z. Here, w_n is given by equation (4.11) and $F_n^{\text{n.f.}}(t=0) = 0$, meaning that data collapse should be obtainable. The axes in Figure 4.9a are already scaled accordingly, but all results are for the same slider length L_x and normal load F_Z. In Figure 4.10, $L_p(F_X)$ is shown for two different system lengths L_x and two different normal loads F_Z, and the result is a perfect data collapse.

The length of precursors then seems to be only weakly dependent on the dynamics of the micro-slip front propagation. The length of precursors might then be obtained from

quasi-static calculations, i.e. without considering the complete dynamics of the system. This is, however, beyond the scope of this thesis.

4.7 Time dependence of slip

As mentioned in chapter 3, the slip as a function of time has been measured for precursor events in the experiments [5], and it showed a quite interesting time development. In the discrete case, the slip along the interface equals the displacement of one block during an event. It is therefore of interest to compare the displacement of one block in an event to the slip measured in experiments.

The slip was measured in experiments where the slider was held stationary, and the tangential load was applied at the base. The current model may therefore not be fully accurate, but it is nonetheless interesting to investigate if any similarities can be observed between the model and experiments. The slip should not be highly dependent on the driving mechanism, since the driving velocity is very small compared to the rapid dynamics during slip.

The displacement of one block in an event can be seen in Figure 4.11a. As will be discussed in section 4.11, the slip length and duration of an event is highly dependent on the chosen number of blocks N. Therefore, a quantitative comparison with experiments involving the total slip length and slip time will not be done here. However the qualitative behaviour of the slip is also of interest. The motion depicted in Figure 4.11a is that of an acceleration up to a constant velocity, and then a deceleration back to zero velocity.

The experimentally obtained slip, seen in Figure 4.11b, shows much more complex behaviour, and the discrepancy between the model and experimental result is quite large. This is to be expected, since the rapid local heating of the interface to above the glass temperature and the succeeding cooling suggested to be the reason behind the slip curve shown in Figure 4.11b, discussed in chapter 3, is quite different from what a simple Amontons–Coulomb friction law will be able to reproduce. This result indicates that a much more sophisticated friction law will be needed in order to get a dynamical behaviour in better agreement with experiments.

4.8 Rupture velocities

As discussed in chapter 3, the rupture velocity is an important part of the experimental results. The rupture velocity can also be introduced in the model, making a comparison between model and experimental results possible.

In the model, the rupture velocity can be measured locally by considering the time from block $n-1$ started to move to block n started to. The distance between block $n-1$ and n is divided by the length of this time interval. The rupture velocity is then the inverse of local slope of the line separating the white and coloured regions of Figure 4.7. These velocities can be compared with both the experimental rupture velocities and the

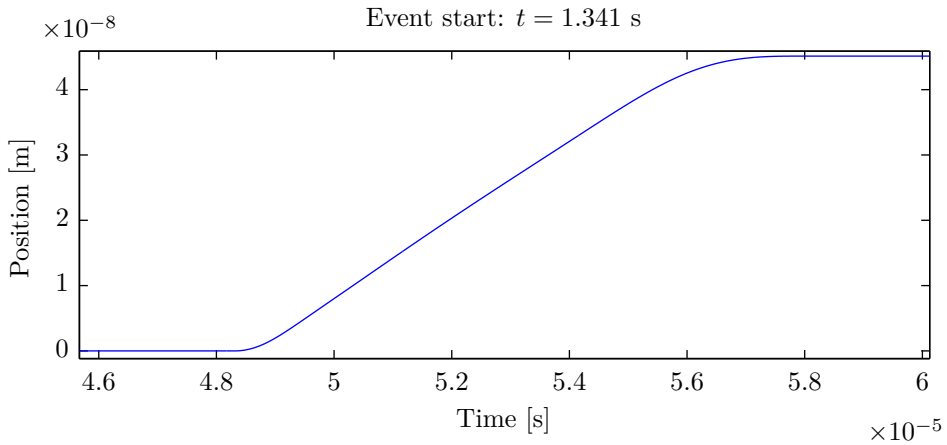

(a) Position of block 50 as a function of time for a simulation with $N = 100$ and $\theta = g = 0$ for the side driven model. The zero point for the position and time in this figure is the position of the block and time at the beginning of the event.

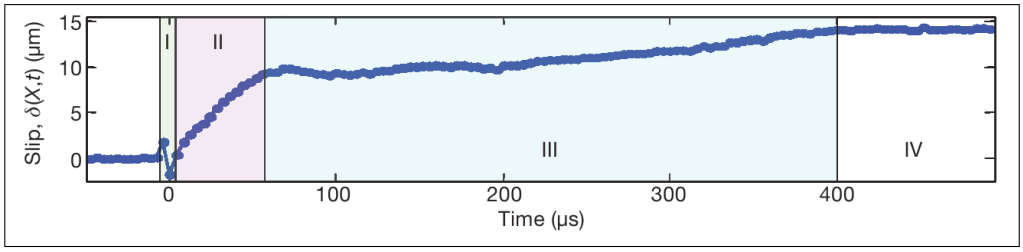

(b) Local slip δ measured at a X adjacent to the interface as a function of time. From [6], Figure 2a.

Figure 4.11: The slip as a function of time in the model (top) and in experiments (bottom) for a precursor event. A large discrepancy is shown, probably resulting from lacking physics in the modelling of the friction process.

velocity of sound in the model, which is given by [32]

$$\boxed{v_s = \sqrt{\frac{E}{\rho}}.} \tag{4.29}$$

The rupture velocity v_c for one event in the side driven model can be seen in Figure 4.12, where the shear force profile right before the event and the corresponding local rupture velocities are shown. This event is quite representative, there is not much difference between global events except the exact placement of the spikes in the shear force. The rupture velocity is per definition zero where the rupture started.

In Figure 4.13, the corresponding result from an experiment is shown. There are clearly variations in the in the rupture velocity, but they are much larger in the experimental data than the ones seen in the model results, and no intersonic front is seen.

The model is not expected to produce slow fronts, since the friction law contains no slow time dynamics. The low variation in the rupture velocity can possibly also be explained by the small variation in the initial shear to normal force ratio, because this was seen to have a large effect on the rupture velocities in the experiments, see Figure 3.4b.

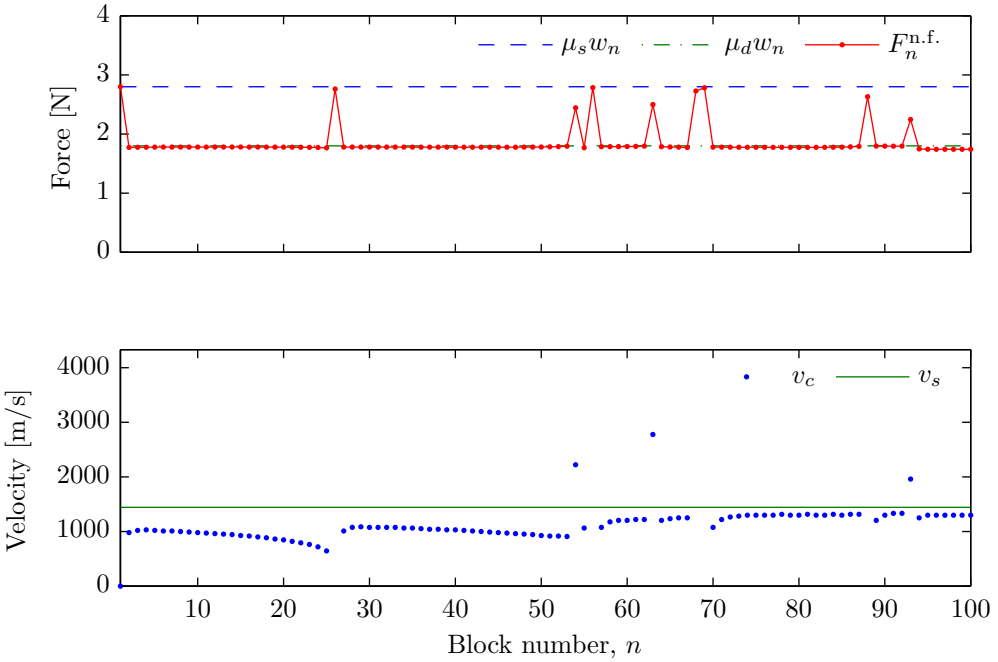

Figure 4.12: Result from the side driven model with standard parameters, $N = 100$ and $\theta = g = 0$. The topmost plot shows the shear force profile in the sample right before the global event. The lowermost plot shows the rupture velocities at different positions in the sample for the same event.

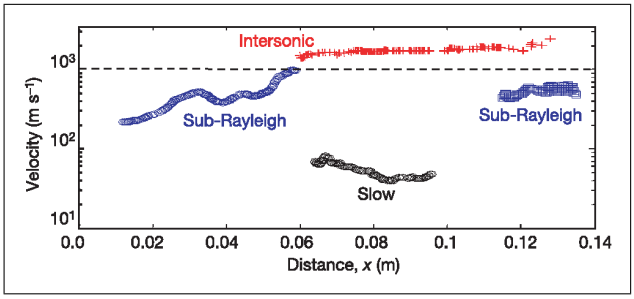

Figure 4.13: Experimental rupture velocity plotted as a function of position. The dashed line is the shear wave velocity. From [45], Figure 4b.

Since there seems to be a relationship between the initial shear ratio and the rupture velocity, it would be interesting to study this further. This is done in chapter 5, where the rupture velocities are studied systematically as a function the shear to normal force ratio.

4.9 Shear torque

In this section, the importance of shear torque on the length of precursors will be discussed, properly introducing the parameter g. First, the theoretical background will be presented, relating the size of this effect to the height at which the tangential load is applied. Then, this effect is included in the model, and it is then investigated if this effect could be the cause of the large deviations between the model and experimental results seen in the length of precursors $L_p(F_X)$.

4.9.1 Theoretical background

As known from classical mechanics, a force $\mathbf{F}$ will induce a torque $\boldsymbol{\tau} = \mathbf{r} \times \mathbf{F}$ around the centre of mass, where $\mathbf{r}$ is the vector going from the centre of mass to the point at which the force is applied. If the driving point P is above the interface, the driving force will induce a torque which will cause a reduction in the normal force at the trailing edge, and an increase in normal force at the leading edge.

This effect was proposed to be important in a top driven system [49], but here it is applied to a side driven system. This may not be appropriate, but it is anyway interesting to see what effects it might result in. The situation is illustrated in Figure 4.14. The block is assumed to be infinitely stiff, meaning that it does not deform in any way. In reality this assumption is of course not correct. However, the goal of this analysis is not make a detailed analysis of the effect of shear torque, but rather to get a better understanding of the consequences on the length of precursors.

The tangential force F_X is applied at a height h above the track. This induces a torque about the centre of mass that the normal force has to compensate in order to avoid rotation. The total normal force W is assumed to be linearly distributed according to the formula

$$w(x) = \bar{w}(x)\,\mathrm{d}x = \left(F_Z + g\frac{(x - L_x/2)}{L_x/2}F_X\right)\frac{\mathrm{d}x}{L_x}, \qquad F_Z = \int_0^{L_x} \bar{w}(x)\,\mathrm{d}x, \tag{4.30}$$

where F_Z is the applied normal force and assumed to be uniform. The form of equation (4.30) means that the torque leads to a linear redistribution of the normal forces, where the size of the non-uniformity is given by the parameter g. This is of course an approximation, in reality it is not linear, but it is expected to be accurate if the slider height is small compared to the length, see e.g. Figure 2 in [49]. Given the parameters in Table 4.1, $L_z/L_x = 0.2$, meaning that a linear approximation might not be accurate, but it is acceptable as a first approximation. The dependence of the parameter g on the pushing height h will now be investigated.

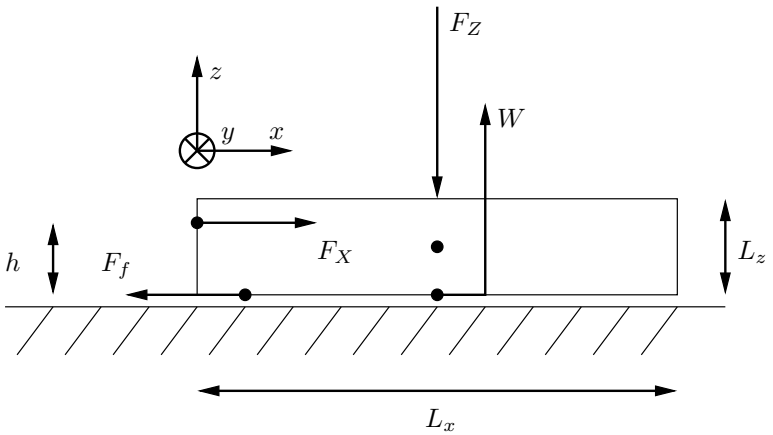

Figure 4.14: The forces acting on an infinitely stiff block. F_X is the applied tangential load, F_f is the friction force, and F_Z is the normal force.

The torque from the friction force F_f (F_f is negative) and the applied tangential load F_X (F_X is positive) is

$$\tau_{F_f} = -F_f L_z/2, \qquad \tau_{F_X} = F_X(h - L_z/2). \tag{4.31}$$

The total torque from the normal force, given a normal force on the form of equation (4.30), is

$$\tau_{F_Z} = -\int_0^{L_x} \bar{w}(x)(x - L_x/2)\,\mathrm{d}x = -\frac{g}{6} L_x F_X. \tag{4.32}$$

In the static case $F_f = -F_X$, and all torques should sum up to zero. Using equations (4.31) and (4.32) therefore leads to

$$\tau_{F_f} + \tau_{F_X} + \tau_{F_Z} = 0 \quad \Rightarrow \quad F_X h - \frac{g}{6} L_x F_X = 0,$$

which yields

$$\boxed{g = \frac{6h}{L_x}.} \tag{4.33}$$

This is then the relation between the pushing height h and the size of the shear torque effect g. $h > 0$ leads to $g > 0$, and the normal force on the trailing edge is reduced.

The discrete version of equation (4.30) is

$$\boxed{w_n = \frac{F_Z}{N} + \frac{g}{N}\left(\frac{2n - N - 1}{N - 1}\right) F_X, \qquad W = \sum_{n=1}^{N} w_n,} \tag{4.34}$$

where n indicates block $n = 1, 2, \ldots, N$. The normal force on the trailing edge block will be $w_1 = F_Z/N - gF_X/N$, while the normal force on the leading edge block will be $w_N = F_Z/N + gF_X/N$. Since $F_X > 0$ and $h > 0$, the normal force on block 1 will decrease and the normal force on block N will increase, as desired.

The normal force on block n will be zero if

$$\frac{F_Z}{N} - g\frac{F_X}{N} = 0 \quad \Rightarrow \quad g = \frac{F_Z}{F_X^{\max}}. \tag{4.35}$$

This means that if $g > F_Z/F_X^{\max}$, blocks may get a negative normal force, which is to say that the normal force is zero and the block is lifted above the track.

4.9.2 The effect of shear torque on the length of precursors

From equation (4.33) and the parameters given in Table 4.1, the maximal value for g when pushing on the block itself is

$$g_{\max} = \frac{6 \times 20\ \mathrm{mm}}{100\ \mathrm{mm}} = \frac{6}{5} = 1.2.$$

Simulations were done with $N = 100$, $\theta = 0$ and different values for g in order to investigate this effect, and the result can be seen in Figure 4.15. The figure shows that the shear torque causes the precursor propagation length to increase for lower values of the tangential force F_f. This effect actually causes the curves in Figure 4.15 to deviate more from the experiment. The reason for this is that the shear torque cases the normal force on the blocks on the trailing edge to be reduced, which means that the maximal static friction force on these blocks will decrease. The blocks will therefore start to slip for a lower tangential load.

This shows that it is not the shear torque effect alone which causes the deviations seen in Figure 4.9. Another mentioned cause is the large deviations in the shear force profiles, discussed in section 4.5.4. This will be investigated in the next section.

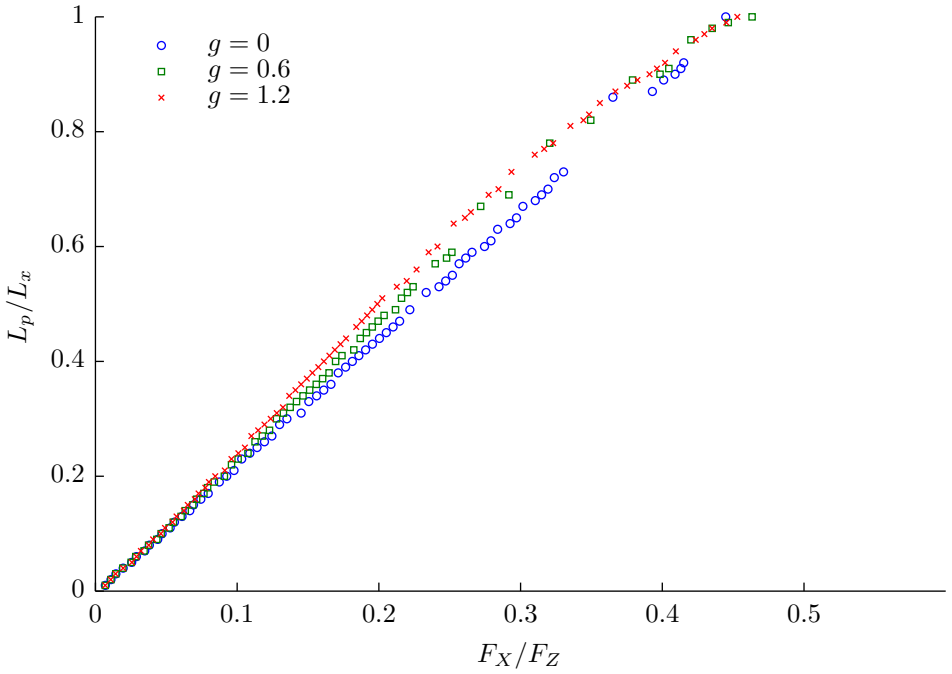

Figure 4.15: Plot of precursor lengths as a function of tangential force from simulations done with $N = 100$ and $\theta = 0$ for different values of g for the side driven model. This shows that the shear torque cause the precursors to propagate longer for lower values of the tangential force F_X.

4.10 Initial shear force profile

Another suggested reason for the deviation in the length of precursors between the model and the experiments was the shear force profile. There is not much that can be done about that without significant changes to the model, i.e. including the vertical dimension. However, the initial shear force profile can at least be chosen to be in better agreement with experiments.

The initial shear stress profile obtained from experiment can be seen in Figure 3.3b. This result is actually obtained from a slightly different experiment than that by Maegawa et al. [37] which has been used for comparison up until now. However, a better understanding of the effect the initial shear force profile has on the length of precursors can nonetheless be obtained by including a profile similar to that seen in Figure 3.3b. As a crude approximation, the functional form

$$F_n^{\text{n.f.}}(t=0) = s\frac{\mu_d F_Z}{N}\left(\frac{2n-N-1}{N-1}\right)^{2j+1}, \tag{4.36}$$

where $j = 1, 2, \ldots, n$ is the block number and s is a dimensionless constant is used. This is qualitatively compatible with the experimental results. The value of s determines the lowest and highest value of the initial shear force. By writing the exponent in this way, only antisymmetric shear profiles are included. This means that no driving force is required to balance the shear forces, because the sum of all friction forces on the sample is zero.

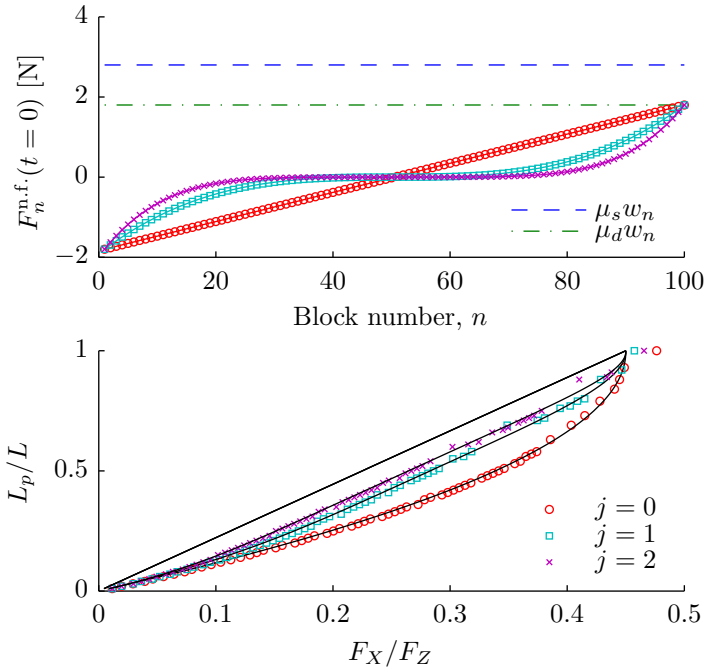

Figure 4.16: The bottom plot shows the $L_p(F_X)$-curves for different initial shear force profiles, seen in the top plot. The black lines are the curves calculated from equation (4.27), and the straight black line is the result from the model if the initial shear force is zero. $N = 100$, $\theta = g = 0$ and other parameters are as in Table 4.1.

The initial condition is then chosen according to equation (4.36) by using equation (4.16). The initial shear force profile will then only have an effect on the system until the first global event occurs. The result of simulations done with an initial shear profile chosen in accordance with equation (4.36) for $j = 1, 2, 3$ and $s = 1$ can be seen in Figure 4.16.

The effect is clearly visible. Because of the negative initial shear force on blocks 1 to 50, a higher tangential force is needed in order to initiate a precursor of the same length as before. The effect is reduced with increasing j since the initial shear force profile then flattens out. However, because the initial shear forces always sum up to zero, the tangential force needed to initiate the first global event is approximately the same. This effect does not explain all the discrepancies between the model and experimental length of precursors, but serves as another indication of the importance of two-dimensional effects on the $L_p(F_X)$ curve.

4.11 Scaling with the number of blocks

It was stated previously that the slip of one block during an event depends on the number of blocks. In addition, it was observed that the model has too many precursors and events in general compared to the experimental results. This can be traced back to the model's rather peculiar scaling with the number of blocks.

Starting out with the tangential loading and N_{sliding} curves, the result seen in Figure 4.5 is quite similar to that obtained in experiments, as discussed previously. However, this

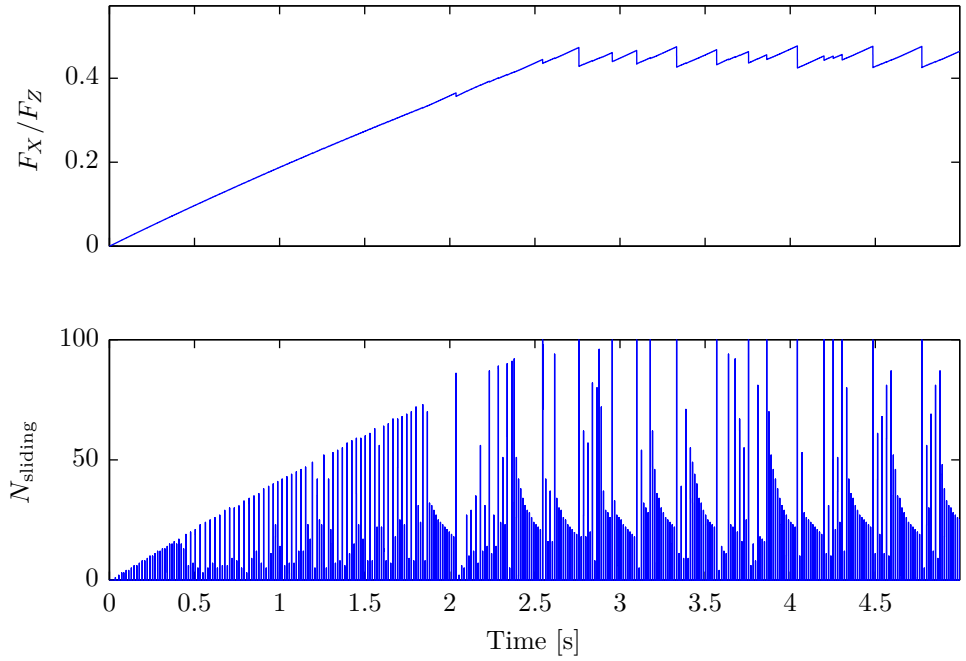

Figure 4.17: Result of the same simulation as shown in Figure 4.5 ($\theta = g = 0$), but with $N = 100$. The number of precursors increases, and the relative difference in tangential force between stick and lip periods decreases.

simulation result was obtained using only $N = 10$ blocks. The question is then what happens if the number of blocks now is chosen to be $N = 100$?

In Figure 4.17, the model result using $N = 100$ is shown. The number of events per time increases, and the relative change in the tangential force between stick and slip intervals decreases. For a more quantitative analysis, consider Figure 4.18, where the number of events in the first 20 s is plotted as a function of the number of blocks. The scaling is actually linear, causing the number of events to keep increasing as the number of blocks increases.

A consequence of this scaling is that the slip length, that is the length one block moves

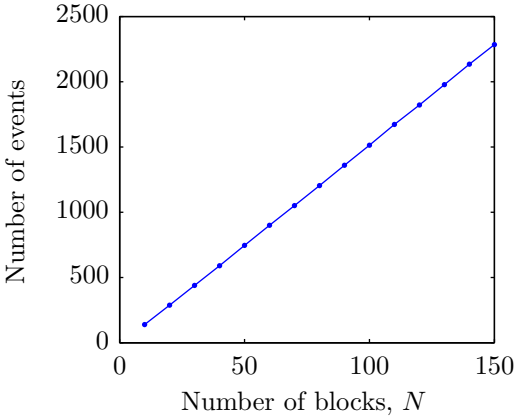

Figure 4.18: Plot of the number of events in the first 20 s of the simulation for the side driven model as a function of the number of blocks used.

in a single event, also will depend on the number of blocks. If the number of events per time increases, then the slip length of a block per event has do decrease to compensate for the fact that the whole sample's displacement per time is held constant (the driving velocity determines the displacement of the sample). As discussed previously, the slip length is a quantity measured in experiments, and consequently it should not scale with the number of blocks. The rupture velocities do not, however, seem to scale with N. By looking at the calculated rupture velocities for simulations done with different number of blocks, no clear trend is seen. This justifies the further study of the rupture velocities done in chapter 5 before the N-dependence is resolved.

This concludes the first discussion of the one-dimensional side driven model. The rupture velocities will be investigated further in chapter 5, where a systematic analysis of the dependence on the initial state will be done. The scaling of the side driven model will be discussed further in section 6.1: by understanding the reason for this particular scaling, a possible solution can be found by modifying the static friction law.

4.12 The one-dimensional model with top driving

In the side driven one-dimensional model, only the trailing edge block was driven. This is a rather peculiar way of driving the system, because in the real system, a finite region about the point where the driving force is applied will be affected. The reason for this is the elastic properties of the material, which will distribute the applied force some distance into the sample. This distance will depend on e.g. the height at which the driving is applied and the size of the driving force itself.

In addition, all events nucleate at the trailing edge block in the side driven model. In the experiments where the slider was held stationary and the tangential force was applied to the base block, events were seen to nucleate elsewhere along the interface as well.

It is therefore interesting to examine what the consequences of adding a driving force to other blocks is. In the top driven one-dimensional model, depicted in Figure 4.19, each block is connected to an infinitely rigid plate by springs with spring constants K_n. The springs are modelled as leaf springs, meaning that the spring forces only act in the x-direction and that they are proportional to the displacement in the x-direction only. The plate is moving at a constant velocity V. Using this driving mechanism, the one-dimensional model will be equal to the Burridge–Knopoff model, mentioned above.

The only difference between the side and top driven model is therefore the form of the driving forces F_n^K, which in the top driven model is given by

$$\boxed{F_n^K = K_n(Vt - u_n), \qquad n = 1, 2, \ldots, N.} \tag{4.37}$$

The equations of motion, shear force and total driving force are then still given by equations (4.5), (4.6) and (4.3), respectively. The driving spring constants K_n are chosen equal to K/N, where K is the driving spring constant in the side driven model. This ensures that the same amount of force will be applied to the system in a given amount of time as in the side driven model when all blocks are stationary. In addition, all blocks are driven equally. The top driven model is in other aspects equal to the side driven model. This driving method should be more similar to the experiments where the slider is held stationary and the tangential load is applied at the base instead.

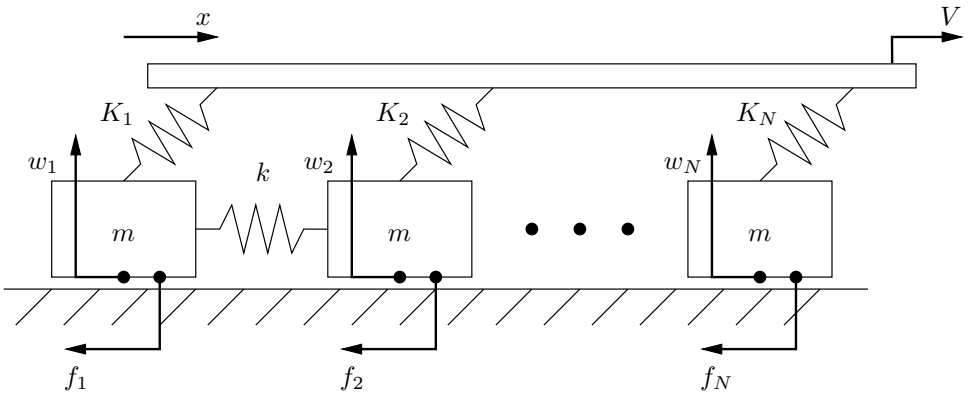

Figure 4.19: This figure shows the top driven system, where each block is connected to a plate moving at a velocity V. The springs with spring constant K_n are leaf springs, meaning that the spring forces only work in the x direction and that the force from one such spring on block n is given by $K_n(Vt - u_n)$.

Results obtained for the top driven model will now be presented. The discussion will not be as thorough as for the side driven model since the differences between the two models are emphasised.

4.13 First model results

As for the side driven model, the stick-slip behaviour exhibited by the model and the time development of the shear force, which turned out to explain a large part of the results for the side driven model, will be presented in this section.

4.13.1 Stick-slip behaviour

In the top driven model all blocks will start sliding simultaneously if there is no asymmetry in the system, since all blocks will then experience the same driving force and have the same static friction level. In order to get precursors, an asymmetry therefore has to be added to the system. This is done in two different ways; by having a shear torque, and by imposing a non-uniform normal load.

The stick-slip plot is shown in Figure 4.20 for $\theta = 0$ and $g = 1.2$. The general behaviour looks much the same as that depicted in Figure 4.5 for the side drive model. However, the static friction coefficient has been reduced to $\mu_s = 0.55$ in order to get some precursors at all. This is done at the cost of reducing the drops in the shear force for each event, which has become rather small compared to the experimental result in Figure 3.2a.

Removing the shear torque effect, adding a non-uniform distribution of normal weights and again setting $\mu_s = 0.7$, results in Figure 4.21. There are now both larger drops in the shear force during an event and a higher number of precursors.

The roles of the local friction coefficients μ_s and μ_d seem not to have changed: the static friction coefficient determines the size of the drops in the tangential force during an event and the dynamic friction coefficient determines the average level of the $F_X(t)/F_Z$-curve.

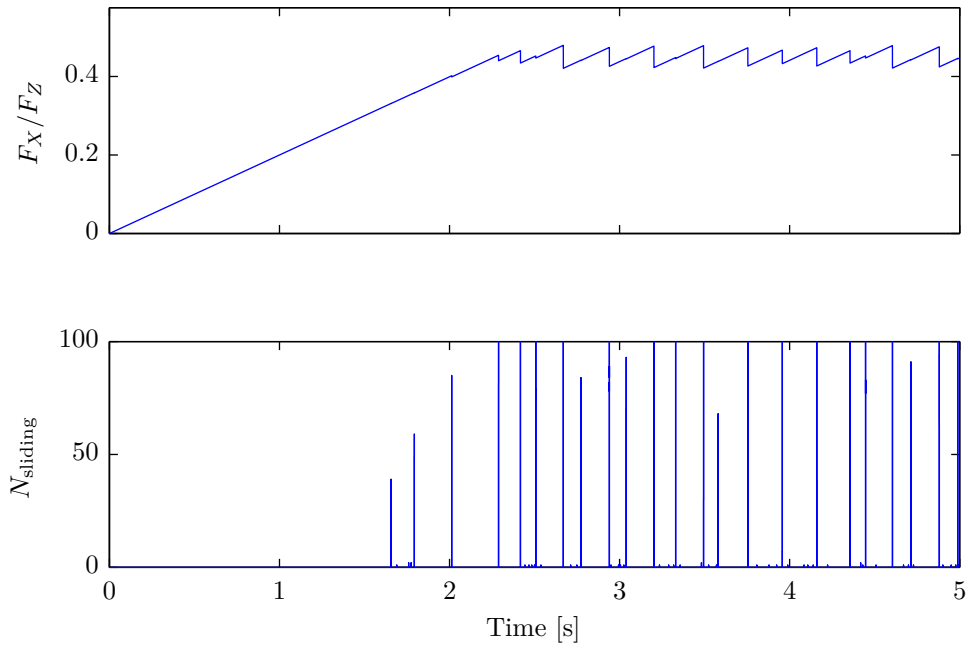

Figure 4.20: The uppermost plot shows the tangential force as a function of time normalised by the total normal load for $N = 100$, $\theta = 0$, $g = 1.2$ and $\mu_s = 0.55$ for the top driven model. The temporal evolution resembles that seen for the side driven model, but the precursors are fewer and bigger, as can be seen in the lowermost plot depicting the number of moving blocks.

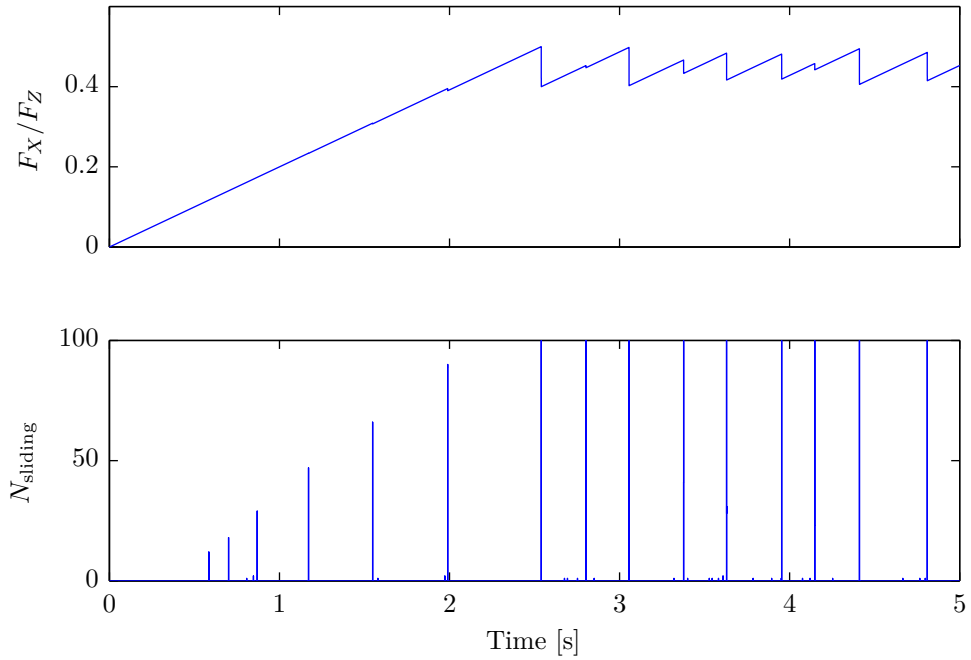

Figure 4.21: The top plot shows tangential force as a function of time normalised by the total normal load for $N = 100$, $\theta = 0.833$ and $g = 0$ for the top driven model. The number of precursors is now larger than that seen in Figure 4.20.

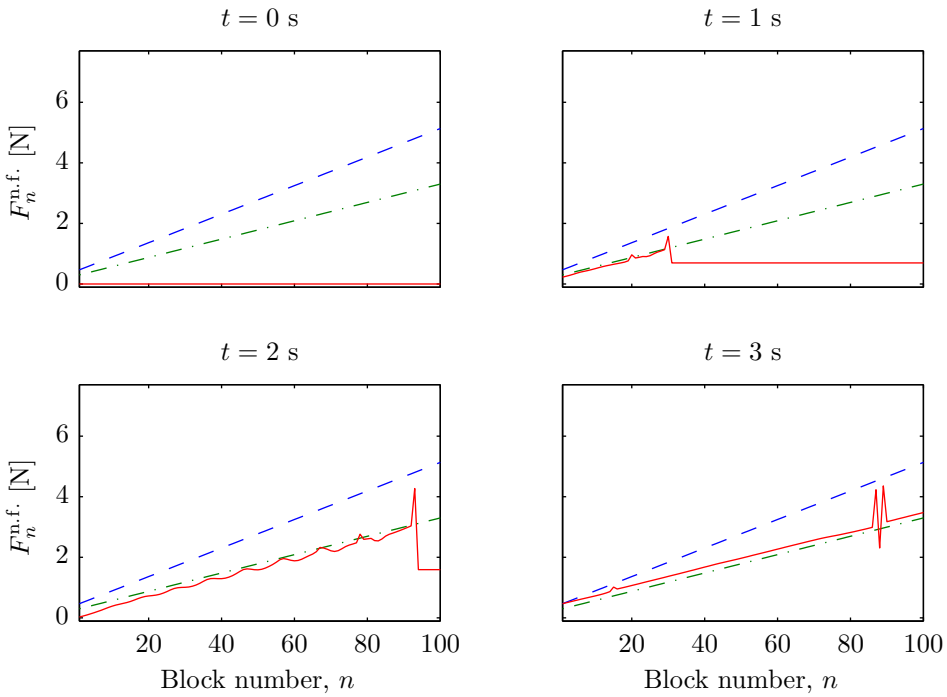

Figure 4.22: Plots of the shear force profile in the sample at different times with $N = 100$, $\theta = 0$ and $g = 0$ for the top driven model. The long dashed line is the level of local static friction, the dashed-dotted line is the level of local dynamic friction, and the drawn line is the shear force profile. The time development of the driving force can be seen in Figure 4.21.

4.13.2 Shear force profile

The shear force profile for the top driven model with $\theta = 0.833$ and $g = 0$ is plotted in Figure 4.22 for four different times. The shear force lies approximately on the level of dynamic friction where blocks have slipped as in the side driven model. However, in the side driven model, the shear force was unaltered where slip had not occurred. This is not the case for the top driven model, where the shear force will increase with time in non-slipped regions due to the increased driving force. This can clearly be seen in Figure 4.22 at $t = 1$ s and $t = 2$ s.

It will later be shown that this property results in a much better scaling with the number of blocks N compared to the side driven model.

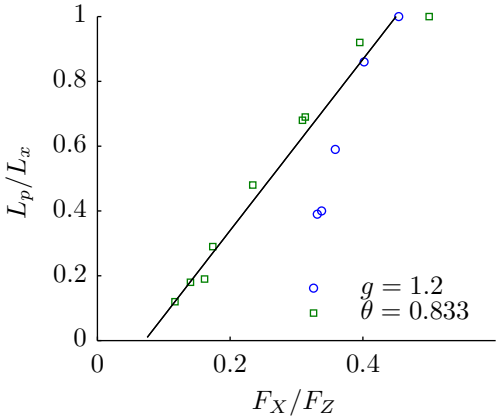

Figure 4.23: Length of precursors L_p as a function of the applied tangential load F_X. The $g = 1.2$ simulation has $\theta = 0$ and $\mu_s = 0.55$. The $\theta = 0.833$ simulation has $g = 0$, $\mu_s = 0.7$. The drawn black line is the analytical curve calculated from equation (4.38) for $\theta = 0.833$. Other parameters are as in Table 4.1.

4.14 Precursor lengths

In this section follows the results for the precursor lengths for the top driving. First, the precursor lengths will be investigated numerically for both a shear torque and a non-uniform normal load. Second, it will be shown that the length of a precursor can again be predicted from the applied tangential load in an easy way if $g = 0$.

4.14.1 Model results

The precursor length plot for the top driven model with $\theta = 0.833$, $g = 0$ and $\theta = 0$, $g = 1.2$ can be seen in Figure 4.23. The non-uniform normal load, $\theta = 0.833$ is seen to result in an approximately linear $L_p(F_X)$ dependence. If shear torque is included instead, $g = 1.2$, the model is seen to result in a few quite long precursors requiring a high tangential load.

None of these results can be considered to be in better agreement with the experimental results than the side driven model. That is, however, not very surprising since experimental $L_p(F_X)$ data exists only for systems where the tangential load is applied at the slider.

4.14.2 Prediction of the length of a precursor

Calculation of the precursor lengths will now be done assuming $g = 0$ and no initial shear force profile. In order to do this, the shear force profile must be known for a given precursor length n_p. Using the observations done in section 4.13.2, a schematic drawing of the shear force profile for a precursor length n_p can be made. This is shown in Figure 4.24: the shear force on a block is assumed to be equal to the dynamic friction level if it has moved during the event. At the same time, blocks that have not moved still have an increased shear force, and this level has to be found.

If no blocks have slipped, the shear force on block n would be $K_n Vt$. According to Figure 4.24, blocks with a dynamic friction level below $K_n Vt$ have moved, and the shear force has been reduced to the dynamic friction level. The total excess force is then the sum of the difference between the dynamic friction level and the unslipped shear

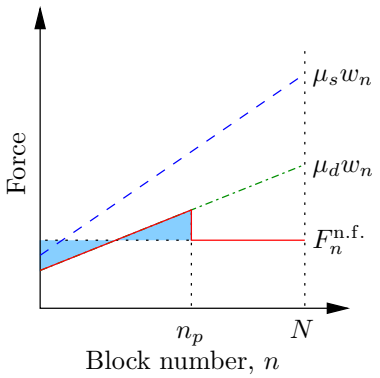

Figure 4.24: Schematic illustration of the shear force profile in the top driven model for a precursor of length n_p immediately after the event ended.

force level. This total excess force is used to lift some of the blocks that have not slipped up to the dynamic friction level. In Figure 4.24, the excess force is illustrated as an area (the leftmost coloured triangle). The area of the rightmost coloured triangle is the force needed to lift the additional blocks up to the dynamic friction level.

From the model results in Figure 4.22, it seems like these two areas are equal. That would mean that the tangential force F_X is not reduced during a precursor event, and as seen in Figure 4.21, this is almost true. The reason is the soft driving springs $K_n \ll k$: the precursors do not lead to a displacement large enough to reduce the driving spring forces considerably. The two coloured areas in Figure 4.24 are therefore assumed to be equal in the rest of this derivation.

The driving force can now be found by summing up the shear force on each block for a given precursor length n_p. The shear force is known in the slipped region, and in the unslipped region the force equals the average of the dynamic friction level at the trailing edge (block 1), and the dynamic friction level on block n_p. The driving force is then given by

$$\boxed{F_X(n_p) = \sum_{n=1}^{n_p} \mu_d w_n + \frac{\mu_d w_{n_p} + \mu_d w_1}{2}(N - n_p),} \tag{4.38}$$

and the length of a precursor is still given by equation (4.28). The black line in Figure 4.23 is calculated using this formula. Equation (4.38) is seen to give a fairly good approximation of the $L_p(F_X)$-curve.

4.15 Rupture velocities

Since the top driven model is more similar to the experimental setup where the tangential load is applied at the base, and rupture velocities were also measured for this driving mechanism, it is interesting to study the rupture velocities in this model as well. In this section, the rupture velocities in the top driven model with a non-uniform normal load are discussed. These ruptures do not have to nucleate at the trailing edge, but will be seen to nucleate near the trailing edge since only $\theta > 0$ will be used.

In Figure 4.25, the rupture velocity and the shear force profile right before the event is shown for a typical event using $\theta = 0.833$. The event is seen to nucleate at block 11 and then propagate both towards the trailing and leading edge.

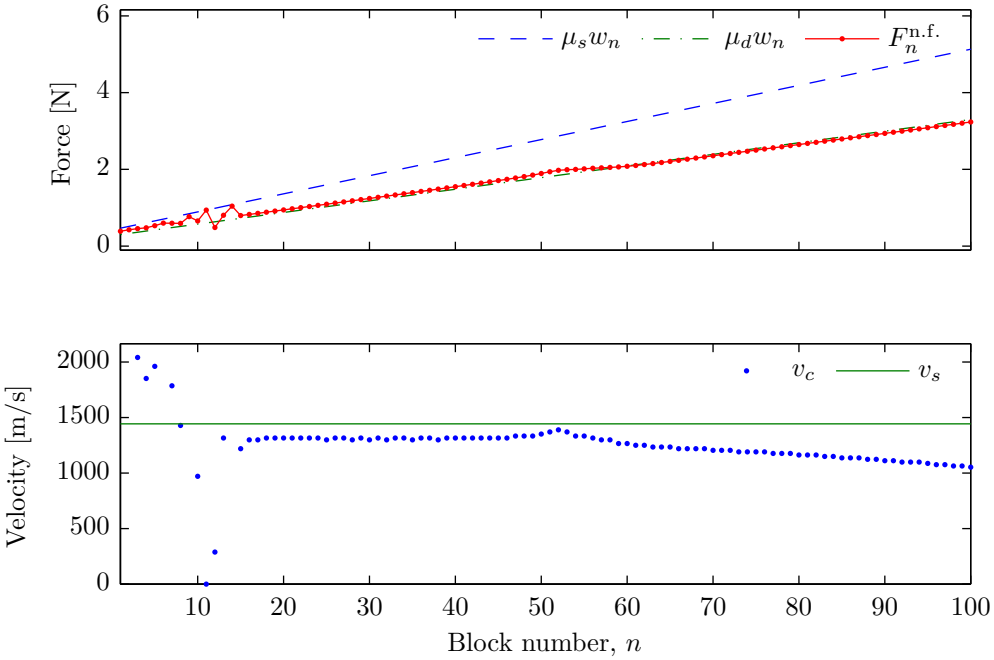

Figure 4.25: Shear stress profile right before and event (top) and the corresponding rupture velocities (bottom) for the top driven model with $N = 100$ and $\theta = 0.833$.

The corresponding result for a smaller non-uniformity in the normal load can be seen in Figure 4.26, where $\theta = 0.3$ is used. This leads to a larger variation in the initial shear force, which in turn is seen to cause a rather large variation in the rupture velocity. Again there seems to be a close relationship between the initial shear force and the rupture velocity.

In [5], the local rupture velocity was plotted as a function of the local stress ratio. Such a plot was not made for the side driven model, since the variation in the rupture velocity and initial shear force was quite small. Using a small non-uniformity in the top driven model, however, seems to result in much larger variations in both initial shear force and rupture velocities. As a first attempt in trying to better understand the rupture velocities in the model, such a plot is now made using $\theta = 0.3$. The corresponding plot for $\theta = 0.833$ is similar, but with a smaller range in the shear stress ratio.

The result is given in Figure 4.27a, where each point is the mean value of the neighbouring points inside a distance of 3 mm from the chosen measurement point. Velocities above 5 km/s are discarded. The measurement points are chosen to be in agreement with those used in the experiment. This means that, even though the experimental slider was longer, the relative position of the points are the same.

The model result in Figure 4.27a should be compared with the experimental result given in Figure 4.27b. Some features are seen in both the model and experiment: The rupture velocity is both below and above the shear wave speed, and an increasing stress ratio seems to favour larger rupture velocities.

However, there are serious deviations between the model and experiments. Firstly, the low creep velocities are missing. This is probably because of the friction law imposed

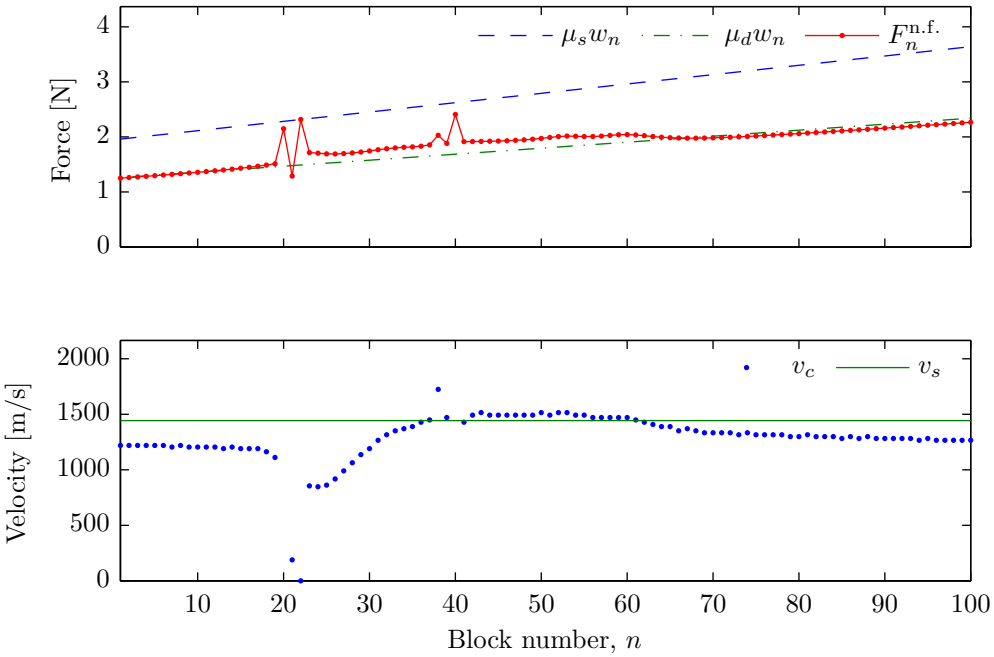

Figure 4.26: Shear stress profile right before and event (top) and the corresponding rupture velocities (bottom) for the top driven model with $N = 100$ and $\theta = 0.3$.

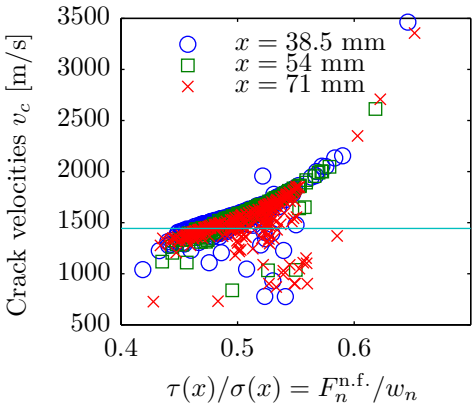

(a) Result from for the top driven model. Rupture velocities measured at different positions in the sample as a function of the ratio between shear and normal stress. The horizontal line is the velocity of sound in the one-dimensional model. $N = 100$, $\theta = 0.3$, other parameters as in Table 4.1.

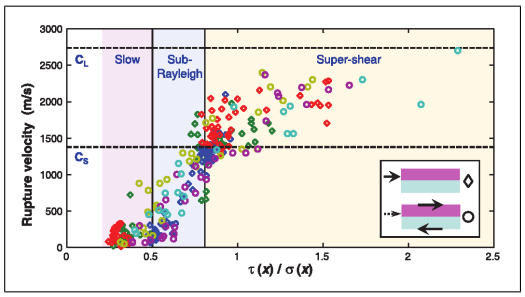

(b) Experimental result. Different markers represent different drivings, and different colours indicate different positions along the interface. c_l and c_s are the longitudinal and shear wave velocity in PMMA, respectively. From [5], Figure 3.

Figure 4.27: Rupture velocities as a function of the local stress ratio right before the event in the top driven model with $\theta = 0.3$, $g = 0$ (left) and in experiments (right). Each point in each colour corresponds to one event at a given location.

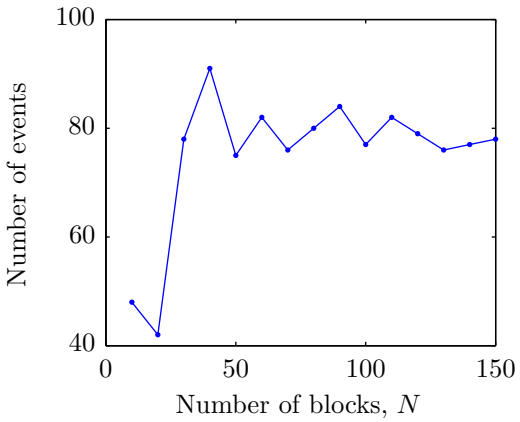

Figure 4.28: Plot of the number of events in the first 20 s of the simulation for the top driven model as a function of the number of blocks used. $\theta = 0$, and all other parameters are as in Table 4.1.

between the blocks and the track, which does not favour a creep-like motion: blocks are either moving or not moving. Secondly, the large local stress ratio observed in experiment is not present in the model. The reason for this is that in the model, the local stress ratio cannot exceed the local μ_s, because if it does, the block will move. The rupture velocities will be studied in more detail in chapter 5, where the initial stress ratio will be manipulated in order to investigate the relationship between rupture and stress more closely.

4.16 Scaling with the number of blocks

The side driven model had a rather peculiar scaling with the number of blocks. The top driven model, on the other hand, does not show the same scaling behaviour. The number of events as a function of the number of blocks for the top driven model, corresponding to Figure 4.18 for the side driven model, is shown in Figure 4.28. The number of events is seen to be roughly constant as a function of the number of blocks used in the simulation. This can be understood by again considering the shear force profile. Looking at Figure 4.24, one can observe that the force needed to initiate at least the first precursor will not depend on the number of blocks.

Between subsequent events, the additional tangential load applied will not depend on the number of blocks either. The reason for this is that all blocks feel the same increase in the driving spring force. The spikes in the shear force seen in Figures 4.25 and 4.26, which are seen to determine where an event nucleates, act as the trigger. However, in order for this spike to reach the static friction level, the shear force on all blocks is increased. This argument will become clearer as a possible solution to the scaling problem of the side driven model is presented in section 6.1.

4.17 Robustness of the results

It is important to investigate the robustness of the results, that is, how the results change if modifications are made to either the parameters or the model itself. The model results should not change to a large degree if only small modifications are made. In this section, the robustness of the results presented in this chapter will be discussed.

The consequences of changing the local friction coefficients have been discussed previously. Varying the local dynamic friction coefficient changes the global static friction coefficient: μ_d is actually approximately the global static friction coefficients obtained from simulations. Changing the local static friction coefficients changes the variation of the tangential load through an event. As long as both are within reasonable limits, they do not change the qualitative behaviour of the system, and the quantitative behaviour is to a large degree understood.

However, there is no disorder included in this model. In reality, the strength of the interface will vary, and the model is therefore in a rather unique regime. One might therefore fear that adding e.g. a small randomness in the friction coefficients will change the results. This have been done, and as long as the variation is not too large (a few percent of the mean friction coefficient or less), the results presented here do not change.

As long as the driving spring is soft ($K \ll k$), the results do not depend on the driving either. The same goes for the driving velocity: as long as it is slow, the results do not change. However, if the driving velocity is increased too much (on the order of the maximum velocity of the blocks during an event or more), the stick-slip behaviour disappears.

The model is not very sensitive to changes in η. The value of η was originally chosen in such a way that it should minimise the unwanted oscillations while still keeping the rest of the dynamics mostly unchanged. Reducing the value of η leads to an increased amplitude of the unwanted oscillations, while increasing it reduces them even more. The effect on the shear force profile is easily seen, but the effect on other results such as precursor lengths is small as long as η is not increased too much ($\eta \gg \sqrt{km}$).

4.18 Summary and conclusion

In this chapter, a one-dimensional spring-block model has been used to model the onset of friction and the stick-slip regime between two blocks of PMMA. Two different driving mechanisms have been used, side and uniform top driving, and Amontons–Coulomb friction has been used as the local friction law.

The results have been compared with recent experimental results. Most of the model results are qualitatively comparable to the experimental results, if not always in good quantitative agreement. It has been suggested that the main reason for these deviations, at least in the length of precursors as a function of the tangential load, are due to effects caused by the vertical dimension not included in the one-dimensional model. This was suggested because of the improved behaviour of $L_p(F_X)$ if an initial shear stress profile was included. Adding a vertical dimension will also cause a non-uniform distribution of normal stress at the interface, which in turn may change the $L_p(F_X)$ curve as well. This idea has been pursued by Trømborg [56], and the reader is referred to his master's thesis for a more detailed discussion.

As a purely mathematical model, the side driven one-dimensional spring-block model shows a rather bad scaling with N. The number of events per time was shown to increase linearly with the number of blocks, which makes a comparison with the experimental results on the number of events meaningless. From a mathematical point of view, the accuracy of the model should increase if the resolution is increased.

From a physical point of view, however, it is expected that as the resolution is increased, leading to a decreased size of each block, the Amontons–Coulomb friction laws applied here will not be reasonable. With decreasing block sizes, the number of asperities per block is reduced. Since the Amontons–Coulomb laws are only valid if the number of asperities is large, such that a statistical average of the behaviour of a single asperity is reasonable, the friction law applied here is expected to break down for large N.

Despite this, it is still useful to consider the model's continuum limit, $N \to \infty$. As discussed above, the rupture velocity does not seem to scale significantly with N. A more detailed analysis will be made in chapter 5. In addition, the rather peculiar scaling of the model will be shown to be a consequence of the highly singular driving, rather than the friction law itself in chapter 6. Trømborg [56] has also shown that this problem is solved in a two-dimensional model, which is due to the fact that the loading region (the region affected by the driving force) then no longer depends on N.

Even though the one-dimensional model shows significant discrepancies compared to the experimental results, it is still a very useful study. The model introduces important concepts, such as the shear force profile, that seems to be important for e.g. the length of precursors and the rupture velocities.

It has been shown that the length of precursors as a function of the tangential load can be calculated from a purely geometric argument. The dynamics of each event then does not seem to be important, rather, it is the fact that the average block end up at the local dynamic friction level after an event which is important.

Rather than including the vertical dimension in the simulation, the second horizontal dimension could also be included. This might lead to new interesting behaviours, since the importance of this dimension is unclear. A $(2 + 0)$D block model will be presented in chapter 7 as an alternative to the $(1 + 1)$D model presented in [56], and the effects induced by the second horizontal dimension are investigated.

Chapter 5

Rupture velocities

As mentioned in chapter 3, the velocity of the micro-slip fronts propagating along the interface when slip initiates are one of the mysterious results from the experiments. In earthquakes, one of the important parameters governing the damage is the fault rupture velocity. It has therefore been under close investigation, both theoretically and numerically, for the last 60 years. It was believed that the rupture velocity is limited by the Rayleigh wave speed, but it has later been shown that supershear ruptures are possible. They are, however, limited by the longitudinal wave speed. It is only recently that such supershear ruptures have been observed, see e.g. [26] for a brief summary and references.

In the experiments presented in chapter 3, the ruptures velocities are divided into three modes of rupture: slow ruptures, characterised by velocities much less than the material wave speeds, sub-Rayleigh ruptures, with velocities less then the Rayleigh wave speed, and the supershear ruptures, where the velocities exceed the shear wave speed. This is illustrated in Figure 3.4b. The sub-Rayleigh ruptures are considered well understood theoretically, but for slow and supershear ruptures, both the rupture process and their importance in e.g. earthquakes are still not clear [5].

Studies of rupture velocities in the Burridge–Knopoff model with Amontons–Coulomb friction have previously been done by Knopoff et al. [34] and Muratov [39]. Knopoff et al. went to the continuum limit of the Burridge–Knopoff model and obtained a set of partial differential equations describing the propagation of rupture. The possibility of prestress in the driving springs was included, and this prestress could vary along the interface. Muratov studied ruptures in the discrete Burridge–Knopoff model given a constant prestress in the driving springs, and arrived at a relationship between the initial shear stress and rupture velocity.

The Burridge–Knopoff model, is only one of the many that has been used for studying rupture. Finite difference methods [1] and analytical calculations [18] are also widely used. Shi et al. [52] recently used the finite element method to study dynamic ruptures, and observed both sub- and supershear ruptures. The referred articles are only three examples, and the reader is again referred to [26] for a more complete summary and list of references.

In 2009, a spring block model was presented in which slow rupture fronts were observed [16]. This model is quite similar to the model used here, but the Amontons–

Coulomb friction law had been replaced by a time dependent friction law. Slow ruptures have also been observed by imposing an elasto-plastic inspired friction law [9]. Despite this, however, the physical processes causing slow ruptures are not yet understood.

From experiments, there seems to be a close relationship between the local stresses along the interface and the corresponding rupture velocity. In the model, the initial stresses and the strength of the interface can be manipulated. This leads to the possibility of a systematic investigation of the relationship between stresses, interfacial strength and rupture velocities, which may in turn lead to a more detailed understanding of the rupture process.

A short discussion of the rupture velocities in the side driven one-dimensional model was done in section 4.8. In this chapter, the rupture velocities in this model will be studied in more detail, both through numerical simulations and analytical calculations. First, a uniform system will be studied, where the initial stresses and friction coefficients are constant along the interface. Second, the consequences of non-uniformity will be studied, where the initial stresses and/or friction coefficients may vary along the interface. This study is therefore not limited to analysing the recent experimental results, but may also be of interest to e.g. fault rupture propagation in earthquakes.

The approach used by Muratov will be applied here to investigate the rupture velocities in the side driven model analytically. The prestress is in the side driven model stored in the material springs, not in the driving springs, but much remains the same compared to the Burridge–Knopoff model. The results obtained here will then be used to study systems with non-uniform initial shear stresses.

Throughout this chapter, $\eta = 0$, since it is the rupture process inherent in the Amontons–Coulomb friction law that will be studied. Including a relative viscous damping is seen to have a quantitative effect on the results, but the qualitative behaviours remain. It should be possible to apply techniques used here to a system with $\eta \neq 0$, but that is not within the scope of this thesis.

5.1 Uniform prestress

In this section, only systems with a uniform initial shear force will be studied. However, this allows both simulations and analytical calculations to be done, providing a good understanding of the rupture velocities in the model. This will in turn be used to understand the rupture velocities in systems with a non-uniform prestress.

5.1.1 Simulation results

First some computational remarks: how to choose the initial shear force level is described in section 4.3, giving the position of all blocks for a given initial shear force. The rupture is forced to nucleate at the trailing edge by increasing the load on the first block until it reaches its static friction level. The simulation does not have to include anything more than the time from the rupture initiates to the time where it has reached the leading edge, causing the simulation time to be much smaller than previously. Because of this, the number of blocks used in the simulations can be increased, and results in this section

are obtained with $N = 1000$ and an integration time step of $\Delta t = 1 \times 10^{-11}$ s or smaller, or $N = 2000$ and $\Delta t = 5 \times 10^{-12}$ s or smaller.

The simulation results for two different initial shear force levels are shown in Figure 5.1. The initial shear force profile and the rupture velocity as a function of n and $1/n$ is shown, where the lowermost figure has an initial shear force closest to the dynamic friction level.

In Figure 5.1a, the rupture velocity appears to converge to some constant value after a transient. However, in Figure 5.1b, the rupture velocity does not reach a constant value, but continues to increase throughout the sample. When the rupture velocity is plotted as a function of $1/n$, it is clear that it is actually converging, but the transient is rather long. In order to estimate this final velocity, a linear extrapolation is done, as illustrated by the red lines extending from the curves in the rightmost plots.

The asymptotic rupture velocity can now be calculated for many different initial shear force levels, the result can be seen in Figure 5.2, where it is plotted as a function of the initial shear force. The blue (upper) curve shows the velocity obtained by using the parameters given in Table 4.1. In all cases, $v_c > v_s$, and the rupture velocity seems to approach the velocity of sound as the initial shear force approaches the dynamic friction level. In addition, it appears to diverge to infinity as the initial shear force approaches the static friction level.

This can be understood by considering the situation where all blocks are loaded infinitely close to the static friction level. A block then has to move an infinitesimal distance in order for the next block to reach the static friction level and then start moving. The time between the triggering of two blocks is then an infinitesimally small time, causing an infinite rupture velocity.

The blue (upper) curve in Figure 5.2 was, as stated above, calculated for a given Young's modulus, density, normal force and static and dynamic friction coefficients. It is to be expected that the curve will change if these parameters are changed, and as shown by the cyan (lower) curve, this is indeed the case. In this simulation, Young's modulus and the friction coefficients were changed, leading to a different sound velocity and different limits for the initial shear force. However, the qualitative behaviour appears not to have changed, and it should therefore be possible to collapse these two curves onto each other.

This is indeed possible by assuming that the rupture velocity as a function of the initial shear force has the form

$$\boxed{v_c(F^{\text{n.f.},0}) = v_s \bar{v}_c\left(\bar{\tau}\right), \qquad \bar{\tau} = \frac{F^{\text{n.f.},0} - \mu_d w}{(\mu_s - \mu_d) w},} \tag{5.1}$$

where a dimensionless initial shear force $\bar{\tau}$ has been introduced. This is then the only parameter included in the function $\bar{v}_c(\bar{\tau})$. The collapse of the two graphs can be seen in Figure 5.3. The collapse is actually so good that only one curve is visible, suggesting that the rupture velocity indeed has the functional form given in equation (5.1). This scaling is the same as that obtained by Muratov [39], suggesting a close relationship between the rupture velocities in the Burridge–Knopoff model and the side driven model considered here. In section 5.1.2 the function $v_c(F^{\text{n.f.},0})$ will be calculated, proving the scaling given above.

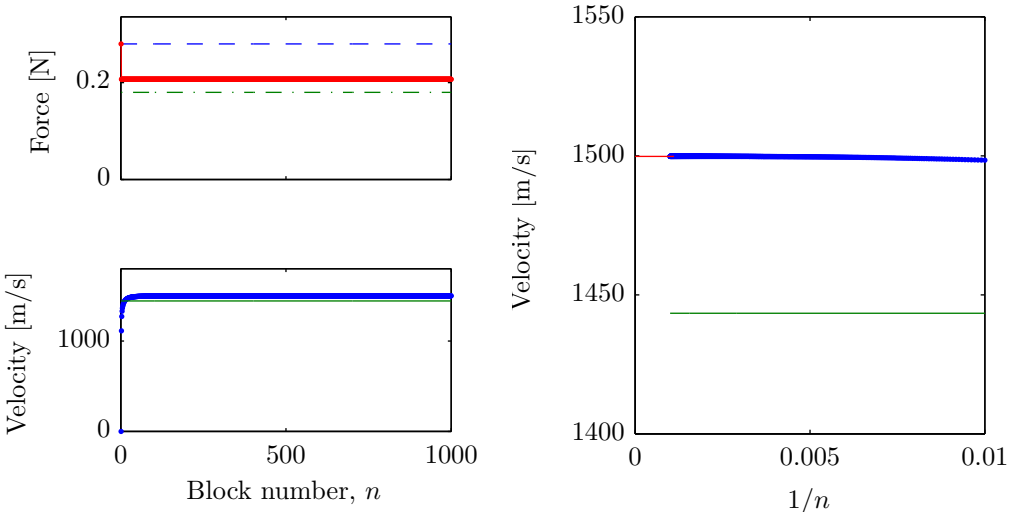

(a) Result from simulation with $F_n^{\text{n.f.},0} = 1.15 \times \mu_d w_n$. The two left plots are the shear force and rupture velocity as shown previously, while the right plot is the rupture velocity plotted against the inverse of the block number.

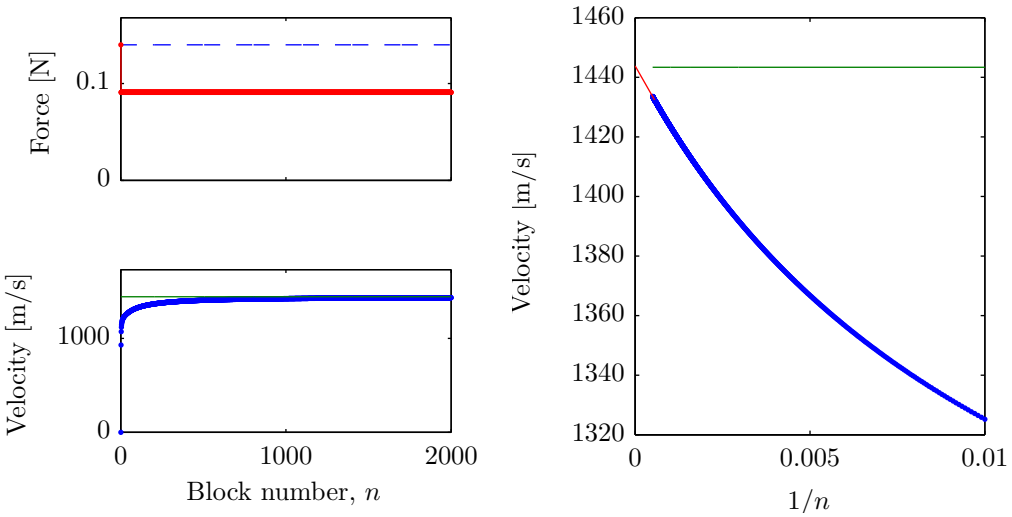

(b) Result from simulation with $F_n^{\text{n.f.},0} = 1.01 \times \mu_d w_n$; the initial shear force is slightly above the dynamic friction level. The two left plots are the shear force and rupture velocity as shown previously, while the right plot is the rupture velocity plotted against the inverse of the block number.

Figure 5.1: The rupture velocity is shown for two different initial shear force levels. The red line extending from the curve in the rightmost plots illustrates the extrapolation towards $N \to \infty$. Legends are the same as in Figure 4.12, and $\eta = 0$ for all four simulations. Other parameters are as in Table 4.1.

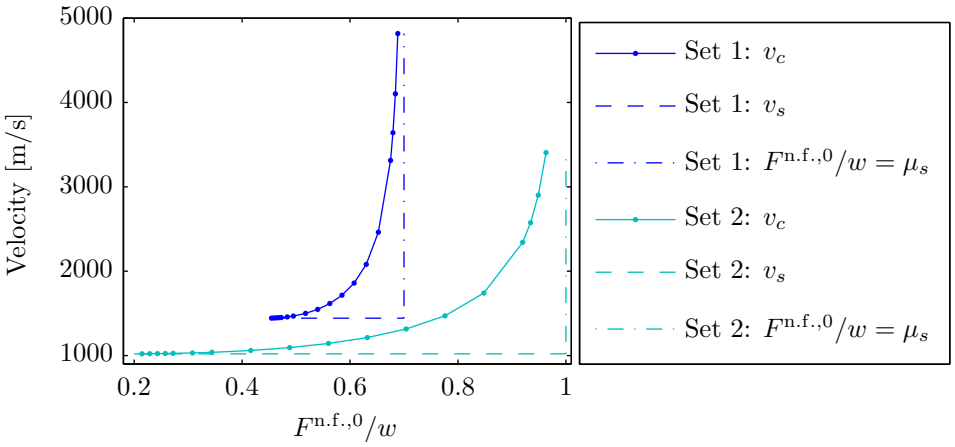

Figure 5.2: The final rupture velocity as a function of the initial shear stress for two different parameter sets. Set 1 has parameters as in Table 4.1, while set 2 has $\mu_s = 1$, $\mu_d = 0.2$ and $E = 1.25$ GPa, while the other parameters are as tabulated.

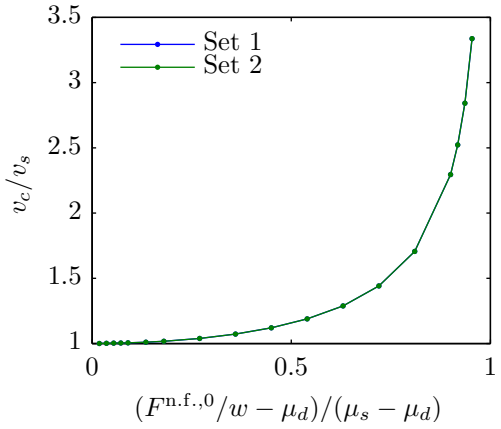

Figure 5.3: Data collapse of the two curves shown in Figure 5.2 using equation (5.1). The collapse works extremely well, suggesting that the assumed relationship is correct.

For a uniform initial shear force below the dynamic friction level, the rupture is seen to arrest, and no stable rupture velocity is found. It should be noted that the results given above are independent of both the driving spring constant K and the driving spring velocity V. These two parameters only seem to affect the transients, and not the final rupture velocities. In addition, the spatial extent of the transients seems to disappear as the number of blocks is increased. This means that, in the limit $N \to \infty$, the transients will disappear, and the constant rupture velocities will be reached instantly. There has not been time to do a quantitative analysis of the transients.

From the results above, there seems to be a relationship between the initial shear force and the rupture velocity. The collapse shown in Figure 5.3 even suggests the functional form of this relationship. In the next section, the scaling found above will be proven, and a scheme for finding the function $\bar{v}_c(\bar{\tau})$ analytically will be given.

5.1.2 Analytical calculation

In this section, the rupture velocities for uniform prestresses will be calculated from the equations of motion assuming a constant rupture velocity. Muratov [39] has previously

done this for the one-dimensional Burridge–Knopoff model using the approximations of soft driving springs and a slow driving velocity. It will be shown here that the side driven model results in the same equations determining the rupture velocities as the ones obtained by Muratov [39], but without any approximations being necessary.

Since the calculation will be done for uniform systems, meaning that the normal and initial shear forces do not vary along the interface, all indices indicating block number will be dropped for these forces. First, the equations that need to be solved are derived, and second, an iterative scheme is used to solve them.

Deriving the equations

The equation of motion is given by

$$m\ddot{u}(t) = k(u_{n+1}(t) + u_{n-1}(t) - 2u_n(t)) - \mu_d w, \tag{5.2}$$

for all moving blocks, ignoring edge effects. The initial positions are usually chosen according to equation (4.16) given an initial shear force.

The above equation can, however, be rewritten in such a way that all blocks are initially placed at the origin, but with an initial shear force still included. This is done by introducing the new variable $u'_n(t)$, which is a measure of the position of block n relative to its initial position, defined by

$$u'_n(t) = u_n(t) - u_n^0, \tag{5.3}$$

where u_n^0 is the initial position of block n calculated by equation (4.16). Inserting this into equation (5.2), leads to

$$\begin{aligned} m\ddot{u}'_n(t) &= k\left(u'_{n+1}(t) + u'_{n-1}(t) - 2u'_n(t)\right) + k\left(u^0_{n+1}(t) + u^0_{n-1}(t) - 2u^0_n(t)\right) - \mu_d w \\ m\ddot{u}'_n(t) &= k\left(u'_{n+1}(t) + u'_{n-1}(t) - 2u'_n(t)\right) + F^{\text{n.f.},0} - \mu_d w, \end{aligned} \tag{5.4}$$

where $F^{\text{n.f.},0}$ again is the initial shear force on all blocks.

The next step is to write equation (5.4) on a dimensionless form. This can be done by introducing a dimensionless time $\bar{t} = t/T$ and block position $\bar{u}_n = u'_n/U$. Inserting this into equation (5.4) yields

$$\frac{\mathrm{d}^2\bar{u}_n}{\mathrm{d}\bar{t}^2} = \frac{kT^2}{m}\left(\bar{u}_{n+1} + \bar{u}_{n-1} - 2\bar{u}_n\right) + \frac{T^2}{Um}\left(F^{\text{n.f.},0} - \mu_d w\right) \tag{5.5}$$

Choosing $T = \sqrt{m/k}$ then leads to

$$\frac{\mathrm{d}^2\bar{u}_n}{\mathrm{d}\bar{t}^2} = \bar{u}_{n+1} + \bar{u}_{n-1} - 2\bar{u}_n + \frac{1}{Uk}\left(F^{\text{n.f.},0}/w - \mu_d\right) w, \tag{5.6}$$

The maximum and minimum possible initial shear force will depend on the local static and dynamic friction, and U should therefore be chosen such that the dimensionless initial shear is always between e.g. 0 and 1, independent of the local static and dynamic friction levels. This can be done by choosing $U = (\mu_s - \mu_d)w/k$, which leads to the dimensionless equation of motion:

$$\frac{\mathrm{d}^2\bar{u}_n}{\mathrm{d}\bar{t}^2} = \bar{u}_{n+1} + \bar{u}_{n-1} - 2\bar{u}_n + \bar{\tau}, \tag{5.7}$$

where

$$\bar{t} = t/T, \quad \bar{u}_n = u_n'/U, \qquad T = \sqrt{\frac{m}{k}}, \quad U = \frac{(\mu_s - \mu_d)w}{k}, \quad \bar{\tau} = \frac{F^{\text{n.f.},0}/w - \mu_d}{\mu_s - \mu_d}. \tag{5.8}$$

Transformations of the time and block position have now been made. A transformation of the spatial coordinate x can also be made. The velocity of sound will depend on Young's modulus E and the density ρ, and having a dimensionless sound velocity equal to 1 would be convenient. The velocity of sound is given by [32]

$$v_s = a\sqrt{\frac{k}{m}}, \tag{5.9}$$

where a is the equilibrium distance between to blocks, $a = L_x/(N-1)$. A dimensionless position coordinate is now introduced, $\bar{x} = x/x_0$. The dimensionless velocity is then given by

$$\bar{v}_s = a\sqrt{\frac{k}{m}}\frac{T}{x_0} = \frac{a}{x_0},$$

and choosing $x_0 = a$ then leads to $\bar{v}_s = 1$, as desired.

The initial shear force $\bar{\tau}$ can be removed from equation (5.7) by doing another transformation. Introducing the new variable $\tilde{u}_n$ defined by

$$\bar{u}_n = \bar{\tau}\left(\tilde{u}_n + \frac{\bar{t}^2}{2}\right), \tag{5.10}$$

and inserting this into equation (5.7) above, leads to

$$\frac{\mathrm{d}^2\tilde{u}_n}{\mathrm{d}\bar{t}^2} = \tilde{u}_{n+1} + \tilde{u}_{n-1} - 2\tilde{u}_n, \tag{5.11}$$

where the initial shear force $\bar{\tau}$ has been removed by the transformation. If the rupture has reached block j at time $\bar{t}_j$, meaning that block j starts to move at the time $\bar{t}_j$, the equation of motion for this block in the interval $\bar{t} \in [\bar{t}_j, \bar{t}_{j+1}]$ is given by

$$\frac{\mathrm{d}^2\tilde{u}_j}{\mathrm{d}\bar{t}^2} = \tilde{u}_{j-1} - 2\tilde{u}_j - \frac{\bar{t}^2}{2}. \tag{5.12}$$

To obtain this equation, $\bar{u}_{j+1} = 0$ was inserted into equation (5.10) to obtain $\tilde{u}_{j+1}$, since in this interval block $j+1$ has not yet started to move.

The above differential equations are invariant to translations in time, meaning that $\bar{t} = 0$ can be chosen to be when block j starts to move, $\bar{t}_j = 0$. At this instant

$$\bar{u}_j(0) = 0, \qquad \left.\frac{\mathrm{d}\bar{u}_j}{\mathrm{d}\bar{t}}\right|_{\bar{t}=0} = 0,$$

which is the initial condition for block j. In the new variables, this is given by

$$\tilde{u}_j(0) = 0, \qquad \left.\frac{\mathrm{d}\tilde{u}_j}{\mathrm{d}\bar{t}}\right|_{\bar{t}=0} = 0 \tag{5.13}$$

using equation (5.10).

If the rupture is propagating at a constant velocity v_c, then

$$u'_{n-1}(t_j) = u'_n(t_j + \delta t), \qquad \dot{u}'_{n-1}(t_j) = \dot{u}'_n(t_j + \delta t),$$

where δt is the time between the triggering of two neighbouring blocks. Given a constant rupture velocity, the slip $u'_n(t)$ should be equal for all blocks, but delayed δt in time per block away from the block at the edge of the rupture, which leads to the relations above. In the new variables, this condition becomes

$$\tilde{u}_{n-1}(0) = \tilde{u}_n(\delta\bar{t}) + \frac{\delta\bar{t}^2}{2}, \qquad \left.\frac{\mathrm{d}\tilde{u}_{n-1}}{\mathrm{d}\bar{t}}\right|_{\bar{t}=0} = \left.\frac{\mathrm{d}\tilde{u}_n}{\mathrm{d}\bar{t}}\right|_{\bar{t}=\delta\bar{t}} + \delta\bar{t}.$$

The time $\delta\bar{t}$ can be expressed in terms of the rupture velocity:

$$\bar{v}_c = \frac{\bar{a}}{\delta\bar{t}} = \frac{1}{\delta\bar{t}} \quad \Rightarrow \quad \delta\bar{t} = \frac{1}{\bar{v}_c} = \bar{v}_c^{-1},$$

which leads to

$$\tilde{u}_{n-1}(0) = \tilde{u}_n(\bar{v}_c^{-1}) + \frac{1}{2\bar{v}_c^2}, \qquad \left.\frac{\mathrm{d}\tilde{u}_{n-1}}{\mathrm{d}\bar{t}}\right|_{\bar{t}=0} = \left.\frac{\mathrm{d}\tilde{u}_n}{\mathrm{d}\bar{t}}\right|_{\bar{t}=\bar{v}_c^{-1}} + \frac{1}{\bar{v}_c}. \tag{5.14}$$

Assuming a rupture velocity $\bar{v}_c$, this set of equations can now be solved. The solution above must be related to the initial shear force, and this relation is determined by the rupture criterion

$$k(u_{j+1}(t_j) + u_{j-1}(t_j) - 2u_j(t_j)) = \mu_s w,$$

which means that at the time t_j, the shear force on block j is equal to the static friction level. In the new variables, this criterion is given by

$$\tilde{u}_{j-1}(0) = \frac{1-\bar{\tau}}{\bar{\tau}},$$

relating the obtained solution for a given rupture velocity to the initial shear force corresponding to this velocity.

In order to make the process of solving these equations simpler, a transformation of the indices is made $j - n \to n$. This means that block j's new index is 0, block $j-1$'s new index is 1 and so on. The set of equations that needs to be solved is then

$$\frac{\mathrm{d}^2\tilde{u}_0}{\mathrm{d}\bar{t}^2} = \tilde{u}_1 - 2\tilde{u}_0 - \frac{\bar{t}^2}{2}, \tag{5.15}$$

$$\frac{\mathrm{d}^2\tilde{u}_n}{\mathrm{d}\bar{t}^2} = \tilde{u}_{n+1} + \tilde{u}_{n-1} - 2\tilde{u}_n, \quad n \geq 1, \tag{5.16}$$

with the initial conditions given by

$$\tilde{u}_0(0) = 0, \qquad \left.\frac{\mathrm{d}\tilde{u}_0}{\mathrm{d}\bar{t}}\right|_{\bar{t}=0} = 0, \tag{5.17}$$

$$\tilde{u}_{n+1}(0) = \tilde{u}_n(\bar{v}_c^{-1}) + \frac{1}{2\bar{v}_c^2}, \quad \left.\frac{\mathrm{d}\tilde{u}_{n+1}}{\mathrm{d}\bar{t}}\right|_{\bar{t}=0} = \left.\frac{\mathrm{d}\tilde{u}_n}{\mathrm{d}\bar{t}}\right|_{\bar{t}=\bar{v}_c^{-1}} + \frac{1}{\bar{v}_c}, \tag{5.18}$$

and the corresponding initial shear force is given by

$$\tilde{u}_1(0) = \frac{1-\bar{\tau}}{\bar{\tau}}. \tag{5.19}$$

The scaling of the rupture velocities suggested in equation (5.1) is now already proved. Equations (5.15) to (5.18) have a unique solution for a given $\bar{v}_c$. The solution will be on the form $\tilde{u}_n = \tilde{u}_n(\bar{t}, \bar{v}_c)$, and using equation (5.19) then yields $\bar{v}_c = \bar{v}_c(\bar{\tau})$.

Equations (5.15) to (5.19) is in fact the exact same equations obtained by Muratov [39] for the Burridge–Knopoff model. However, no assumptions have been made regarding the driving, meaning that the equations above are the exact equations for the constant rupture velocities in the side driven model.

Solving the equations

The next step is to solve equations (5.15) to (5.18). In a numerical scheme, this can be done as follows:

1. Use equation (5.17) for the initial condition for block 0 and guess the initial condition for the other blocks.
2. Solve equations (5.15) and (5.16) using these initial conditions from $\bar{t} = 0$ to $\bar{t} = 1/\bar{v}_c$ using e.g. the Runge-Kutta method.
3. Use equation (5.18) to obtain a new guess for the initial conditions for blocks 1 to N.
4. Repeat 2. and 3. until the solution $\tilde{u}_n(\bar{t}, \bar{v}_c)$ has converged.
5. The function $\bar{v}_c(\bar{\tau})$ can be found by repeating 1. to 4. for several different values of $\bar{v}_c$ and using equation (5.19) to obtain the corresponding initial shear force.

This method will not be employed here, since a numerical result for the function $\bar{v}_c(\bar{\tau})$ already has been found, given in Figure 5.3.

Equations (5.15) to (5.18) can also be solved analytically by expanding the solution in powers of $\bar{v}_c^{-1}$. If the rupture velocity is large, $\bar{v}_c \gg 1$, then block 0 only has to move a very small distance in order to initiate its neighbour's movement. Therefore, in the interval $0 \leq \bar{t} \leq \delta\bar{t} = \bar{v}_c^{-1}$, block 0 can be approximated to be stationary in the limit $\bar{v}_c^{-1} \to 0$. When the rupture velocity is infinitely high, interactions between the blocks will become less prominent because the time interval $\delta\bar{t}$ becomes negligibly small.

Using this, therefore neglecting the right-hand sides of equations (5.15) and (5.16), integrating both equations with respect to $\bar{t}$ twice, and applying the initial conditions in equations (5.17) and (5.18), a zeroth order approximation to the solution of equations (5.15) to (5.18) can be found. The result is

$$\tilde{u}_n^{(0)}(\bar{t}, \bar{v}_c) = \frac{n^2}{2\bar{v}_c^2} + \frac{n\bar{t}}{\bar{v}_c}, \tag{5.20}$$

which corresponds to the solution in the limit $\bar{v}_c \to \infty$, and

$$\tilde{u}_1^{(0)}(0, \bar{v}_c) = \frac{1}{2\bar{v}_c^2}. \tag{5.21}$$

The result for $\tilde{u}_n^{(0)}(\bar{t}, \bar{v}_c)$ can now be used to obtain the solution to the first order. By inserting $u_n^{(0)}$ on the right hand side of equations (5.15) and (5.16), integrating,

and applying the initial conditions given in equations (5.17) and (5.18), the first order solution can be found. It is given by

$$\begin{aligned}\tilde{u}_0^{(1)}(\bar{t},\bar{v}_c) &= -\frac{\bar{t}^4}{24}+\frac{\bar{t}^3}{6v_c}+\frac{\bar{t}^2}{4v_c^2},\\ \tilde{u}_n^{(1)}(\bar{t},\bar{v}_c) &= \frac{1}{24\bar{v}_c^4}-\frac{n}{6\bar{v}_c^4}+\frac{n^2}{2\bar{v}_c^4}-\frac{\bar{t}}{6\bar{v}_c^3}+\frac{n\bar{t}}{\bar{v}_c^3}+\frac{\bar{t}^2}{2\bar{v}_c^2}+\frac{n^2}{2\bar{v}_c^2}+\frac{n\bar{t}}{\bar{v}_c},\quad n\geq 1,\end{aligned} \tag{5.22}$$

which results in

$$\tilde{u}_1^{(1)}(0,\bar{v}_c)=\frac{1}{2\bar{v}_c^2}+\frac{3}{8v_c^4}. \tag{5.23}$$

This procedure has been followed to the third order in Mathematica, resulting in

$$\begin{aligned}\tilde{u}_0^{(3)}(\bar{t},\bar{v}_c) = \frac{\bar{t}^2}{40320\bar{v}_c^6}\Big[&6300+4872\bar{v}_c\bar{t}+70\bar{v}_c^2\left(108+5\bar{t}^2\right)-\\ &56\bar{v}_c^3\bar{t}\left(-100+9\bar{t}^2\right)-28\bar{v}_c^4\left(-360+\bar{t}^4\right)+8\bar{v}_c^5\bar{t}\left(840-84\bar{t}^2+5\bar{t}^4\right)+\\ &\bar{v}_c^6\left(-1680\bar{t}^2+112\bar{t}^4-5\bar{t}^6\right)\Big],\end{aligned} \tag{5.24}$$

and

$$\tilde{u}_1^{(3)}(0,\bar{v}_c)=\frac{1}{2\bar{v}_c^2}+\frac{3}{8v_c^4}+\frac{5}{16v_c^6}+\frac{35}{128\bar{v}_c^8}. \tag{5.25}$$

The series given in equation (5.25) is actually the first four terms in the Taylor expansion of the function

$$\begin{aligned}\frac{1}{\sqrt{1-x}}-1 &= \sum_{n=1}^{\infty}\binom{-1/2}{n}(-1)^{n+1}x^n\\ &= \frac{x}{2}+\frac{3x^2}{8}+\frac{5x^3}{16}+\frac{35x^4}{128}+\frac{63x^5}{256}+\cdots\end{aligned} \tag{5.26}$$

about the point $x=0$, where

$$\binom{x}{y}=\frac{\Gamma(x+1)}{\Gamma(y+1)\Gamma(x-y+1)} \tag{5.27}$$

is the generalised binomial coefficient. It has not yet been proved that $\tilde{u}_1(0,\bar{v}_c)$ is the function given in equation (5.26) (to infinite order), but it will be shown later that it fits extremely well with the numerical results. One strategy of proving this relation would be to recognise the series development of $u_0(\bar{t},\bar{v}_c)$, and then proving that this is indeed the solution by inserting it into equations (5.15) to (5.18). However, it is a series in both $\bar{t}$ and $\bar{v}_c^{-1}$, and attempts have not yet been successful. In the rest of this thesis, it will be assumed that this is indeed the correct solution. If it is not, then it can be thought of as a fit to the numerical result that is more than good enough for the uses to which it will be put.

Anyway, using equation (5.26) results in the relation

$$\tilde{u}_1(0,\bar{v}_c)=\frac{1}{\sqrt{1-1/\bar{v}_c^2}}-1, \tag{5.28}$$

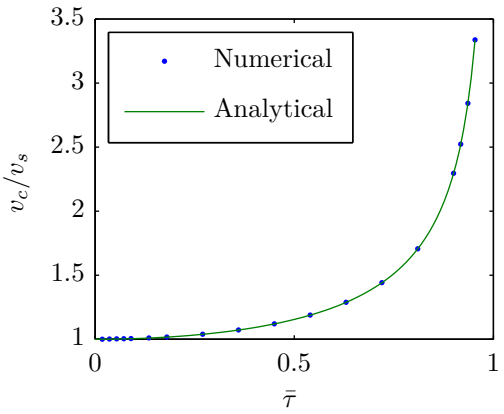

Figure 5.4: The numerical result presented in section 5.1.1 plotted with the analytical solution given in equation (5.29).

which, using equation (5.19) yields the relation between the initial shear force and the rupture velocity:

$$\boxed{\bar{v}_c(\bar{\tau}) = \frac{1}{\sqrt{1-\bar{\tau}^2}}.} \tag{5.29}$$

As expected, the solution approaches 1 in the limit $\tau \to 0$, and infinity in the limit $\tau \to 1$. It is also flat at $\bar{\tau} = 0$, as suggested by the numerically result. In Figure 5.4, the function $\bar{v}_c(\bar{\tau})$ given in equation (5.29) is plotted with the numerical result obtained in section 5.1.1. The analytical solution fits the numerical result extremely well, and equation (5.29) will therefore be used instead of the numerical solution in the rest of this thesis.

5.2 Non-uniform prestress

Up until now, the initial shear force level, the friction coefficients and the normal force have been constant along the interface. This was shown to lead to a constant rupture velocity after a transient. In this section, the effects of a non-uniform prestress will studied. It is then interesting to observe whether the velocities still lie on the curve seen in Figure 5.4, making the result obtained above more general, or not.

First, the effect of a sudden change in the initial state of the interface will be investigated. Then, the consequence of continuously changing properties along the interface will be discussed.

5.2.1 Discrete jumps in the initial state of the interface

In this section, the effect of a sudden change from one uniform initial state of the interface to another is studied. According to the analytical calculation done above, there exists for a given uniform initial state one unique constant velocity at which the rupture can propagate for a given initial state. It is then interesting to investigate if this velocity is realised when the interface suddenly changes from one state to another.

The result from simulations done, where the initial shear force and the friction coefficients are varied systematically, are shown in Figures 5.5 to 5.7. In Figure 5.5, the result is shown for a sudden increase in the initial shear force, corresponding to a highly prestressed region. It is clear from the figure that, after transients seen as vertical sets of points in the rightmost plot, constant rupture velocities are achieved which equal the ones given by equation (5.29).

This is equally true for both a sudden change in the dynamic friction coefficient, seen in Figure 5.6, and a sudden change in the static friction coefficient, seen in Figure 5.7. This means that, even though changes in the initial state of the interface occur, the constant rupture velocity corresponding to a given $\bar{\tau}$ will be realised. Again, the spatial extent of the transients is seen to become smaller as N is increased, leading to an instant change in rupture velocity for an instant change in the initial state of the interface.

Of course, instantaneous changes along the interface are not physical. In reality, the interface will have a more or less continuous variation of both strength and initial shear stress. Up until now, only constant initial states of the interface have been studied. It is therefore natural to investigate the effect of continuously varying the friction coefficients and the initial shear force along the interface. That is the purpose of the next section.

5.2.2 Continuous variations in the initial state of the interface

Several different simulations have been done with different continuous changes in the initial state of the interface. As examples of such results, consider Figures 5.8 and 5.9. These two figures show the result for the exact same initial state of the interface, but in Figure 5.8, $N = 100$, while in Figure 5.9, $N = 1000$. In both, the friction coefficients are constant along the interface, while the initial shear force is varying as a cosine function.

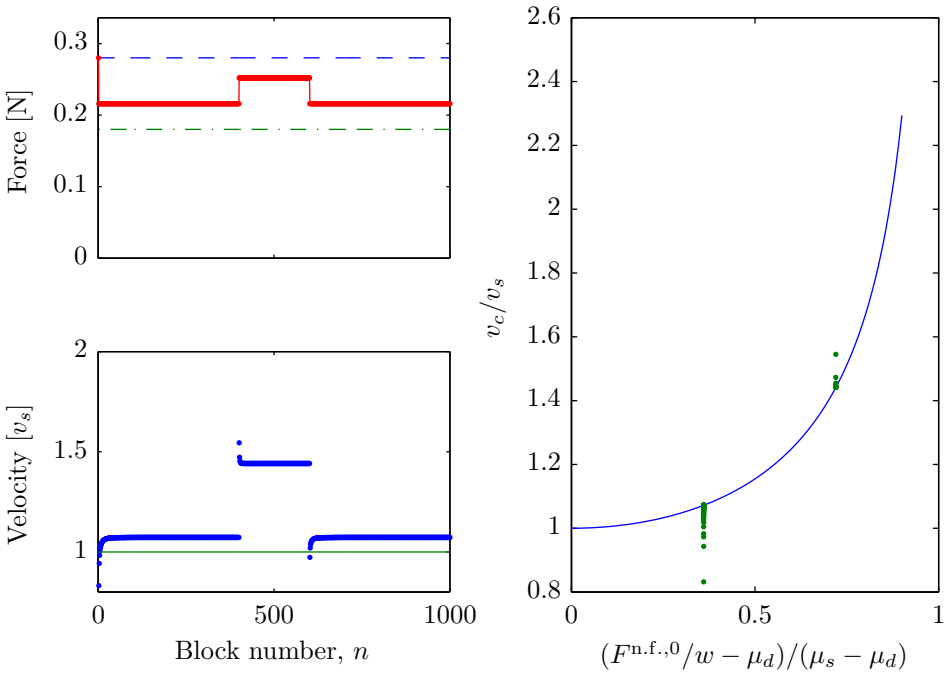

Figure 5.5: The top left plot shows, as usual, the initial state of the interface with an increase in the shear force in the middle. The bottom left plot shows the corresponding rupture velocities. The right plot shows the rupture velocities plotted as function of $\bar{\tau}$ as points, where the drawn line is the analytical calculated function $\bar{v}_c(\bar{\tau})$.

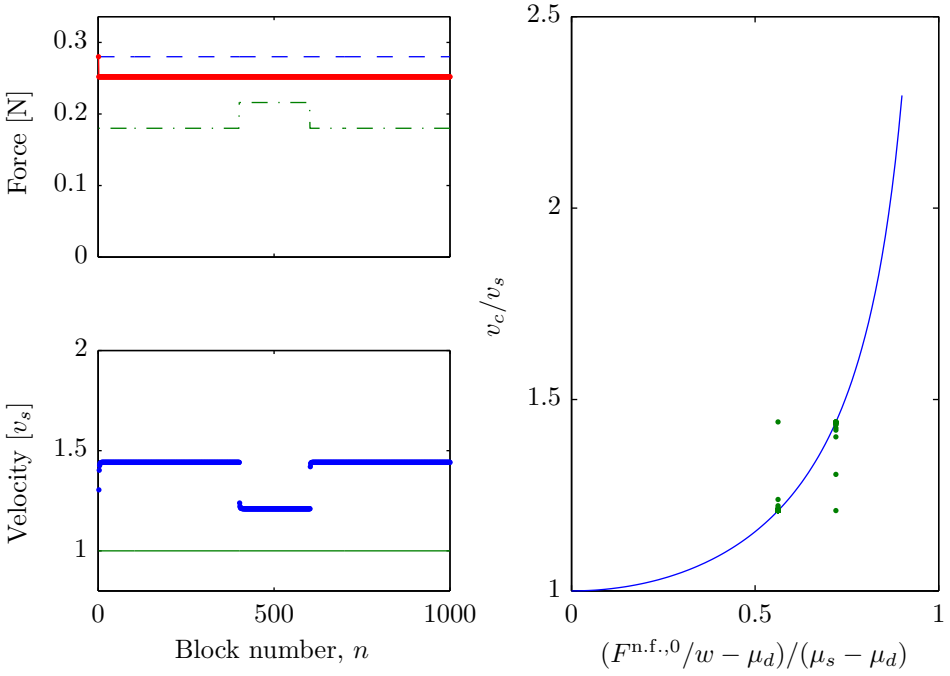

Figure 5.6: The top left plot shows the initial state of the interface with an increase in the dynamic friction coefficient in the middle. The bottom left plot shows the corresponding rupture velocities. The right plot shows the rupture velocities plotted as function of $\bar{\tau}$ as points, where the drawn line is the analytical calculated function $\bar{v}_c(\bar{\tau})$.

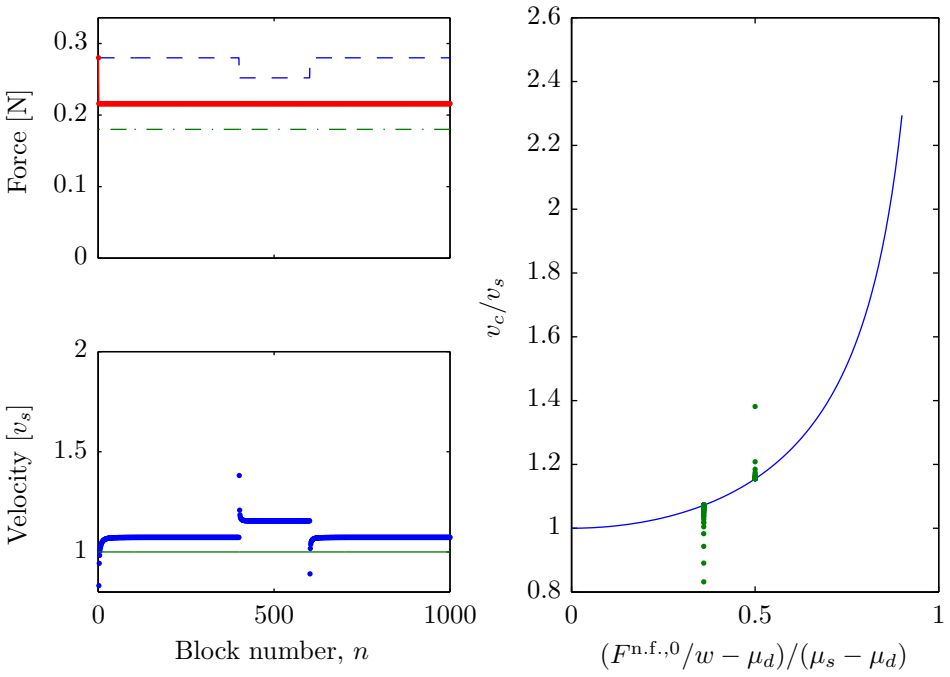

Figure 5.7: The top left plot shows the initial state of the interface with a decrease in the static friction level in the middle. The bottom left plot shows the corresponding rupture velocities. The right plot shows the rupture velocities plotted as function of $\bar{\tau}$ as points, where the drawn line is the analytical calculated function $\bar{v}_c(\bar{\tau})$.

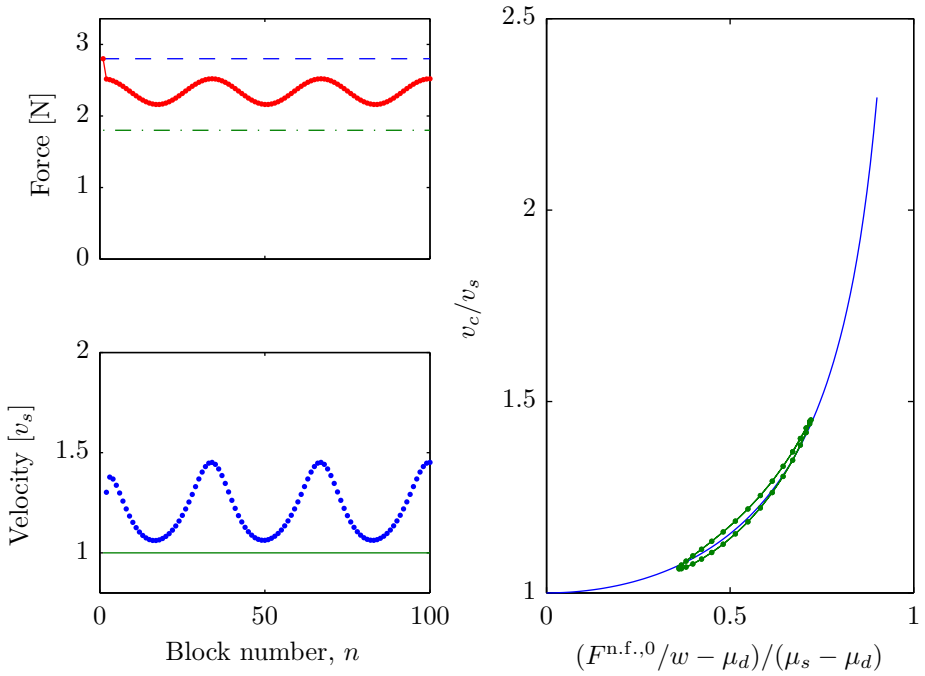

Figure 5.8: The topmost left plot shows the initial state of the interface with a continuously varying initial shear force. The lowermost left plot shows the corresponding rupture velocities. The right plot shows the rupture velocities plotted as function of $\bar{\tau}$ as points, where the drawn line is the analytical calculated function $\bar{v}_c(\bar{\tau})$. In this simulation, $N = 10$.

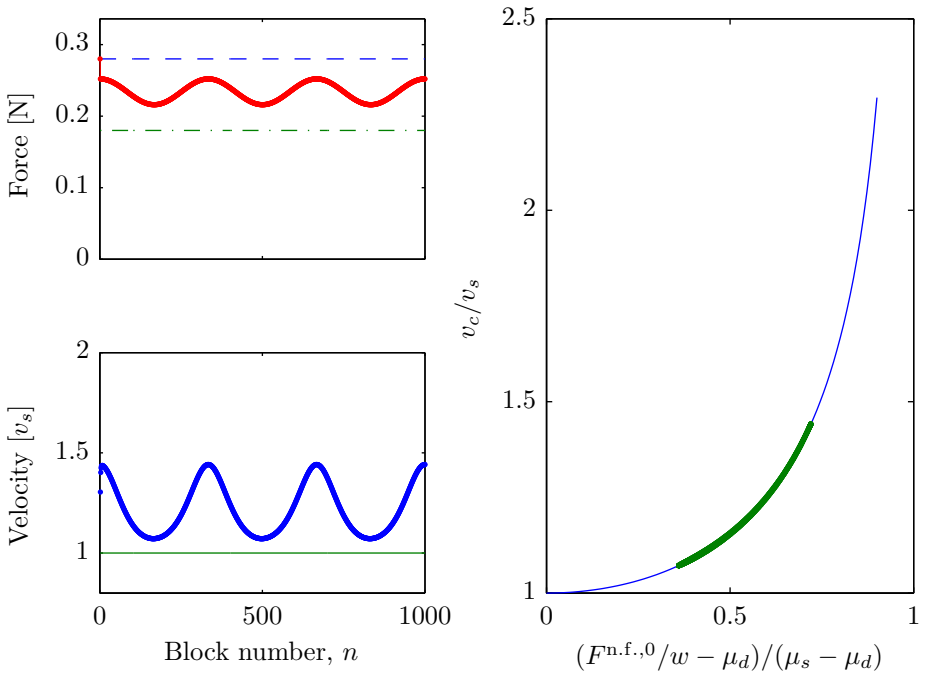

Figure 5.9: The topmost left plot shows the initial state of the interface with a continuously varying initial shear force. The lowermost left plot shows the corresponding rupture velocities. The right plot shows the rupture velocities plotted as function of $\bar{\tau}$ as points, where the drawn line is the analytical calculated function $\bar{v}_c(\bar{\tau})$. In this simulation, $N = 1000$.

The relationship between the initial shear force and the rupture velocity is again obvious, but the most interesting feature can be seen in the rightmost plots in the two figures. For the simulation with $N = 100$, the deviation between the resulting velocities and the analytical calculated curve for constant rupture velocities is not difficult to notice. This difference, however, seems to have been significantly reduced for the simulation with $N = 1000$.

This shows that, in the limit $N \to \infty$, all velocities will be on the analytically calculated curve $\bar{v}_c(\bar{\tau})$. This is in agreement with the observation made in the previous section that transients become less prominent as the number of blocks is increased. The function $\bar{v}_c(\bar{\tau})$ is then a much stronger result than initially expected. It is this curve that dominates the rupture velocities both in uniform systems and in non-uniform systems.

As mentioned above, fronts are seen to arrest if $\bar{\tau} < 0$. Fronts do not, however, arrest instantaneously, but the way in which such a front arrests has not been studied in detail. Simulations indicate that that the behaviour becomes much more complex and that it depends on the number of blocks. There has unfortunately not been time to pursue this further.

5.3 Special case: all blocks at the dynamic friction level

Up until now, initial shear forces exactly at the dynamic friction level have been consistently avoided. There is a good reason for this, because this level of the initial shear force appears to be extremely special. It should be noted that the above analytical calculation breaks down when $\bar{\tau} = 0$ because of the transformation done in equation (5.10). This special case will therefore be treated separately in this section.

5.3.1 Numerical results

Four different scenarios for the initial state of the interface are given in Figure 5.10. Common to all of them is that the initial shear force is equal to the dynamic friction level except for the small jump in the initial shear force in Figure 5.10d.

Starting out with Figure 5.10a, one can see that the velocity is not equal to the sound velocity, as predicted by equation (5.29), but rather a great deal lower. By comparing Figures 5.10a and 5.10b, it is clear that the rupture velocity is independent of the friction coefficients. This is the same situation as predicted by $\bar{v}_c(\bar{\tau})$, since $\bar{\tau} = 0$ for both cases.

In Figure 5.10c, $\bar{\tau} = 0$ along the whole interface as well. However, when the static coefficient of friction is reduced, the rupture velocity is increased. It is clear from the figure that this is not a transient effect, the rupture velocity is stabilising at a higher level. This means that two (or possibly more) different constant rupture velocities results from the same value of $\bar{\tau}$ instead of just one as was the case for $\bar{\tau} > 0$. In addition, neither of these two velocities are in quantitative agreement with equation (5.29).

Figure 5.10d shows an even stranger situation. In the left part of the sample, where nothing has changed, the rupture velocity is the same as in Figure 5.10a. Then, by increasing the shear force, the rupture velocity is increased, as expected. By measuring this velocity, and comparing it with the result from equation (5.29) inserted for the local value of $\bar{\tau}$, one can observe that this rupture velocity is in agreement with the mentioned equation.

When the front has passed this highly prestressed region, the rupture velocity is reduced. It does not, however, return back to the velocity it had before the highly prestressed region, but appears to stabilise at a higher velocity approaching the velocity of sound. Again, more than one constant rupture velocity is seen to exist for $\bar{\tau} = 0$.

It turns out that $\bar{\tau} = 0$ is even more peculiar than this. By doing a simple calculation, an even lower stable rupture velocity than the one seen in Figure 5.10a can be found. This calculation is given below, with the result from a numerical simulation to support it.

5.3.2 Analytical calculation

Consider a system where all blocks are at the dynamic friction level initially, and a rupture propagating in the positive x direction. By assuming that this rupture propagates with only one block moving at a time, the rupture velocity can be found rather straight forward by considering the motion of a single block. A block, say block n, can then be

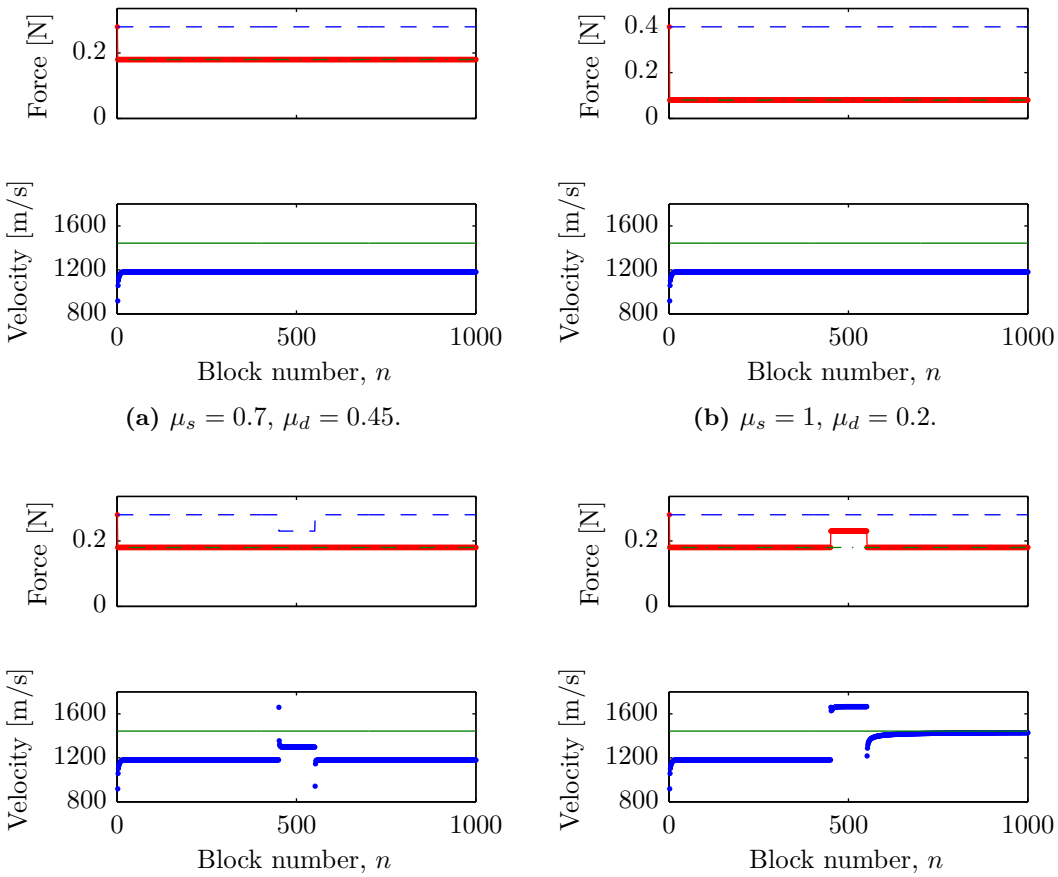

(a) $\mu_s = 0.7$, $\mu_d = 0.45$.

(b) $\mu_s = 1$, $\mu_d = 0.2$.

(c) $\mu_s = 0.7$, $\mu_d = 0.45$. Reduced μ_s in the middle.

(d) $\mu_s = 0.7$, $\mu_d = 0.45$. Increased initial shear force in the middle.

Figure 5.10: Different simulation results obtained for the initial shear force at the dynamic friction level.

considered to be attached to two walls, and the equation of motion needs to be solved from the time it is put into motion by its left neighbour, to the time where this motion has caused its right neighbour to reach the static friction level. For this type of rupture to exist, this time then has to coincide with the time the block itself stops.

Let block n start moving at the time $t = 0$, with $u_n(t)$ the position of block n as a function of time, and $u_n(t = 0) = 0$. u_{n-1} and u_{n+1} are then the position of block $n-1$ and $n+1$, which are assumed constant in the time span considered here, as stated above. The total spring force from blocks $n-1$ and $n+1$ on block n is given by

$$F_n^{\text{n.f.}}(t) = k_l(u_{n-1} - u_n(t)) + k_r(u_{n+1} - u_n(t)), \tag{5.30}$$

where the first term is the spring force from block $n-1$ on block n (spring constant k_l), and the second term is the spring force from block $n+1$ on block n (spring constant k_r). At $t = 0$ this force is then given by

$$F_n^{\text{n.f.}}(0) = k_l u_{n-1} + k_r u_{n+1}.$$

Inserting this into equation (5.30) leads to the formula for the total spring force on block

n for a given initial force $F_n^{\text{n.f.}}(0)$,

$$F_n^{\text{n.f.}}(t) = F_n^{\text{n.f.}}(0) - (k_l + k_r)u_n(t). \tag{5.31}$$

From Newton's second law, the equation of motion for this system is

$$m\ddot{u}_n(t) + (k_l + k_r)u_n(t) = F_n^{\text{n.f.}}(0) - \mu_d w_n, \tag{5.32}$$

where the mass of one block is as usual m, μ_d is the dynamic friction coefficient and w_n is the normal force on block n. This is a linear inhomogeneous ordinary differential equation, and the solution is given by

$$u_n(t) = B\sin(\omega t) + C\cos(\omega t) + \frac{F_n^{\text{n.f.}}(0) - \mu_d w_n}{k_l + k_r}, \qquad \omega = \sqrt{\frac{k_l + k_r}{m}}, \tag{5.33}$$

where B and C are constants determined by the initial conditions $u_n(0) = \dot{u}_n(0) = 0$. Applying these initial conditions to equation (5.33) results in

$$u_n(t) = -C\cos(\omega t) + C, \qquad C = \frac{F_n^{\text{n.f.}}(0) - \mu_d w_n}{k_l + k_r}. \tag{5.34}$$

Because of the motion of block n, block $n+1$ will experience an increased spring force from block n, and this increase equals $k_r u_n(t)$. Block $n+1$ will then reach the static friction level and start to move at the time t_{n+1} when

$$k_r u_n(t_{n+1}) = \mu_s w_{n+1} - F_{n+1}^{\text{n.f.}}(0),$$

where $F_{n+1}^{\text{n.f.}}(0)$ is the preload on block $n+1$. Inserting for $u_n(t)$ by using equation (5.34) leads to the equation

$$-\frac{F_n^{\text{n.f.}}(0) - \mu_d w_n}{k_l + k_r}\cos(\omega t_{n+1}) + \frac{F_n^{\text{n.f.}}(0) - \mu_d w_n}{k_l + k_r} = \frac{\mu_s w_{n+1} - F_{n+1}^{\text{n.f.}}(0)}{k_r} \tag{5.35}$$

Solving this equation for t_n will involve an arccos function, and will not necessarily be self consistent in the sense that the velocity of block n will be zero at t_{n+1}. By now inserting $F_n^{\text{n.f.}}(0) = \mu_s w_n$, $F_{n+1}^{\text{n.f.}}(0) = \mu_d w_{n+1}$ and $w_n = w_{n+1} = w$ into equation (5.35), the time t_{n+1} is given by

$$-\frac{\mu_s w - \mu_d w}{k_l + k_r}\cos(\omega t_{n+1}) + \frac{\mu_s w - \mu_d w}{k_l + k_r} = \frac{\mu_s w - \mu_d w}{k_r}.$$

It is now interesting to note that the numerators cancel, consequently that the friction coefficients and the normal force do as well. The case $\mu_s = \mu_d$ is ruled out because it would lead to an infinite rupture velocity. The above equation then yields

$$\cos(\omega t_{n+1}) = -\frac{k_l}{k_r}, \tag{5.36}$$

and for $k_l = k_r$, the solution for the smallest $t_{n+1} > 0$ is then given by

$$t_{n+1} = \frac{\pi}{\omega}. \tag{5.37}$$

It is now necessary to check if $\dot{u}_n(t_{n+1}) = 0$. Using equation (5.34), it is clear that this is the case, because $\sin(\omega t_{n+1}) = \sin(\pi) = 0$.

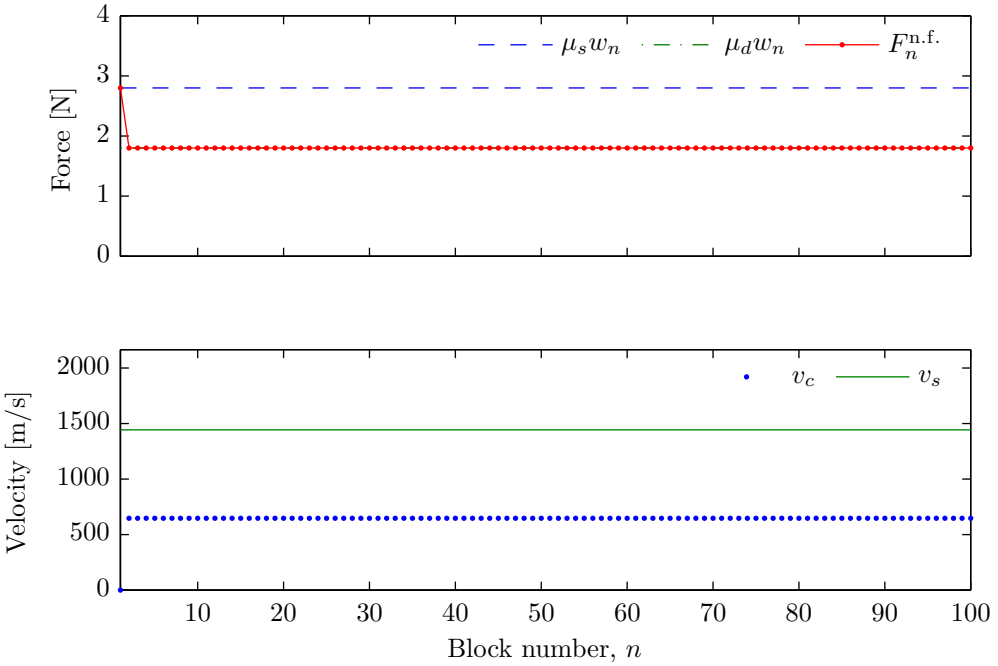

Figure 5.11: The rupture velocity from a simulation with $K = k$ and $V = 1 \times 10^{-8}$ m/s. As shown, the rupture velocity is constant, with no transient. Measured rupture velocity equals approximately 647 m/s, which is very close to the analytically obtained 641 m/s from equation (5.38). The reason for this slight deviation is the non-zero driving velocity and numerical errors.

The rupture velocity v_c is then given by the distance between block n and $n+1$ divided by the time t_{n+1} since block n started to move at $t = 0$. Using equations (4.10), (5.33) and (5.37), this leads to the rupture velocity

$$v_c = \frac{L/(N-1)}{t_{n+1}} = \pi\sqrt{\frac{2EAL}{M}}, \qquad N \gg 1. \tag{5.38}$$

Inserting for the usual parameters given in Table 4.1, the rupture velocity is $v_c \approx 641$ m/s or $\bar{v}_c \approx 0.44$.

This is then a completely different rupture velocity than what is seen in the numerical simulations in Figure 5.10 and the one predicted by the formula $\bar{v}_c(\bar{\tau})$. However, this rupture velocity can also be obtained through numerical simulations by using $K = k$ and a very small driving velocity. This will then cause the driving point to be approximately stationary while the first block is moving, and the motion of this block is then given by equation (5.34). According to the calculation above, the first block will then stop at the time t_2, initiating the movement of the second block. The numerical result can be seen in Figure 5.11, where the driving spring constant K is equal to the material spring constant k. The velocity obtained is indeed the one predicted by equation (5.38).

The rupture velocity for the special case $F^{\text{n.f.},0} = \mu_d w$ is then highly dependent on both the driving velocity V and the driving spring constant K, which is not the case for all other initial shear levels. The result seen in Figure 5.10 then corresponds to the soft

driving limit, where $K \ll k$, and the driving force is approximately constant during rupture.

Summing up, there is no unique constant rupture velocity that corresponds to the initial shear force at the dynamic friction level, $\bar{\tau} = 0$. Rather, the resulting rupture velocity is highly dependent on the chosen driving spring constant K, the driving velocity V, and the history of the rupture, as seen in Figure 5.10.

5.4 Summary and conclusion

In this chapter it has been shown that for $\bar{\tau} > 0$, there exists a unique constant rupture velocity $\bar{v}_c = \bar{v}_c(\bar{\tau})$. This was done in a way similar to that in [39] for the Burridge–Knopoff model, but for the side driven model, no approximations were necessary. It has also been shown that for $\tau = 0$, several different constant rupture velocities exist, and that the one realised depends on the driving spring constant, the driving velocity, and the history of the rupture. It does not, however, exceed v_s, which is the predicted velocity from equation (5.29).

Unfortunately, this does not ease the interpretation of the original simulation result given in Figure 4.12 much. The reason for this is that the initial shear force is slightly below the dynamic friction level, causing a decrease in the rupture velocity until a highly prestressed region is reached. The velocity is then increased abruptly, followed by a new decrease. This means that the rupture velocity in Figure 4.12 is dominated by transients, which unfortunately depend on the model resolution N, and the special case $\bar{\tau} = 0$. There has unfortunately not been enough time to investigate the transients further. This in addition to a study of the situation $\bar{\tau} < 0$ are something that should be done in order to get a complete understanding of the rupture velocities in the side driven model.

The top driven model has not been studied in this chapter. These results can therefore not be applied directly to understand the result in Figure 4.27a. However, the equations determining the (constant) rupture velocities in the side driven model was found by Muratov [39] to be valid in the Burridge–Knopoff model as well. Though he only considered uniform initial states of the interface and constant rupture velocities, it is expected that the extension to non-uniform initial states will be similar as that for the side driven model. This is further indicated by the fact that the shape of the function $\bar{v}_c(\bar{\tau})$ is recognisable from Figure 4.27a. The large deviations from the master curve $\bar{v}_c(\bar{\tau})$ may explained by transients.

From experiments, there seems to be a close relationship between the initial local stress ratio and the local rupture velocity, as discussed previously. In the model, there is a specific relationship between the rupture velocity and the initial stress, given by $\bar{v}_c(\bar{\tau})$, where $\bar{\tau}$ serves as a generalisation of the suggested scaling τ/σ in the experiments. This then serves as further indication that the local stress ratio is indeed very important. It also suggests that the strength of the frictional interface, which in the model is represented by μ_s and μ_d, plays an important role. The strength of the interface will vary in the experiments, which could then explain the large spread in the rupture velocities in Figure 3.4b. The scaling derived here has been shown to work in a $(1 + 1)$D model as well with the same friction law [56], suggesting that this scaling is even more general

than what the one-dimensional results given here might indicate.

There are, however, expected deviations between these model results and the experimental results. Firstly, for all $\bar{\tau} > 0$, the rupture velocity is greater than the speed of sound. It actually goes to infinity as $\bar{\tau} \to 1$. In experiments, v_c is seen to exceed the shear wave speed c_S, but it do not exceed the longitudinal wave speed c_L. In the one-dimensional model, only longitudinal waves exist, and their velocity v_s is smaller than the longitudinal wave speed in a three-dimensional medium c_L. For $\bar{\tau} > 0$, the rupture velocity in the model is seen to be super-longitudinal. Secondly, slow ruptures are not observed. Thirdly, the large variation in the stress ratio seen in experiments (from 0.3 to 2, see Figure 3.4b) is not reflected in the model, where it is limited from about the dynamic friction coefficient (~ 0.45, which is fixed by the global static friction coefficient) and the local static friction coefficient. The local static friction coefficient could of course have been increased, but this would in turn lead to much larger drops in F_X per global event. That is not desirable, since these drops then would get significantly larger than the drops observed experimentally, seen in Figure 3.2a. A local variation of the friction coefficients might allow high local stress ratios without disrupting the loading curve. This would, however, only affect the initial stress ratios, and not improve the model's discrepancies regarding the lack of slow ruptures and the possibility of infinitely fast ruptures.

These deviations arise from mainly two reasons: Firstly, the frictional interface is modelled using Amontons–Coulomb's law of friction. This is a macroscopic friction law, which is the result of averaging over many asperities. It is not expected that this simple friction law should produce the rather complex behaviour observed in experiments. It contains no time dynamics, and it is therefore not surprising that no slow ruptures are seen. Secondly, it is only a one-dimensional model. The real system is, of course, three-dimensional, which in addition to introducing a more complex geometry also introduces a new bulk wave speed, the shear wave speed c_S, and the possibility of surface waves. Two- and three-dimensional effects are therefore probably important to the rupture velocity.

Despite these discrepancies, the one-dimensional side driven model does provide useful insights into the rupture phenomena. The analysis has shown the importance of both the initial shear stress ratio and the interfacial strength. Some details remain to be understood, e.g. proving equation (5.29) and the importance of transients. Further analysis of the rupture phenomenon should be done with a different friction law, possibly one similar to that used in [16], exploring the importance of the frictional properties of the interface, and/or in at least two dimensions, as in [56], exploring the importance of dimensionality. Another interesting phenomenon not yet studied in experiments is front arrest. The process of how the two surfaces in frictional contact reattach might also be important in a geological context, e.g. regarding how earthquakes stop.

Chapter 6

Two new local friction laws

In this chapter, two new friction laws will be introduced. The first is a static friction law, which is motivated by the bad scaling of the side driven model with the number of blocks. It will be shown that changing the static friction law and thereby introducing a finite loading region can improve the scaling considerably. The second is a new dynamic friction law aimed at reproducing the time dependence of slip.

6.1 The spring-to-track static friction law

In this section, a new static friction law, named the spring-to-track static friction law, will be introduced and discussed. First, the motivation for introducing a modified friction law will be discussed. The friction law will then be introduced, and its consequences will be examined by both analytical calculations and simulations.

6.1.1 Motivation

The scaling of the side driven model with the number of blocks was discussed in section 4.11, and the number of events per time was shown to increase linearly with N. This is a rather unfortunate property of the model, since the results should not be that dependent on the resolution used in the model. One could say that the model is only valid for a given number of blocks, but multiplying the resolution by, say 10, should not completely change its behaviour.

In order to improve the scaling, the reason for the rather terrible scaling has to be understood. At $t = 0$, the driving force is 0, and as the driving point moves in time, the shear force on the first block increases. The first event will nucleate when $F_X^{(1)} = \mu_s w_1$, provided that there is no initial shear force, $F_n^{\text{n.f.},0} = 0$. Since the normal force on block 1 is inversely proportional to the number of blocks, the threshold force $F_X^{(1)}$ will also be proportional to $1/N$. As the number of blocks is increased, the first event will nucleate at an earlier time. This will also affect all other events as well, since the increase in the force F_X between two events will be proportional to $1/N$.

The scaling is caused by the fact that the loading region (the region that is affected by the driving), only consists of one block. When load is applied to a real (three-dimensional)

slider, a finite region about this point is affected by an increased stress. This region does not depend on the chosen resolution in a simulation, and is characterised by a length l_0. A solution to the scaling problem of the side driven model is in some way to include a finite loading region, even though the force has to be transferred through the only dimension available. One way to do this is to let the blocks move slightly even when they are experiencing static friction.

6.1.2 The model

This leads to the introduction of springs to the track as a static friction law. These springs allow blocks to move, but their movement is constrained. Each block is attached to the track by one spring, and these springs have spring constant k_t.

In order for rupture to occur, these springs also have to have a finite strength. To keep the new friction law as close to the Amontons–Coulomb static friction law as possible, each spring has a strength $\mu_s w_n$. If the spring force exceeds $\mu_s w_n$, the spring breaks. The static friction law is then replaced by the dynamic friction law, and in this phase, the Amontons–Coulomb dynamic friction law is used. When the velocity of the block reaches zero, the spring-to-track static friction law is applied again. The spring is then attached such that the sum of all forces on the block is zero. The reason for this is again to keep the new friction law as close to the Amontons–Coulomb law as possible: when the Amontons–Coulomb static friction law is applied after a block arrests, the size of the static friction force equals the sum of all other forces on the block, resulting in a zero net force.

The equations of motion for this system are still given by equations (4.2) and (4.5), but the friction force is now given by

$$\boxed{f_n = \begin{cases} f_n^s & \text{when } f_n^s \leq \mu_s w_n \\ -f_n^d & \text{when } \dot{u} > 0 \\ f_n^d & \text{when } \dot{u} < 0. \end{cases}} \tag{6.1}$$

The dynamic friction force $\pm f_n^d = \mu_d w_n$ is only applied if the track spring is disconnected, but is otherwise unchanged. The static friction force is now given by

$$f_n^s = -k_t(u_n - u_n^{\text{stick}}), \tag{6.2}$$

where u_n^{stick} is the attachment position of the spring. It is calculated form the shear force when the velocity reaches zero by

$$u_n^{\text{stick}} = u_n - \frac{F_n^{\text{n.f.}}}{k_t}. \tag{6.3}$$

The shear force profile as the first precursor is initiated using this friction law is shown in Figure 6.1. The shear force appears to decrease exponentially with a characteristic length l_0. It should be noted that the shear force need not equal the friction force, due to inertial forces. Figure 6.1 shows in reality the static friction force given by equation (6.2), however, if the loading is done slowly, leading to very small block accelerations, these two forces will be approximately equal.

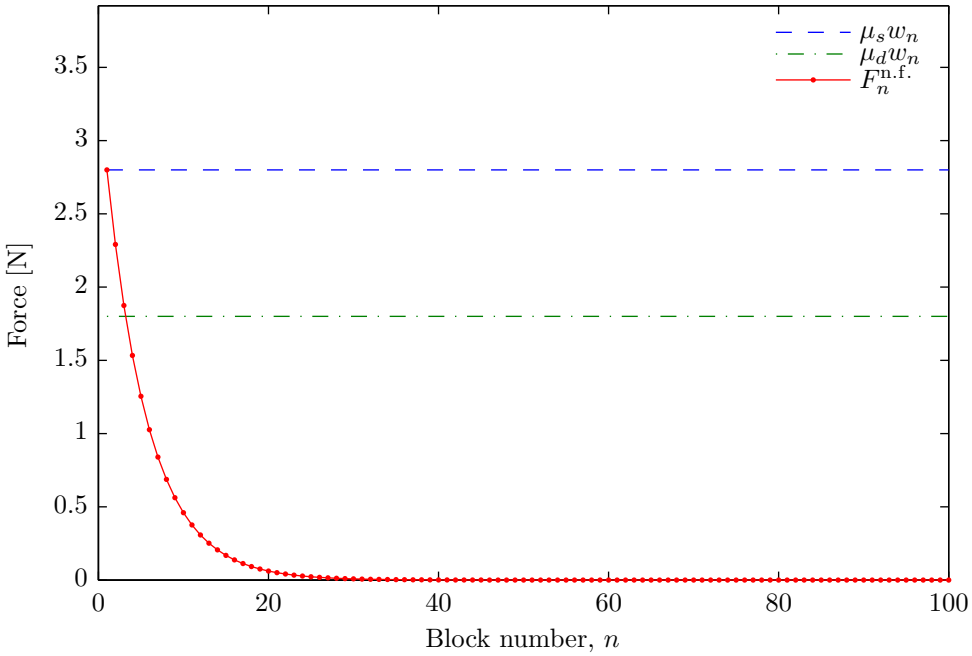

Figure 6.1: The shear force profile in the sample right before the first event for the spring-to-track static friction model, with $N = 100$, $k_t = 5EL_yL_z/L_x$.

If the characteristic length l_0 is independent of the number of blocks, then the force $F_X^{(1)}$ needed to start the first precursor is independent of N as well. However, this may require a scaling of the track springs k_t with N. To investigate this further, the static equations for this system are solved analytically.

6.1.3 Solving the static equations

In order to obtain a simple solution for the static problem, the length of the block L_x is assumed to be much larger that the characteristic length l_0. The number of blocks is also assumed to be large, meaning $l_0/L_x \ll 1$ and $N \gg 1$. The driven block is assumed to be loaded to the static friction level $\mu_s w_0$, and the leading edge blocks is then not affected because of the large system length L_x.

For all the blocks to be at rest, the sum of all forces on each block has to be zero, which means that

$$k(u_{n-1} - 2u_n + u_{n+1}) - k_t u_n = 0, \qquad n = 2, 3, \ldots, N-1. \tag{6.4}$$

The first term is the total spring force from neighbouring blocks, and the last term is the force from the spring connected to the track. It is assumed that there is no initial shear force, which means that the static friction force at $t = 0$ is zero and consequently u_n^{stick} is the initial position of each block, $u_n^{\text{stick}} = 0$. This is done for simplicity, it is possible to include an initial shear force profile with this static friction law as well.

The above equation can be rewritten to

$$k\left(\frac{L_x}{N-1}\right)^2 \frac{u_{n-1}-2u_n+u_{n+1}}{a^2} - k_t u_n = 0,$$

where $a = L_x/(N-1)$ is the equilibrium distance between the blocks. In the continuum limit, the position of block n, u_n, can be rewritten to $u(x_n)$, or just $u(x)$, where $x_n = na$. If a is small, i.e. if $N \gg 1$, the fraction in the above equation is an approximation to the second order spatial derivative,

$$\frac{\partial^2 u(x)}{\partial x^2} = \frac{u_{n-1}-2u_n+u_{n+1}}{a^2} + \mathcal{O}(a^2). \tag{6.5}$$

Inserting this into the equilibrium equation above yields the differential equation

$$\frac{\partial^2 u(x)}{\partial x^2} - \frac{k_t}{ka^2}u(x) = 0. \tag{6.6}$$

This is a linear first order ordinary differential equation, and the general solution is

$$u(x) = Ce^{x/l_0} + De^{-x/l_0}, \qquad l_0 = \sqrt{\frac{k}{k_t}}a, \tag{6.7}$$

where C and D are constants determined by the boundary conditions. In the discrete case, the shear force on block n, $F_n^{\text{n.f.}}$, during loading is related to the position of the blocks by the relation

$$F_n^{\text{n.f.}} = k(u_{n-1}-2u_n+u_{n+1}). \tag{6.8}$$

The relative viscous damping term has been ignored due to the slow dynamics during loading. In the continuous limit, this force is then given by

$$F^{\text{n.f.}}(x) = a^2\frac{\partial^2 u(x)}{\partial x^2}. \tag{6.9}$$

Using equation (6.7), the general form of the shear force is then given by

$$F^{\text{n.f.}}(x) = \frac{a^2}{l_0^2}\left(Ce^{x/l_0} + De^{-x/l_0}\right). \tag{6.10}$$

The constants C and D are given by the boundary conditions

$$F^{\text{n.f.}}(0) = \mu_s w_0, \qquad F^{\text{n.f.}}(x = L_x) = 0, \tag{6.11}$$

meaning that the first block is loaded up to the static friction threshold. The blocks on the leading edge do not feel the effect of the driving as a consequence of the small characteristic length l_0. The second condition yields

$$Ce^{L_x/l_0} + De^{-L_x/l_0} = 0,$$

and since $L_x/l_0 \gg 1$, the second term is negligible, resulting in $C = 0$. The first boundary condition then determines the constant D, by requiring

$$D\frac{a^2}{l_0^2} = \mu_s w_0,$$

meaning that the shear force right before the first precursor is given by

$$\boxed{F^{\text{n.f.}}(x) = \mu_s w_0 e^{-x/l_0}, \qquad l_0 = \sqrt{\frac{k}{k_s}}a, \qquad N \gg 1, \quad \frac{l_0}{L_x} \ll 1.} \tag{6.12}$$

As stated above, this is an exponential function with the characteristic length l_0.

The scaling of the characteristic length l_0 with N can now be investigated. In the physical system, the size of the stressed region is not dependent on the resolution in the calculations, meaning that l_0 should not scale with N. By inserting equation (4.10) for k into the expression for l_0 in equation (6.12), the characteristic length can be expressed as

$$l_0 = \sqrt{\frac{(N-1)EL_yL_z}{L_xk_t}}a = \sqrt{\frac{EL_yL_zL_x}{k_t(N-1)}}, \tag{6.13}$$

This expression obviously scales with N, however if the track spring constant k_t was to scale as $1/(N-1)$, the scaling of l_0 with N would be eliminated. By now defining $k_t^{\text{tot}} = (N-1)k_t$, the characteristic length is given by

$$\boxed{l_0 = \sqrt{\frac{EL_yL_zL_x}{k_s^{\text{tot}}}}, \qquad k_t = \frac{k_t^{\text{tot}}}{N-1}, \qquad N \gg 1, \quad \frac{l_0}{L_x} \ll 1.} \tag{6.14}$$

which, as stated, does not scale with N. The value of k_t^{tot} can then be determined by the desired size of the stressed region.

It is now possible to calculate the force $F_X^{(1)}$ needed to initiate the first precursor as a function of the size of the loading region l_0. For finite N, the force needed to initiate the first precursor is given by

$$F_X^{(1)} = \sum_{n=1}^{N} F_n^{\text{n.f.}} = \frac{1}{a}\sum_{n=1}^{N} F_n^{\text{n.f.}}a. \tag{6.15}$$

In the limit $N \gg 1$ and $l_0 \ll L_x$, $F_n^{\text{n.f.}}$ can be replaced by the continuous version in equation (6.12), and the sum can be approximated by an integral, leading to

$$\begin{aligned} F_X^{(1)} &= \frac{1}{a}\int_0^{L_x} F^{\text{n.f.}}(x)\,\mathrm{d}x \\ &= \frac{\mu_s w_0}{a}\int_0^{L_x} e^{-x/l_0}\,\mathrm{d}x \\ &= \frac{\mu_s F_Z}{Na}\left[-l_0 e^{-x/l_0}\right]_0^{L_x} \end{aligned}$$

Using $L_x/l_0 \gg 1$ and $N - 1 \approx N$ since $N \gg 1$, this leads to

$$F_X^{(1)} = \mu_s F_Z \frac{l_0}{L_x}. \tag{6.16}$$

6.1.4 Verification and consequences

In Figure 6.2, the driving force $F_X^{(1)}$ needed to initiate the first precursor is shown as a function of the inverse number of blocks for $l_0/L_x = 0.05$. It is clear that this force is

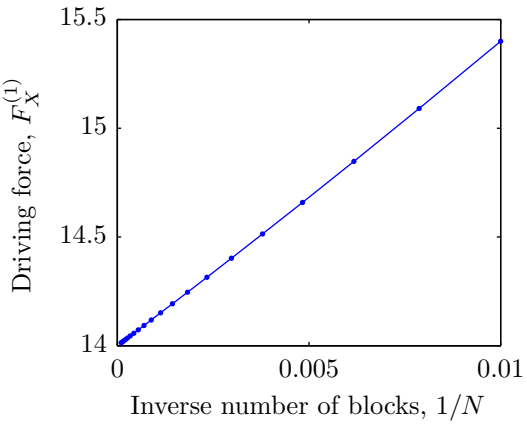

Figure 6.2: This figure shows the driving force $F_X^{(1)}$ needed to initiate the first precursor as a function of the inverse number of blocks with $l_0/L_x = 0.05$. The driving force then approaches $F_X^{(1)} = 14$ N, as given by equation (6.16).

converging to a specific force as $1/N \to 0$. By using equation (6.16), this force should be 14 N, which appears to be correct.

The needed scaling of k_t can be understood in a rather intuitive way. All the springs attached to the track is connected in parallel, meaning that the total spring constant for the connection to the track is given by Nk_t. This quantity should be independent of N because the strength of the connection to the track should not depend on the model resolution. Therefore, one can argue that $k_t \propto 1/N$ is the correct scaling for k_t.

Up until now, the spring-to-track static friction law has only been studied for static situations, i.e. where all time derivatives are zero. However, this does not prove that the N-dependence is eliminated when dynamics is considered. The rest of this section will therefore compare the dependence of the results on N for the old Amontons-Coulomb static friction law and the new spring-to-track static friction law for simulations with time dynamics.

In Figure 6.3, the number of global events is shown for simulations with both the old and new static friction law. For the Amontons–Coulomb static friction law, shown in Figure 6.3a, the scaling is approximately linear, where the number of events increases with the number of blocks, as discussed previously. The corresponding result for the spring-to-track static friction law, shown in Figure 6.3b, is on the other hand fairly constant.

The scaling of the mean slip per global event per block is shown in Figure 6.4. For the Amontons–Coulomb static friction model, shown in Figure 6.4a, the mean slip decreases towards zero when the number of blocks increase. The mean slip even appears to be proportional to $1/N$. For the spring-to-track static friction model, shown in Figure 6.4b, the mean slip appears to be fairly constant.

However, only global events are included in Figures 6.3 and 6.4. This was done in order to demonstrate the improvement, but the spring-to-track static friction law does not solve all problems with the side driven model. The number of very small events, involving only a few blocks, still seems to scale with N. Other results, such as the length of precursors, are still very similar to that obtained with the Amontons–Coulomb static friction law. The results presented in chapter 4 will therefore not be reproduced here using the spring-static-friction law.

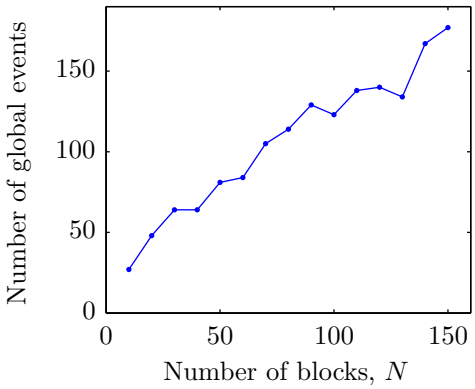

(a) Result obtained using the old Amontons–Coulomb static friction law.

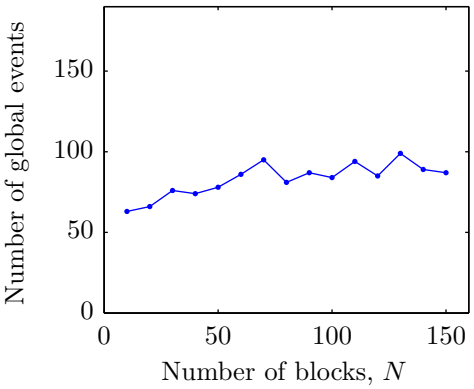

(b) Result obtained using the new spring-to-track static friction law with $l_0 = 5$ mm.

Figure 6.3: The number of global events in the first 20 s as a function of the number of blocks for the Amontons–Coulomb and spring-to-track static friction laws. All events in the first 5 s are ignored. Parameters are as in Table 4.1.

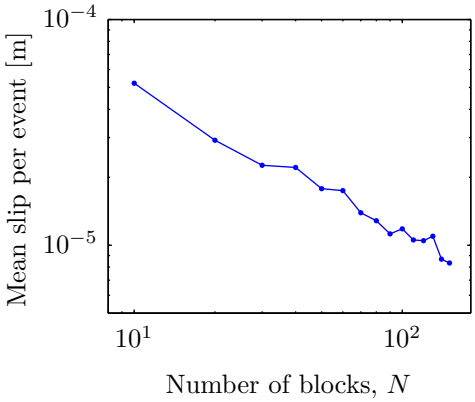

(a) Result obtained using the old Amontons–Coulomb static friction law.

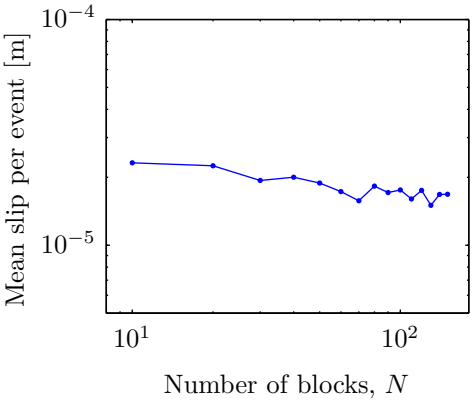

(b) Result obtained using the new spring-to-track static friction law with $l_0 = 5$ mm.

Figure 6.4: The mean slip length per block for global events in the first 20 s as a function of the number of blocks for the Amontons–Coulomb and spring-to-track static friction laws. All events in the first 5 s are ignored. Parameters are as in Table 4.1.

6.1.5 Summary and conclusion

This concludes the discussion of the spring-to-track static friction law. It has been shown that replacing the Amontons–Coulomb static friction law with springs to the track and scaling the spring constants in a particular way significantly improves the side driven model's scaling with N, because it keeps the size of the loading region constant. However, results such as the length of precursors and the qualitative behaviour of slip are still similar to that seen in chapter 4.

The spring-to-track static friction law can be interpreted in two ways. Firstly, it introduces a finite stiffness of the interface. The ensemble of asperities connecting the base and the slider have a finite stiffness, and the new friction law can be thought of as one possible way to model this. Modelling the yielding of asperities have been further investigated by Thøgersen [53], and the reader is referred to his thesis for a more detailed discussion. Secondly, it is a way to introduce force transfer from the driven block during loading, which is a two- and three-dimensional effect. This serves as yet another indication of the importance of the other two spatial dimensions.

6.2 A viscous dynamic friction law

In this section, an absolute viscous dynamic friction law will be introduced. This law, meant to replace the Amontons–Coulomb dynamic friction law, is motivated by the experimentally observed local slip seen in Figure 3.5, now given again in Figure 6.5. First, the new dynamic friction law is studied for a one block system. Results from this analysis are then used to study the effects on a chain of blocks.

6.2.1 Motivation

As discussed in section 4.7, the local slip in the side driven one-dimensional model was not in particularly good agreement with the experimental result in Figure 6.5. This was said to be a result of the Amontons–Coulomb friction, which is lacking the assumed physical effects behind the local slip curve described in section 3.2.

The local slip corresponds to the time development of the position of a block. This is an extremely important parameter in the model, since it basically determines the whole time development of the system. Particularly, the rupture velocities are also determined by the slip function. Consequently, a more realistic time dependence of the local slip might lead to dramatic changes in the results, maybe explaining some of the discrepancies seen between the experimental and model results. Perhaps even slow fronts may be observed.

The physical process causing the experimentally observed local slip was proposed in [6] to be a rapid heating of the interface due to the energy released when micro-contacts break. This heat would increase the temperature locally to above the glass temperature T_g, which would cause a local melting of the material. As a consequence, the shear strength of the interface would be weakened, causing the rapid slip seen in phase II in Figure 6.5. Then, as heat dissipates and the temperature decreases, the shear strength would increase, causing the slow slip seen in phase III and eventually slip arrest (phase IV).

Here, it will be investigated whether a simple viscous friction law is enough to reproduce this behaviour. Above the glass temperature T_g, the viscosity would be low. However, as the heat dissipates and the temperature decreases below the glass temperature, a rapid increase in the viscosity would occur. This may be a too crude description of the process, it may even be wrong. Despite this, investigating the consequences of using

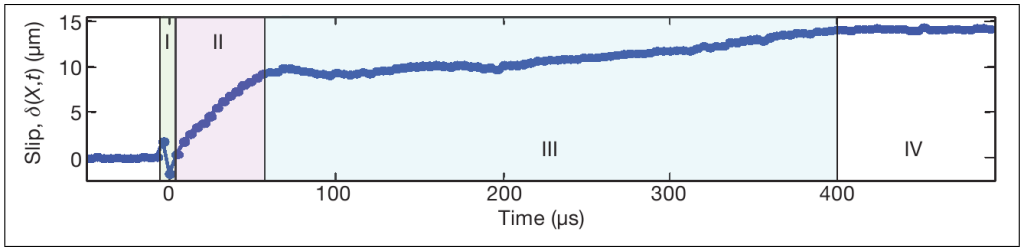

Figure 6.5: Local slip δ measured at a X adjacent from the interface as a function of time. It is divided into four different phases: local rupture of the interface (phase I), rapid slip (phase II), slow slip (phase III) and slip arrest (phase IV). From [6], Figure 2a.

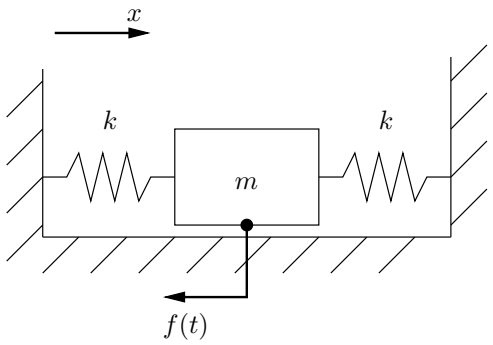

Figure 6.6: The simple system consisting of one block connected to a wall at both sides by springs with spring constant k.

a viscous friction law with a time dependent viscosity can give valuable new insights into the effects of the microscopic processes at the macroscopic level. In particular, would it be able to produce rupture velocities in better agreement with those observed in experiments?

6.2.2 The one block model

The one block modelled used in the first analysis is depicted in Figure 6.6. A block is connected to two springs, each with spring constant k, which in turn are connected to two walls. In addition to the spring forces, the block is influenced by a damping force $f(t, \dot{u})$, which is a function of both time and block velocity. The functional form of this force will be presented later.

Initially, at $t = 0$, the block is at rest and the block is loaded to the static friction level. The equation of motion is then given by equation (5.32), but with the dynamic friction force $\mu_d w_n$ replaced by the damping force $f^d(t, \dot{u})$, $k_l = k_r = k$, and $F^{\text{n.f.}}(0) = \mu_s w$, resulting in

$$m\ddot{u}(t) + (k_l + k_r)u(t) = \mu_s w + f^d(t, \dot{u}), \qquad u(0) = 0, \quad \dot{u}(0) = 0, \tag{6.17}$$

where $u(t)$ is the position of the block as a function of time. The functional form of $f^d(t, \dot{u})$ should be as simple as possible. According to the argument above, the viscosity should be low in the beginning (phase II), and then become much higher as the local temperature decreases below the glass temperature T_g (phase III). $f^d(t, \dot{u})$ is therefore chosen to be a traditional viscous friction law, where the force is proportional to the velocity, but where the viscosity itself is time dependent:

$$f^d(t, \dot{u}) = -\alpha(t)\dot{u}(t). \tag{6.18}$$

The transition in $f^d(t, \dot{u})$ as the temperature decreases below T_g is modelled as a rapid change in $\alpha(t)$. A possible functional form of $\alpha(t)$ including such a rapid change from one level to another is

$$\alpha(t) = \alpha_{\text{II}} + \frac{\alpha_{\text{III}} - \alpha_{\text{II}}}{2}\left[\tanh\left(\frac{t - t_c}{\tau_c}\right) + 1\right], \tag{6.19}$$

where α_{II} and α_{III} are the viscosity levels in phase II and III, respectively, t_c is the time at which the transition between phase II and III occurs (the cooling time), and τ_c is the rate of the transition. Because of the time dependence in the viscosity, equation (6.17) has

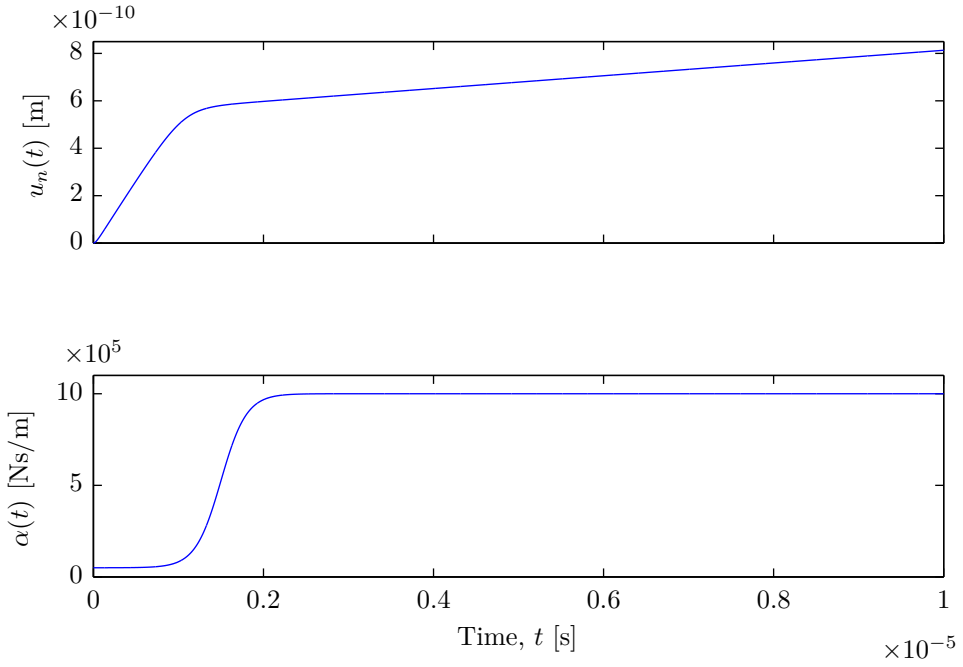

Figure 6.7: Result for the one block model obtained with the absolute viscous dynamic friction law using $\alpha_{\mathrm{II}} = 5 \times 10^4$ Ns/m, $\alpha_{\mathrm{III}} = 1 \times 10^6$ Ns/m, $t_c = 1.5 \times 10^{-6}$ s and $\tau_c = 3 \times 10^{-7}$ s. Other parameters are as in Table 4.1 with $N = 100$ and $\eta = 0$.

become much more complicated. The equation of motion is therefore solved numerically using the fourth order Runge-Kutta method described in section 2.3.

Different values for α_{II}, α_{III}, and τ_c were experimented with, and the result for one parameter set can be seen in Figure 6.7. The qualitative behaviour of the slip is now much more similar that seen in experiments, with first a rapid slip phase, and then a slow slip phase.

A qualitative understanding of the parameters in equation (6.19) can be obtained. As mentioned above, τ_c controls the rate of the transition in $\alpha(t)$, and consequently in $u(t)$ as well. The cooling time t_c controls when the transition occurs, and is for the many block system fixed to approximately 60 µs. The viscous damping levels α_{II} and α_{III} control how much slip occurs in phase II and III. There has to be a considerable damping in phase II as well as phase III, because in an undamped system the block would accelerate over a considerable time. This would cause $u(t)$ to have a positive curvature, while a negative curvature is observed in experiments. A difference in the viscosities in phase II and III of about one order of magnitude was needed in order to get the desired difference between the slip rates in phases II and III.

Neither the time nor the displacement have correct values according to the experimental data in Figure 6.7. This is expected, since adding more blocks to the system will cause both the time and displacement to change considerably. It will therefore be interesting to check if more realistic values for both parameters and slip will be obtained if the new viscous dynamic friction law is applied to a chain of blocks.

6.2.3 In a chain of blocks

The new viscous dynamic friction law will now replace the Amontons–Coulomb dynamic friction law in the one-dimensional side driven model. Since the slip is the object of interest, the Amontons–Coulomb static friction law cannot be used in combination with the side driven model, because the slip would then scale with the number of blocks. The solution is either to use the top driven model with Amontons–Coulomb static friction, or the side driven model with the spring-to-track static friction law. Since the slip is measured for precursor events in the experiments, and the top driven model needs an additional non-uniformity in order for precursor events to occur, the side driven model is used. Which of the models that are the most similar to the experimental system is open for debate, but as mentioned in section 4.7, slip should not be highly dependent on the driving mechanism since the driving velocity is very small compared to the rapid dynamics during slip. This statement holds when comparing the slip in the side and top driven models, and should hold for the experimental systems as well.

The equation of motion for this system is still given by equation (4.5), while the friction force f_n on block n is

$$f_n = \begin{cases} f_n^s & \text{when } f_n^s \leq \mu_s w_n \\ f_n^d(t, \dot{u}_n) & \text{when track spring is detached.} \end{cases} \tag{6.20}$$

The static friction force is given by equation (6.2), while the dynamic friction force is given by

$$f_n^d(t) = \alpha(t - t_n^d)\dot{u}_n, \tag{6.21}$$

where $\alpha(t - t_n^d)$ is given by equation (6.19), and t_n^d is the time track spring n detached. According to experimental results, the cooling time t_c is approximately 60 µs, and the duration of slip is about 400 µs. Therefore, $t_c = 60$ µs in the simulations, and the track spring is attached according to equation (6.3) 400 µs after it detached, restricting further movement of the block.

The slip as a function of time for one block in a precursor event is shown in the uppermost plot in Figure 6.8 for a given set of parameters. These parameters were optimised to get the best possible fit to the experimental result. Again the difference in viscosities in phase II and III are about one order of magnitude. However, both are reduced by approximately three orders of magnitude compared to the corresponding values used in the one block system.

The agreement with the experimental slip in Figure 6.5 is now much better. Initially, the slip is constant — the event has started, but the rupture front has not reached the point where slip is observed. Phases II and III are clearly distinguishable, where phase II has a high slip rate, and phase III has a lower slip rate. The transition occurs approximately 60 µs after initiation of slip, as given by t_c. The total slip distance of about 4 µm is also in agreement with experiment. The small oscillations seen both before and after rupture has initiated are caused by oscillating neighbouring blocks still attached to the track.

As can be seen in the lowermost plot in Figure 6.8, it is also possible to make a rough data collapse between the different precursors by normalising by the total slip in an event as was shown in Figure 3.6 for the experimental result. However, this is hardly surprising considering the explicit form of the friction law used: the transition will occur

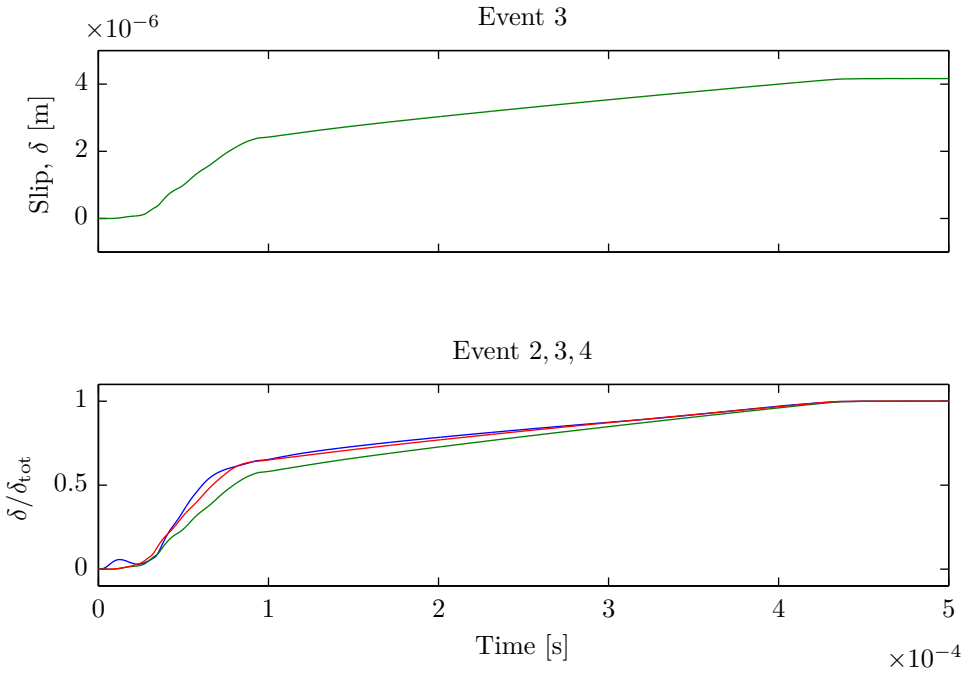

Figure 6.8: Slip as a function of time for one precursor (top) and normalised slip for three precursors (bottom) for block number 5 in a $N = 20$ block system with the absolute viscous dynamic friction law and the spring-to-track static friction law. Position and time are measured relative to the corresponding values at the beginning of the event. Parameters used are $\alpha_{\mathrm{II}} = 1 \times 10^2$ Ns/m, $\alpha_{\mathrm{III}} = 1 \times 10^3$ Ns/m, $t_c = 60$ µs, $\tau_c = 1$ µs, $\mu_s = 1$ and $l_0/L_x = 0.05$. Other relevant parameters are given in Table 4.1.

at approximately t_c and slip will arrest after 400 µs of slip. It is, however, interesting to observe that approximately the same fraction of the total slip occurs in phase II and III for different precursors.

6.2.4 Comparison with experimental viscosities

The viscosities used in the previous section should be related to the physical properties of PMMA. The viscosity of PMMA has been measured as a function of temperature [35], and it should in principle be possible to compare these viscosities to the ones found to work well in the model.

The experimental viscosities are viscosities defined from the behaviour of a fluid pressed between one stationary and one moving two-dimensional plate through the formula [17]

$$F = \alpha' A \frac{v}{y}, \tag{6.22}$$

where F is the resulting viscous force, α' is the viscosity, v is the velocity of the moving plate, A is the area of the plates and y is the spatial separation between the two plates. The area A should be large so that edge effects may be neglected. In the model, the viscosity is applied at the block level, meaning that $A = L_x L_y/N$ is the area of one block. Using this formula is sketchy, since the separation between the two plates, y, is

not well defined, and it assumes that the fluid is homogeneous, which may not be the case.

In principle, the viscosity α' in equation (6.22) could be converted to the same kind of viscosity used in the model by defining $\alpha = \alpha' A/y$. As an attempt at relating α to α', the value of y resulting in values of α approximately equal to the ones used in the simulations will be found. From [35], $\alpha' \approx 10^9$ Pas for the temperature $T \approx 0.95T_g$, where $T_g \approx 389$ K. Using $\alpha \approx 10^2$ Ns/m and $A = L_x L_y/N$, where L_x and L_y are given by Table 4.1 results in:

$$y = \frac{A\alpha'}{\alpha} = \frac{L_x L_y \alpha'}{N\alpha} \approx \frac{100 \text{ mm} \times 5 \text{ mm} \times 10^9 \text{ Pas}}{20 \times 10^3 \text{ Ns/m}} = 25 \text{ m},$$

which is several orders of magnitude larger than expected.

It should be noted that the viscosity of PMMA is seen to change rapidly for small changes in the temperature close to T_g. From $T = 0.92T_g$ to $T = 0.95T_g$, α' decreases from about 10^{11} Pas to about 10^9 Pas. It is therefore possible that the viscosity is low enough to get reasonable values for y when the temperature is about the glass temperature or above. However, only PMMA viscosities for $T \lesssim 0.95T_g$ were presented in the referred paper, making such an analysis rather difficult. It is clear, however, that the viscosity can indeed easily change an order of magnitude, as was seen to be necessary in the model, for small changes in the temperature around T_g.

6.2.5 Consequences to the global behaviour

The consequences to other measurements, such as the driving force F_X and the shear force $F_n^{\text{n.f.}}$, will now be investigated. The stick-slip plot for the same parameter set as that used in Figure 6.8 is shown in Figure 6.9. The system still shows stick-slip behaviour, with some precursors occurring before the first global event. The system is still in the slow driving regime, meaning that the position of the driving point is approximately stationary during an event. As long as this approximation is valid, the macroscopic friction level observed in the F_X-curve will be independent of the driving velocity, even though the dynamic friction law is now locally velocity dependent.

The time development of the shear force is shown in Figure 6.10, and here there are large deviations from the results obtained using the Amontons–Coulomb dynamic friction law. During the precursor events, the shear force does not stabilise at a certain level in the affected area, but is increased gradually even after the first global event. This is the cause of the gradual increase in F_X seen in Figure 6.9 event after the first global event: the shear force, and thereby the tangential force, has not reached its final level when the first global event occurs.

Another property of the F_X-curve that does not fit the experimental slip is the drop in the tangential force during an event. In Figure 6.9 the drops are much smaller than what is observed experimentally. Both these issues could be improved by reducing the effective viscosity so that the blocks would move a longer distance during an event. This, however, would reduce the number of precursors, and in Figure 6.9, there are only four to begin with. By trying out different values for the parameters α_{II}, α_{III}, τ_c and μ_s, the results shown in Figures 6.8 to 6.10 are the ones that are in best agreement with the experimental results.

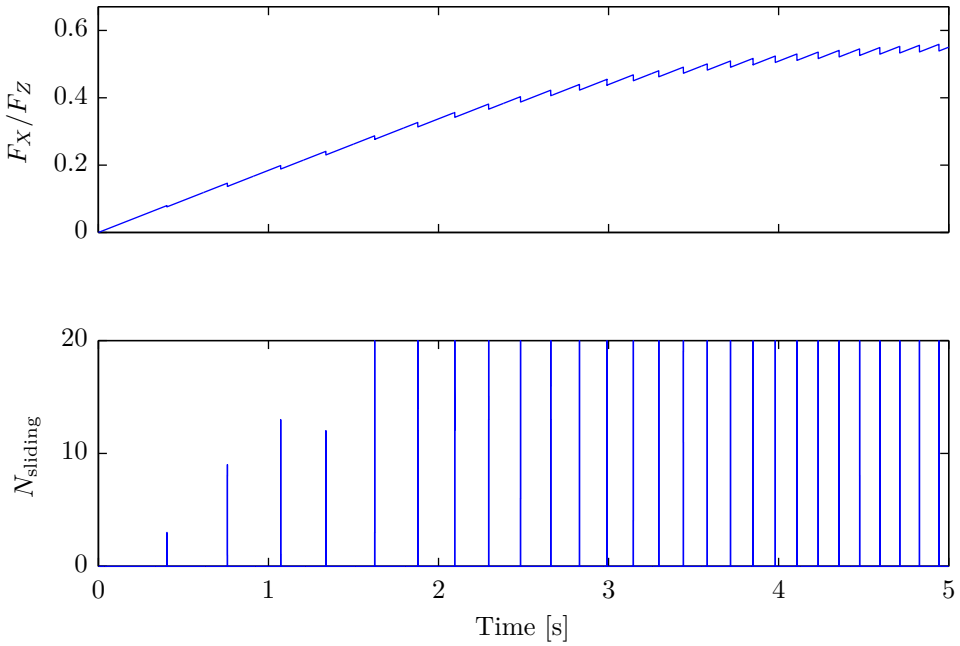

Figure 6.9: The stick-slip plot for a system with the new viscous dynamic friction law and parameters as in Figure 6.8. N_{sliding} is the number of track springs that is disconnected as a function of time.

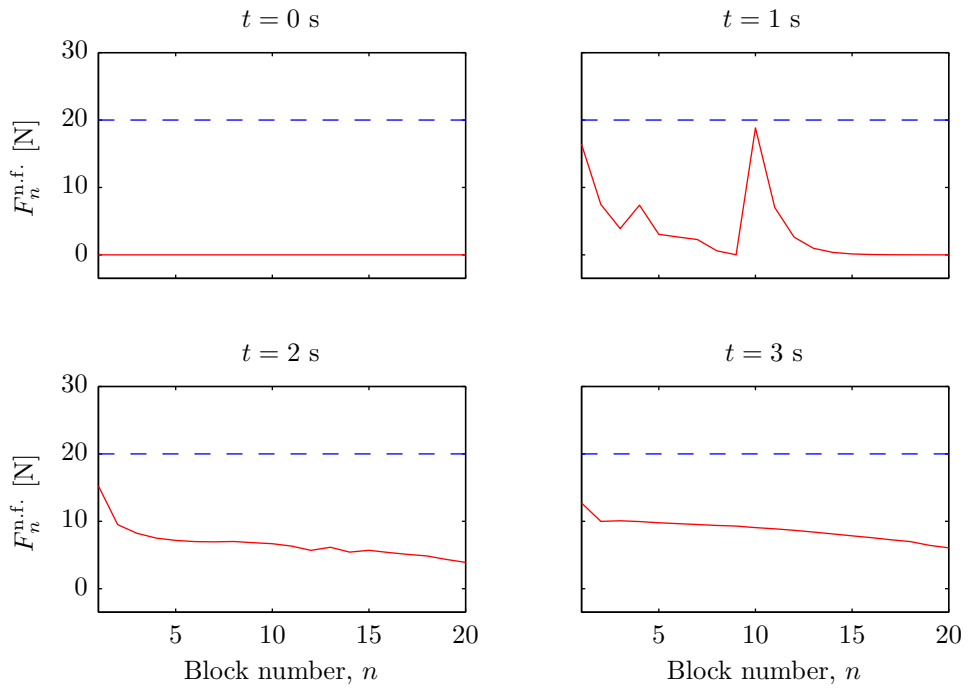

Figure 6.10: The time development of the shear force for a system with the new viscous dynamic friction law and parameters as in Figure 6.8. The dashed line is the static friction level $\mu_s w_n$.

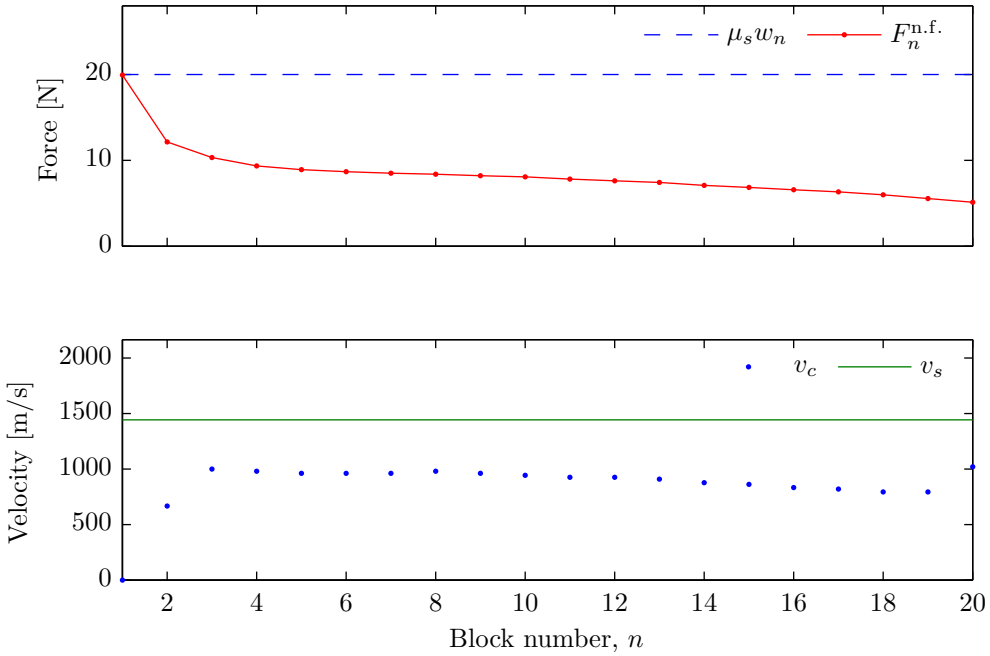

Figure 6.11: The initial shear force profile and the rupture velocity in a typical global event using the new dynamic friction model. Parameters as in Figure 6.8.

As a last result, the rupture velocity for a typical global event is plotted in Figure 6.11. It is clear that the variation in the shear force is quite small, resulting in an almost constant rupture velocity of about 1000 m/s.

6.2.6 Summary and conclusion

It has here been shown that using an absolute viscous dynamic friction law with a time dependent viscosity may result in local slips that are in much better agreement with the experimental results than obtained with a simple Amontons–Coulomb friction law. An absolute viscous friction law proved to be capable of reproducing both a rapid and a slow slip phase, with the resulting total slip quantitatively comparable to the experimental slips. It was also shown that the viscosities used may be compatible to experimentally obtained viscosities for PMMA, but this is not certain.

However, it was also shown to increase the deviation between the model and experiments in the loading curve $F_X(t)$. The average applied tangential load was seen to increase even after the first global event had occurred, and the global events resulted in much smaller drops in $F_X(t)$ than experimentally observed. Clearly, some underlying physical effects are missing. These effects may be connected to the coupling between the static and dynamic friction law, which are now applied independently of each other.

Slow ruptures were not observed. This may be due to the importance of the detachment phase (phase I in Figure 3.5), since this is not taken into account in the viscous dynamic friction law. This is where the slider detaches from the base, which then should be the most important phase in how a rupture propagates along the interface. This serves as

further indication of the importance of the coupling between the static and dynamic friction law. In addition, all results for local slips in [6] were obtained for precursor events only. Jay Fineberg said in a talk in Lyon, France on 17 March 2011 that no slow ruptures have been observed for precursor events. Figure 3.5 may then not reflect the physical processes causing slow fronts.

Chapter 7

The (2 + 0)D spring-block model

The one-dimensional model considered so far has been shown to not be able to reproduce the experimental results to a satisfactory degree. It has been suggested that some of these deviations may be due to the dimensionality of the system, since including two-dimensional effects such as an initial shear force profile and a finite loading region seems to improve the model results.

Before moving on to a system with three spatial dimensions, it is usually wise to consider a two-dimensional system. The reason is that including more dimensions usually makes the dynamics of a system more complex, meaning that it will be more difficult to interpret the results. The importance of each dimension will also be clearer if the are added one by one. In addition, the equations of motion will be more demanding from a computational perspective, requiring more CPU time for the same spatial resolution.

There are, of course, two remaining spatial dimensions: the second horizontal and the vertical. Considering the sketches of the experimental system in Figure 3.1b, the most natural thing to do is to include the vertical dimension. This model is then called the (1 + 1)D model, because it has one horizontal dimension and one vertical dimension. For an extensive discussion of this model, see [56].

In this chapter, the second horizontal dimension is included, making it a (2 + 0)D model. In one way, this system is much more similar to the one-dimensional model since all blocks are still in frictional contact with the track. Effects due to e.g. the non-uniform distribution of the normal stress due to edge- and elasticity effects are not included. This is not to say that the model will be equal to the one-dimensional model. The Poisson effect will still be included in the horizontal plane, and the driving may now be applied in several different ways.

A (2 + 0)D version of the Burridge-Knopoff model has previously been studied in e.g. [20], but then in a more earthquake-like setting, where different measures for the size of the events (earthquakes) were considered. In this chapter, the (2 + 0)D model is discussed in a frictional context.

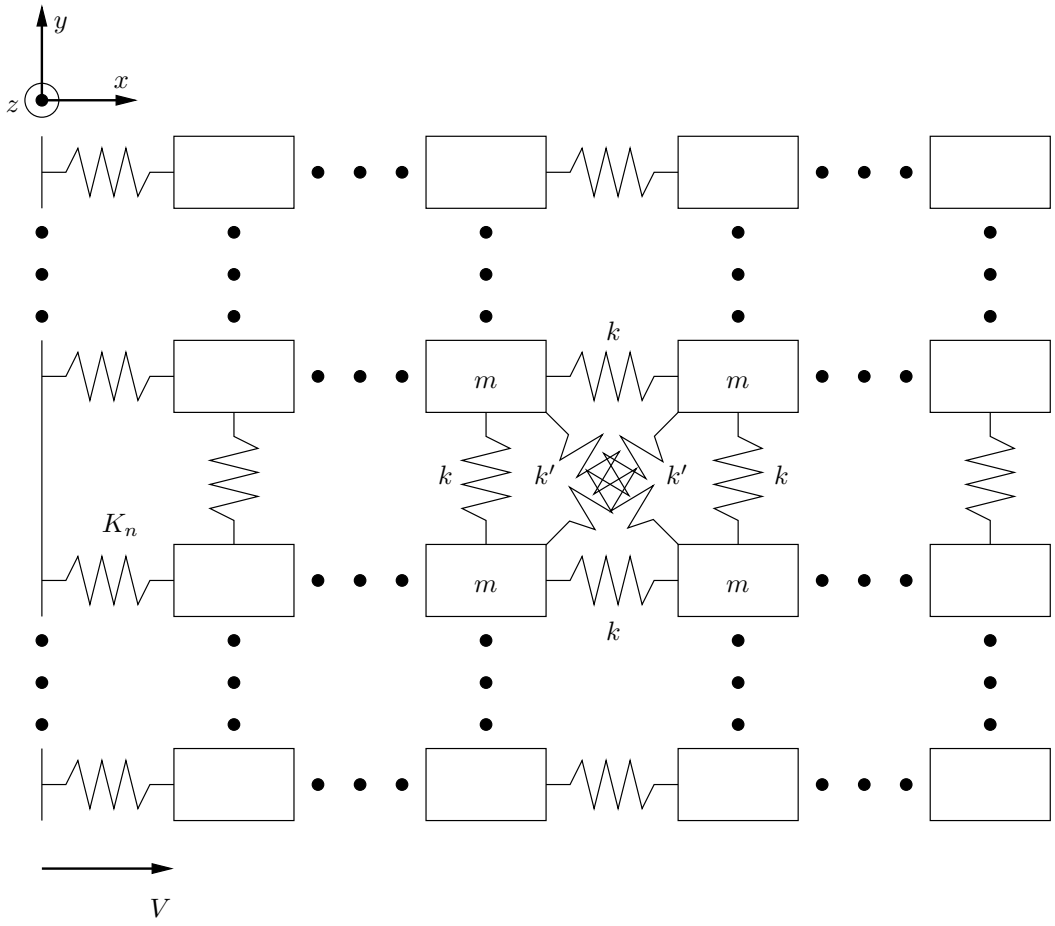

Figure 7.1: Schematic drawing of the (2 + 0)D model driven from the side. All blocks except edge blocks are connected to their nearest neighbours and next nearest neighbours by springs of spring constants k and k', respectively, and all blocks are in frictional contact with the track.

7.1 The model

A schematic drawing of the (2 + 0)D system driven uniformly from the side can be seen in Figure 7.1. All blocks are in contact with the frictional interface, and the blocks are placed in a quadratic grid where each block (except the edge blocks) has eight neighbours. A block is connected to its nearest neighbours by springs with spring constant k, and its next nearest neighbours by springs with spring constant k'.

The reason for adding the springs to the next nearest neighbours is to get a finite Poisson's ratio: without these springs, the x- and y-direction would not be directly coupled, meaning that a compression in the x-direction would not lead to a compression in the y-direction, and vice versa.

The (2 + 0)D system is in other aspects very similar to the 1D system, but quantities such as slip, velocities and forces are now two dimensional quantities, represented by vectors. The equation of motion for block n is

$$\boxed{m\ddot{\mathbf{r}}_n = k\sum_{\langle j\rangle_1}(r_{nj}-l_1)\,\hat{\mathbf{r}}_{nj} + k'\sum_{\langle j\rangle_2}(r_{nj}-l_2)\,\hat{\mathbf{r}}_{nj} + \eta\sum_{\langle j\rangle_{1,2}}(\mathbf{v}_j-\mathbf{v}_n) + \mathbf{f}_n + \mathbf{F}_n^K,} \quad (7.1)$$

where $\langle j \rangle_1$ denotes all nearest neighbours and $\langle j \rangle_2$ denotes all next nearest neighbours, η is the relative damping coefficient, $\mathbf{f}_n$ is the friction force and $\mathbf{F}_n^K$ is the driving force on block n. For blocks that are not driven, $\mathbf{F}_n^K$ is zero at all times. $\mathbf{r}_n$ is the position of block n, $\mathbf{v}_n = \dot{\mathbf{r}}_n$ is the velocity of block n, and $\hat{\mathbf{r}}_{nj}$ is the unit vector directed from block n to block j:

$$\hat{\mathbf{r}}_{nj} = \frac{\mathbf{r}_j - \mathbf{r}_n}{|\mathbf{r}_j - \mathbf{r}_n|} = \frac{\mathbf{r}_j - \mathbf{r}_n}{r_{nj}}.$$

The number of blocks in the x-direction is denoted by N_x, and the number of blocks in the y-direction N_y. The total number of blocks is then given by $N = N_x N_y$.

The Amontons–Coulomb friction law is used, where the friction force on block n is given by

$$\mathbf{f}_n = \begin{cases} \mathbf{f}_n^s & \mathbf{v}_n = \mathbf{0} \\ \mathbf{f}_n^d & \mathbf{v}_n \neq \mathbf{0} \end{cases}, \tag{7.2}$$

where $\mathbf{f}_n^s$ and $\mathbf{f}_n^d$ are the (local) static and dynamic friction on block n, respectively. The local static friction takes values in the range

$$0 \leq |\mathbf{f}_n^s| = f_n^s \leq \mu_s w_n, \tag{7.3}$$

where μ_s is the (local) static friction coefficient and w_n is the normal force on block n as in the one-dimensional model. The static friction force is now a vector quantity which is equal in size and oppositely directed from the sum of all other forces on a block. The local dynamic friction is now also a vector quantity, given by

$$\mathbf{f}_n^d = -\hat{\mathbf{v}}_n \mu_d w_n, \qquad \hat{\mathbf{v}}_n = \frac{\mathbf{v}_n}{|\mathbf{v}_n|}. \tag{7.4}$$

The normal weights w_n are given by equation (A.18), where the block index n is substituted for the block index in the x-direction, n_x:

$$w_n = \frac{F_Z}{N}\left(1 + \frac{2n_x - N_x - 1}{N_x - 1}\theta\right), \qquad n_x = \text{floor}\left(\frac{n-1}{N_y}\right) + 1. \tag{7.5}$$

The standard set of parameters used is given in Table 7.1. It should be noted that a small randomness is added to the friction coefficients in order to loose the perfect symmetry about the x-axis present in the system. This is explained in more detail in Appendix B.2. Some numerical details on solving equation (7.1), including how to choose the time step, are also given in Appendix B.2. In all simulation results presented in this chapter, a time step $\Delta t = 3 \times 10^{-8}$ s was used ($N_x = N_y = 50$), which is less than the estimated period of oscillation for one block 2×10^{-6} s.

7.2 Driving

In order for the driving to not disturb the expansion of the system in the y-direction due to the Poisson effect, the driving force is chosen only to act in the direction of the driving, i.e. along $\mathbf{V}$. This means that the driving springs depicted in Figure 7.1 only exert forces in the x-direction, and none in the y-direction. In addition, the size of this

Physical quantity	Symbol	Value in simulation
Total slider mass	M	0.048 kg
Young's modulus	E	2.5 GPa
Sample length	L_x	120 mm
Sample depth	L_y	120 mm
Sample height	L_z	40 mm
Static friction coefficient	μ_s	0.70 ± 0.01
Dynamic friction coefficient	μ_d	0.45 ± 0.01
Relative viscous damping	η	$\sqrt{0.1}\sqrt{km}$
Total normal force	F_Z	400 N
Driving point velocity	V	0.1 mm/s
Total driving spring constant	K	0.8 MN/m
Local driving spring constant	K_n	K/N_d

Table 7.1: Overview of the physical constants and parameters used in the simulation of the (2 + 0)D model. Most of these parameters are the same as for the one-dimensional model in Table 4.1, but some have been altered in order to study square systems. The friction coefficients are drawn from a uniform distribution in the indicated intervals.

force is chosen to be independent of the displacement in the y-direction. The driving force on block n is then given by

$$\boxed{\mathbf{F}_n^K = \left(K_n(\mathbf{V}t + \mathbf{r}_n^0 - \mathbf{r}_n(t)) \cdot \hat{\mathbf{V}}\right)\hat{\mathbf{V}}, \qquad \hat{\mathbf{V}} = \frac{\mathbf{V}}{V},} \tag{7.6}$$

where K_n is the driving spring constant for block n, $\mathbf{V}$ is the driving velocity vector, $V = |\mathbf{V}|$, t is the time, $\mathbf{r}_n^0$ is the position of block n at $t = 0$, and $\mathbf{r}_n(t)$ is the position of block n at time t.

The system depicted in Figure 7.1 is driven from the side, but this is of course not the only way to drive the system. The different methods of driving the system considered here are:

- Side driven: This is the driving that is the most similar to the side driven one-dimensional model. All blocks on the trailing edge experience a driving force exerted by the same harmonic potential.
- Point driven: Only the middle one/two block(s) on the trailing edge feel a driving force, but in other aspects it is equal to the side driving.
- Top driven: This is the (2 + 0)D version of the top driven one-dimensional model, all blocks are driven by the harmonic potential. As was the case in one dimension, a tilt θ or an additional torque effect is needed in order for the whole block not to begin sliding at the same time. Only the result of including a tilt θ will be discussed here.

The driving spring constants on the driven blocks are still chosen to be

$$K_n = K/N_d, \tag{7.7}$$

where K is the driving spring constant used in the one-dimensional side driven model and N_d is the number of driven blocks.

7.3 Choosing the spring constants: Young's modulus and Poisson's ratio

In the one-dimensional model, the spring constant k was chosen such that the system would behave as an elastic object with a specific value of Young's modulus. This was done by calculating the total effective spring constant of the material and relating this to the definition of Young's modulus.

The same is also possible in two dimensions, but the situation is more complicated. Consider the system depicted in Figure 7.1, but without the attached driving springs and with friction turned off. A force F is then applied on each of the edges normal to the x-direction in opposite directions (in order to make the sum of all external forces on the sample zero). This force will cause a compression/expansion of the sample in the x-direction, and because of the Poisson effect, there will also be an expansion/compression in the y-direction.

The relation between the spring constants k and k', and Young's modulus E and the Poisson's ration ν for an infinite two-dimensional system has been derived [38]. It was found that for $k' = k/2$, the system behaves as a two-dimensional isotropic continuum, and that the relations are

$$\boxed{E = \frac{8}{3L_z}k', \qquad \nu = \frac{1}{3}, \qquad k' = k/2.} \tag{7.8}$$

It is worth mentioning that if the system is to behave as a two-dimensional isotropic continuum, then the Poisson's ratio ν cannot be chosen, but is fixed to 1/3. Luckily, the Poisson ratio for PMMA is $\nu = 0.33$ [5, supplementary], by a fortunate coincidence. The value of Poisson's ratio can be adjusted if bond-bending is included in the model. A derivation of equation (7.8) is located in Appendix B.1.

The result given in equation (7.8) is only valid for infinite systems and small displacements. For a small system, for example a 2×2-system, the result is quite different. It can be shown with a similar calculation as that done in Appendix B.1 that for this system, Young's modulus is given by $E = (24/5)k'/L_z$ and Poisson's ratio is $\nu = 1/5$. The two-dimensional systems considered here is, of course, finite, and their Young's modulus and Poisson's ratio are approximately given by equation (7.8). Since the systems considered here are quite large, the approximation should be quite accurate, and this will be verified below.

7.4 Oscillations and relative viscous damping

In the one-dimensional model, a relative viscous damping was included to dampen out unwanted oscillations with wavelength $2a$, where a is the lattice spacing. The coefficient of damping η was chosen to be slightly below the value corresponding to critical damping of waves with this wavelength in order to minimise the impact on other wavelengths.

In two dimensions, a relative damping can be introduced in two ways. One possibility is to dampen oscillations in the spring lengths, while another is to dampen the relative motion of the blocks. This was not an issue in the one-dimensional model, since the

two dampings there are one and the same. In the two-dimensional model, the relative motion of the blocks is damped, leading to the damping term in equation (7.1).

It then remains to find a reasonable value for η, as was done for the one-dimensional model. However, because of the increased complexity of the geometry of the system, a calculation similar to that done in Appendix A.1 for the one-dimensional model will be extremely cumbersome. In addition, the two-dimensional model considered here is quite similar to the one-dimensional model, and it is therefore reasonable to assume that the value for critical damping of the short-wavelength oscillations will be on the same order of magnitude as that found for the one-dimensional model, given in equation (A.12). The spring constant k in this equation should be replaced by an effective spring constant, which is larger than both k and k'. In addition, damping will also originate from more blocks, increasing the effective damping coefficient.

Since the exact value corresponding to critical damping for η is not important, only that it is somewhat below this value, η is in simulations of the two-dimensional model chosen to be

$$\eta = \sqrt{0.1}\sqrt{km}, \tag{7.9}$$

where k is the spring constant of springs to nearest neighbours. The results given here do not vary significantly by changing η.

7.5 First model results

7.5.1 Verification of the code

As for the one-dimensional model, verification of the code is important. Again an analytically solvable special case has to be found, and the analytical solution should then be compared to the numerical solution. The important parts of the code that should be checked are the starting and stopping of blocks, the skipping of stick periods and the integration algorithm itself, as in the code for the one-dimensional model.

The two-dimensional system is more complicated than the one-dimensional, and in order to solve the dynamics of the system analytically, some simplifications have to be made. By setting the spring constant $k' = 0$, but still keeping the original values for k, the system is decoupled in the x- and y-directions. The first event involving only the blocks with $n_x = 1$ can then be examined more closely.

Using the two-dimensional model driven from the side will then effectively be a one-dimensional system, and the analytical solution is again given by equation (4.25). The comparison of the analytical and numerical solutions is shown in Figure 7.2, corresponding to Figure 4.3 for the one-dimensional model. The same behaviour is seen for the two-dimensional model as for the one-dimensional model: the starting and stopping of blocks, skipping of stick periods and the integration algorithm are working.

7.5.2 Verification of Young's modulus and Poisson's ratio

To verify the values of the spring constants k and k' used, Young's modulus and Poisson's ratio are calculated as a function of the number of blocks in the x-direction, N_x. This is

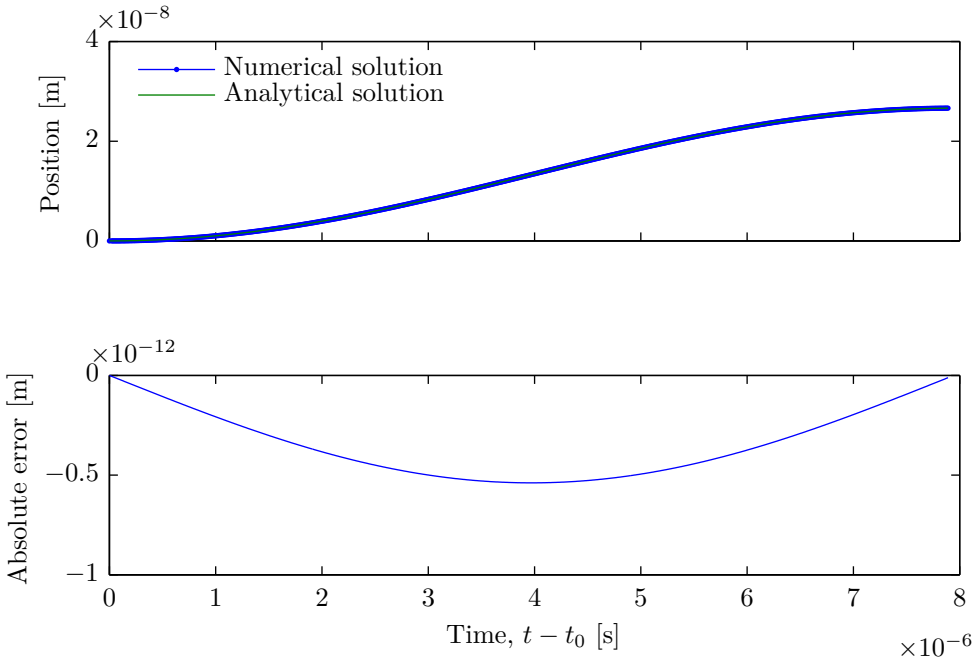

Figure 7.2: The uppermost plot shows the x-position of block 1 as a function of time for the first event in the side driven two-dimensional model, where both the numerical and analytical solutions are shown. The lowermost plot shows the absolute error in the numerical solution as a function of time. $N_x = N_y = 10$, $\theta = 0$ and $\eta = 0$. Other parameters are as in Table 4.1. The spring constant k' has explicitly been set equal to zero, while the value for k is still given by equation (7.8).

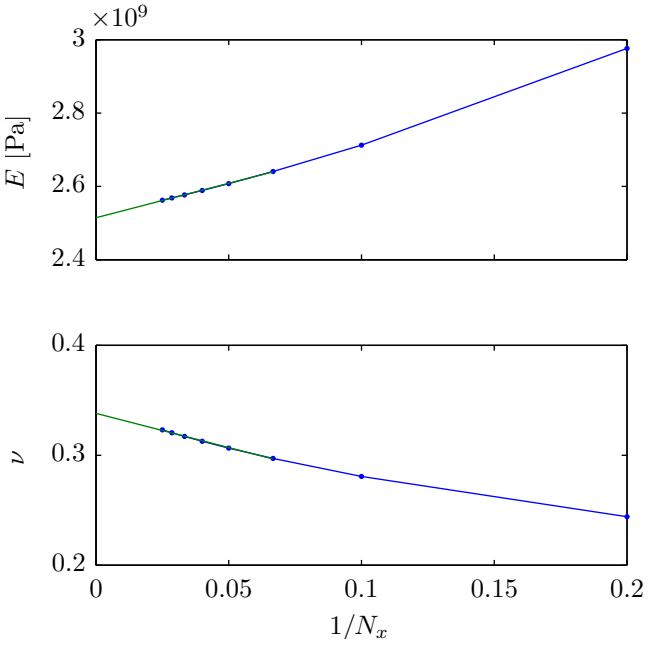

Figure 7.3: Young's modulus E and Poisson's ratio ν as functions of N_x given that the spring constants k and k' are calculated from equation (7.8). Young's modulus should approach $E = 2.5$ GPa while Poisson's ratio should approach $\nu = 1/3$.

done by setting both friction coefficients equal to zero for all blocks except those at the leading edge, which get an extremely high static friction coefficient. The blocks at the leading edge are then stuck, while all other blocks move without friction. The driving force is then applied to all blocks at the trailing edge, resulting in a compression of the system in the x-direction and an expansion in the y-direction. The size of the slider in both the x- and y-direction as a function of the applied driving force can then be calculated from the simulation result. Equation (2.7) and (2.8) are then used to estimate Young's modulus and Poisson's ratio for a given number of blocks.

The result from many such simulations can be seen in Figure 7.3, where Young's modulus and Poisson's ratio calculated from the simulation result are plotted as functions of the inverse number of blocks in the x-direction, N_x. They are both seen to converge to approximately their values in the large system limit, where $E = 2.5$ GPa and $\nu = 1/3$. The linear fits shown in the figure do not match these values exactly. That is not to be expected, since there is nothing saying it should be a straight line, and there are small uncertainties in the numerically calculated values of E and ν. Figure 7.3 is taken as a confirmation of equation (7.8) and that the code is working.

7.5.3 Stick-slip behaviour

The stick-slip plot for the two-dimensional model with uniform side driving is shown in Figure 7.4. The figure shows that the (2 + 0)D model exhibits similar stick-slip behaviour as that seen in the one-dimensional model. Unfortunately, the (2 + 0)D model has the same problem regarding the scaling with the number of blocks. The reason is the same as for the one-dimensional side driven model: no force is transferred from the driven blocks to their neighbouring blocks while stationary. This could again be improved by introducing the spring static friction law in two dimensions, but that is not within the scope of this thesis.

7.5.4 Shear force profile

The shear force profile for three different cross sections for side and point driving are shown in Figure 7.5 and 7.7, respectively. Again, most of the behaviour is similar to that of the one-dimensional model, but there are some differences worth noting.

For the side driving, shown in Figure 7.5, the front has reached further at the two edges of the slider. This is a result of the Poisson effect causing a non-zero shear force in the y-direction at the edges of the slider, which in turn causes the static friction threshold to be reached first at the edges. Other than that, there are no large differences between the side driven two-dimensional model and the side driven one-dimensional model.

For the top driven model, shown in Figure 7.6, there is practically no difference between the two-dimensional and the one-dimensional model. It is only a coincidence that the edge $n_y = 50$ appears to be ahead of the others. At other times, it may be $n_y = 25$ or $n_y = 1$ which is leading. The point driven model, however, shown in Figure 7.7, shows a behaviour quite different from the one-dimensional model, and deserves some extra discussion. In the frame showing the shear force at $t = 1$ s one can see that the shear force is unaltered at the two sides of the slider. In the middle, on the other hand, the shear force is increased over halfway towards the leading edge.

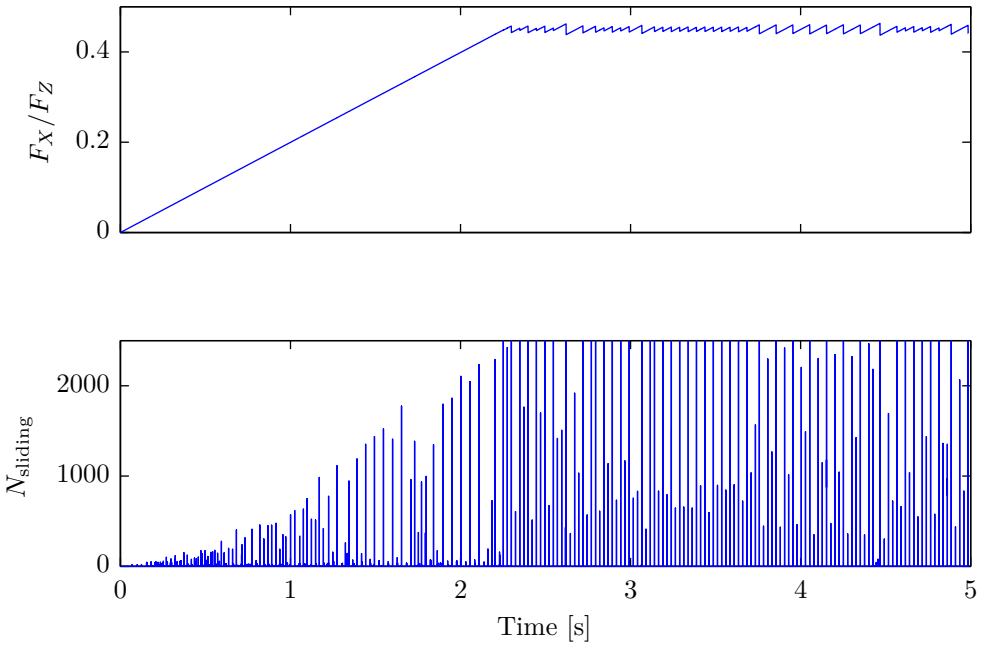

Figure 7.4: The stick-slip plot for the side driven two-dimensional model. Similar results are obtained for both the top and point driven models as well. This result was obtained by using $N_x = N_y = 50$ and $\theta = 0$, other parameters as in Table 7.1.

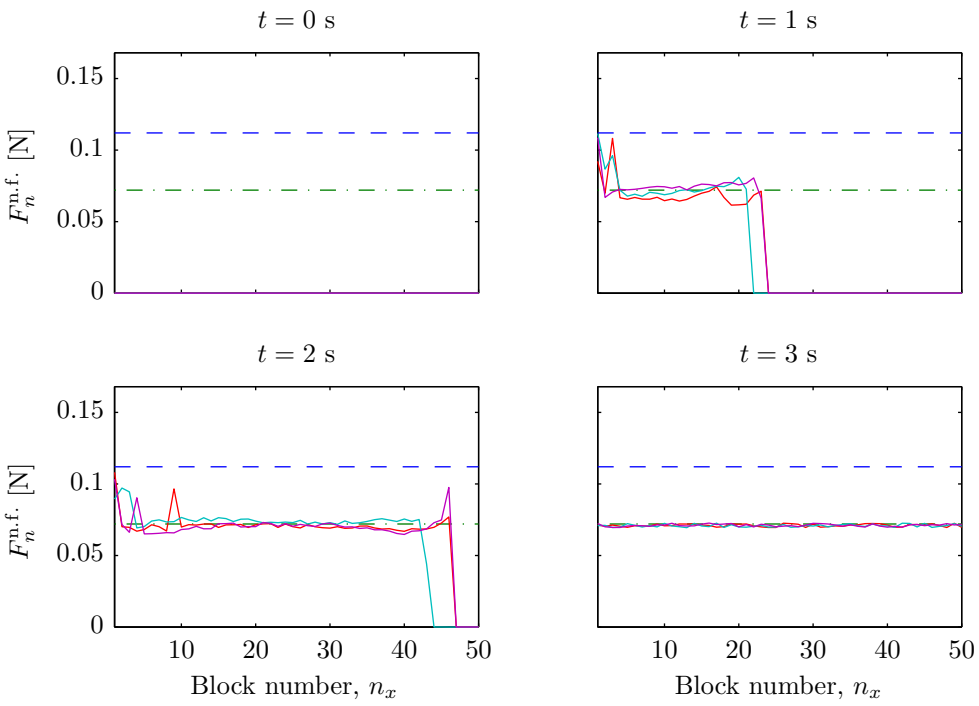

Figure 7.5: Time development of the shear force in the two-dimensional side driven model. The blue dashed line is the static friction level, the green dashed-dotted line is the dynamic friction level, and the three drawn lines are the shear force at three different cross sections: The red is at $n_y = 1$, the cyan is at $n_y = 25$, and the purple is at $n_y = 50$. Simulation is done with $N_x = N_y = 50$ and $\theta = 0$, while other parameters are as in Table 7.1.

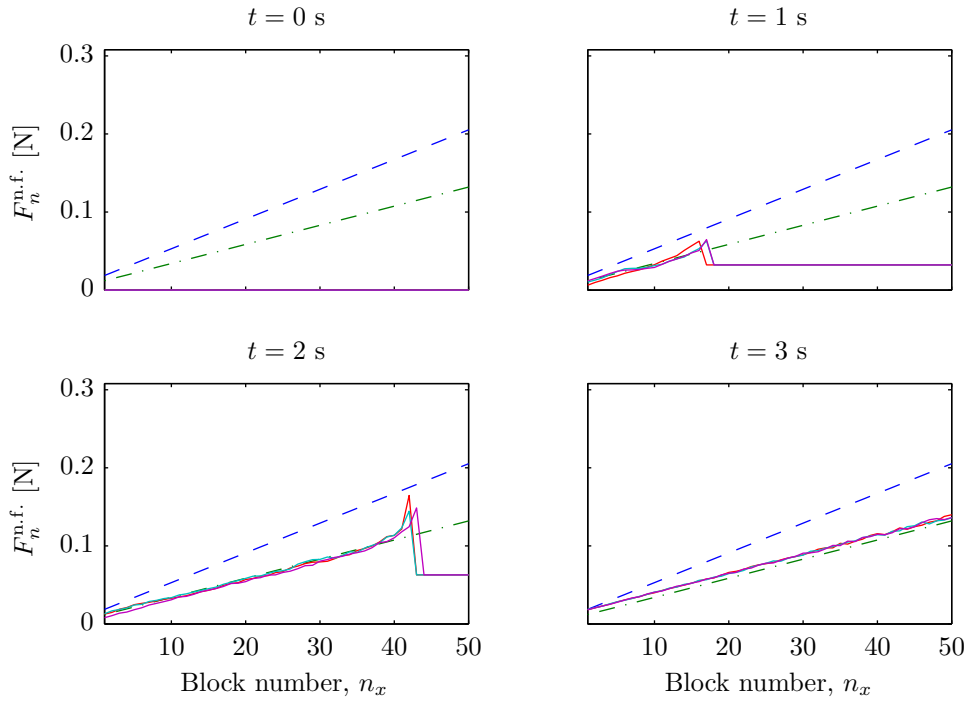

Figure 7.6: Time development of the shear force in the two-dimensional top driven model. Legends are the same as in Figure 7.5. Simulation is done with $N_x = N_y = 50$ and $\theta = 0.833$, while other parameters are as in Table 7.1.

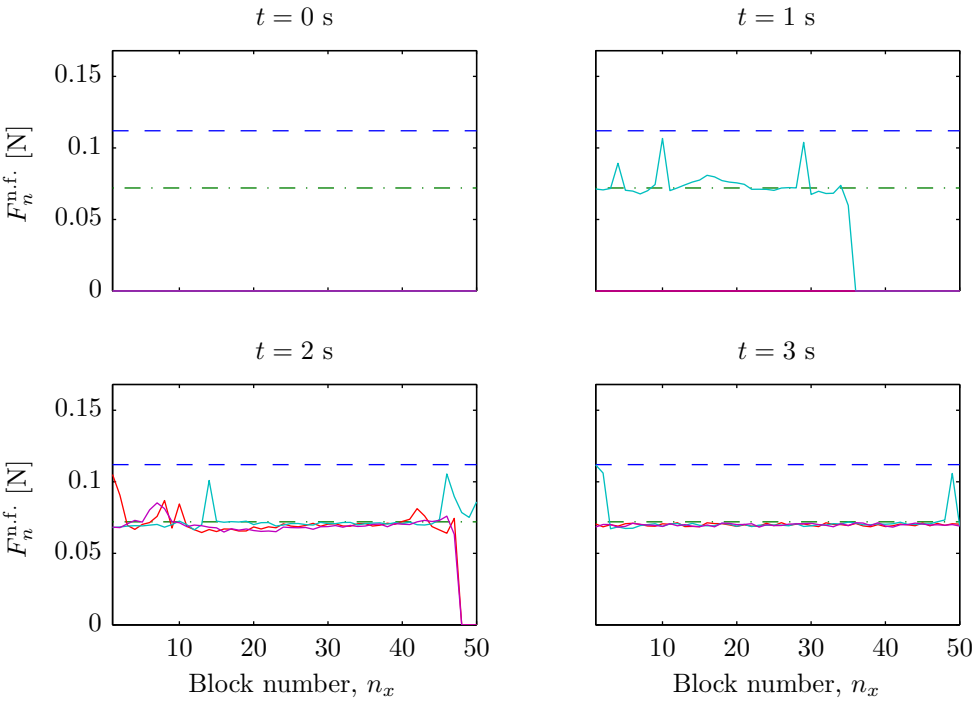

Figure 7.7: Time development of the shear force in the two-dimensional point driven model. Legends are the same as in Figure 7.5. Simulation is done with $N_x = N_y = 50$ and $\theta = 0$, while other parameters are as in Table 7.1.

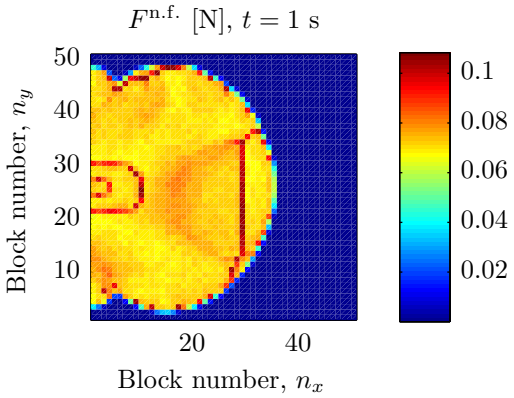

Figure 7.8: This figure shows the size of the shear force on each block for the point driven model at $t = 1$ s. The funny shape is a consequence of the driving, every event will be initiated at the two middle blocks in the y-direction along the trailing edge. The dynamic friction level is in this case at $\mu_d w_n = 0.072$ N.

To illustrate the situation better, the shear force on each block is plotted in Figure 7.8. The particular shape is a consequence of the highly singular driving used. All events originate from the two middle blocks at the trailing edge, and each precursor propagates radially from this point. Therefore, the precursors reach quite far into the sample before blocks at the two sides, $n_y = 1$ and $n_y = N_y$, start to move.

7.6 Length and size of precursors

The length of the precursors as a function of the tangential load has been measured for all driving mechanisms. The two-dimensional definition of the length of a precursor is the distance from the tip of the precursor to the trailing edge along the direction of driving. The result is shown in Figure 7.9a. As expected, the side and top driving do not differ significantly from the one-dimensional result with the corresponding driving. However, for the point driven model, quite long precursors are possible even for small tangential loads.

This can be understood from Figure 7.8. Fewer blocks have to be loaded up to the dynamic friction level in order for the precursor to reach a certain distance towards the leading edge, and consequently a lower tangential load is needed. This effect is quite pronounced here because the vertical dimension is not explicitly taken into account. It is, however, reasonable to believe that this effect will also be present in a three-dimensional model, but to a lesser extent because of the possibility of force transfer through the bulk.

Instead of plotting the length of a precursor, the size of a precursor could be used. The size of a precursor is defined as the fraction of the number of blocks that participated in the event. This would then correspond to the size of the region in which the local area of contact changed during the event. The size of the precursors is plotted in Figure 7.9b as a function of the tangential load. The difference between the point and side driven model are now significantly reduced. This can be understood by considering the shear force profiles. Each block that has moved has a shear force approximately equal to the dynamic friction level. Consequently, the static friction force on each block is also approximately equal to the dynamic friction level when the system is not moving. The sum of all external forces in any stick interval is zero, meaning that the driving force equals the sum of the static friction forces. This means that, for a given tangential

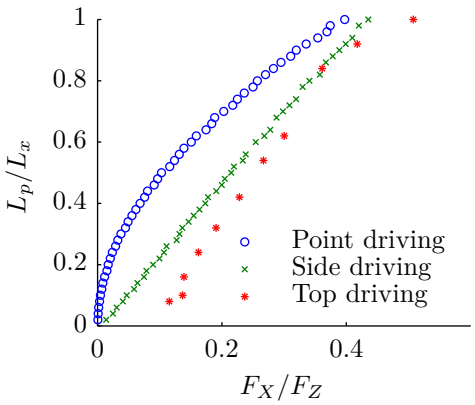

(a) The length of precursors as a function of the tangential load for the two-dimensional model with point, side and top driving.

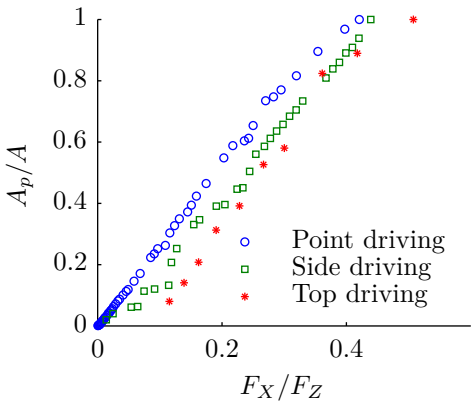

(b) The size of precursors as a function of the tangential load for the two-dimensional model with point, side and top driving.

Figure 7.9: The length and size of precursors as a function of the tangential load for the two-dimensional model. The differences between side driving and the point driving are significantly reduced when using the size instead of the length. For the top driving $\theta = 0.833$ was used, while $N_x = N_y = 50$ for all simulations, and other parameters are as in Table 7.1.

load F_X and fixed static and dynamic friction levels, approximately the same number of blocks has a shear force equal to the dynamic friction level. Consequently, approximately the same number of blocks has moved for a given F_X for the side and point driving.

7.7 System size and two-dimensional effects

As a last result from the (2 + 0)D model, the size of the slider as a function of time is shown in Figure 7.10 for side driving. As in the one-dimensional models, the slider is compressed in the x-direction during the precursor phase. Because of the Poisson effect, this causes an expansion in the y-direction. The system then reaches its final size approximately when the first global event occurs.

In Figure 7.11, the strain ratio is plotted as a function of time. The green line is the value of Poisson's ratio in the infinite system, $\nu = 1/3$. This situation is somewhat different from that considered in section 7.5.2: the tangential force F_X is now opposed by the friction forces distributed among all the blocks. Despite this, the strain ratio is seen to be approximately equal to Poisson's ratio after the first global event has occurred.

7.8 Robustness of the results

The results obtained for the two-dimensional model are equally robust as the results obtained for the one-dimensional model. Again the local dynamic friction coefficient is seen to determine the global static friction coefficient. A small randomness is now included in the friction coefficients (about 1.5 % of the value of μ_s and 2 % of the value of μ_d), and the results have been observed not to change significantly if the variation in

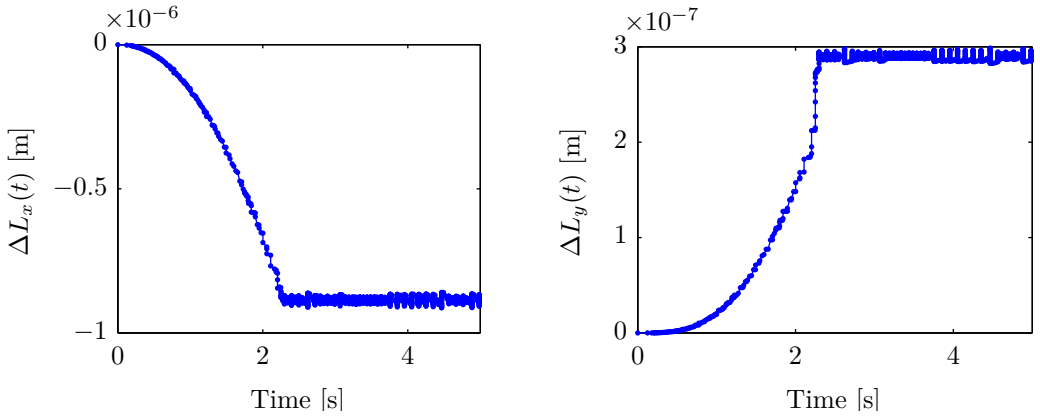

(a) Sample length in the x-direction as a function of time.

(b) Sample length in the y-direction as a function of time.

Figure 7.10: These figures show the time development of the sample length for the side driven $(2 + 0)$D model. $\Delta L_x(t)$ and $\Delta L_y(t)$ are the differences between the length at a given time t and the initial length in the corresponding dimension. This time development is a consequence of the Poisson effect.

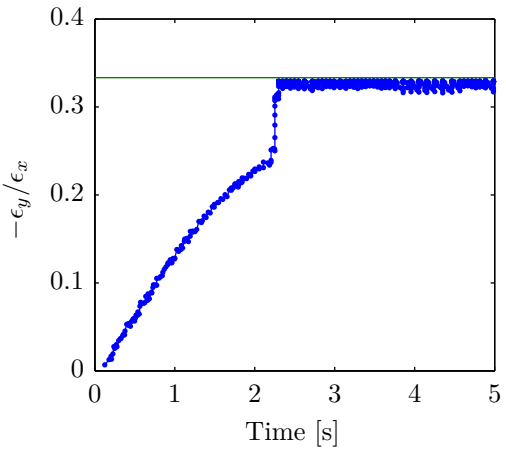

Figure 7.11: The ratio of the strains in the y- and x-direction as a function of time. Surprisingly it stabilises close to the Poisson ratio $\nu = 1/3$ (green line).

the local friction coefficients is increased, as long as the variation is not about the size of the friction coefficients themselves. As stated above, the results do not seem to be highly dependent on the value of η. As long as the driving spring is soft ($K \ll k$) and the driving velocity is low, similar results are obtained.

7.9 Summary and conclusion

In this chapter, a $(2 + 0)$D model has been presented, analysed and compared to the one-dimensional model. It has been shown that for side and top driving, the results from the two-dimensional model are very similar to that obtained for the one-dimensional model. This is caused by the fact that all blocks are still in frictional contact with the track, and are therefore either moving or not moving. Force transfer through the bulk is still not possible.

The results are, however, quite different from those obtained from the one-dimensional model if there is a heterogeneity in the driving, i.e. if the system is driven by a point instead of e.g. uniformly from the side. Fronts do not have to rupture the whole interface in the y-direction in order to propagate forwards, it is enough to break only a part of it.

The point driving is an example of such a heterogeneity. For this driving, which has no analogue in one dimension, some interesting effects were seen. The precursor front was not linear, but propagates radially out from the driven block(s). As a result, the length of precursors is dominated by the front propagating directly towards the leading edge, causing a significant altering of the $L_p(F_X)$-curve. However, considering the size of a precursor instead, this difference almost disappears.

Because of the lack of experiments studying effects in the second horizontal dimension, analysing the results of the (2 + 0)D model becomes more difficult. In addition, new measures are needed in order to study the effects of this dimension. A discussion of the (2 + 0)D model would therefore be more fruitful after experiments have been done focusing on these effects.

Chapter 8

Summary and conclusions

8.1 Summary

In this thesis, spring-block models have been used to shed light on recent experiments studying the transition from static friction to stick-slip motion. First, a one-dimensional model with Amontons–Coulomb friction was discussed. It was shown that many of the experimentally observed features, such as stick-slip behaviour and global ruptures preceded by precursor events initiating slip, are also present in the model. However, there were quite large discrepancies in the length of precursors as a function of applied tangential load and time dependence of slip.

The former was suggested to be caused by the lack of a vertical dimension. The reason for this was that including an initial shear force profile more like the one observed in experiments results in much better agreement, in addition to the fact that the slider used in the experiments looks rather two-dimensional. Since the length of precursors could be calculated from a purely geometrical argument, it was suggested that the specific dynamics of an event is not that important to the length of precursors. Rather, it is the fact that blocks end up at the dynamic friction level that is important. The latter was suggested to be a consequence of the simplified friction law used. The slip is thought to be a consequence of a local melting of the interface, which cannot be expected to be reproduced by a simple Amontons–Coulomb friction law.

The local rupture velocity has been shown to depend on the local shear to normal stress ratio in the experiments. Through both numerical and analytical studies, this was shown to be true also in the one-dimensional side driven model. For constant rupture velocities, there is a unique relationship between the local stress ratio and the rupture velocity:

$$\boxed{v_c = \frac{v_s}{\sqrt{1-\bar{\tau}^2}}, \qquad \bar{\tau} = \frac{\tau/\sigma - \mu_d}{\mu_s - \mu_d}.} \tag{8.1}$$

The parameter $\bar{\tau}$ shows that the rupture velocity also depends on the local strength of the interface, which in the model is represented by the friction coefficients. It also depends on the velocity of sound, which means that different materials will have different rupture velocities.

There was, of course, not a perfect agreement between experimental results and the model. In the model, velocities can get infinitely high, while they in experiments are

limited by the longitudinal wave speed. In addition, no slow ruptures were observed. The reasons for these discrepancies were suggested to be the limits of a one-dimensional model, which only has one type of sound wave while a three-dimensional system has two different kinds of bulk sound waves in addition to surface waves. In a one-dimensional model, waves can only travel in one direction, with the blocks moving along the same direction, which is not realistic. In addition, the friction law itself is too simple: it contains no slow time dynamics, which from recent modelling results appears to be important for slow fronts to appear.

The one-dimensional side-driven model with Amontons–Coulomb friction exhibited an unphysical scaling with respect to the model resolution, i.e. the number of blocks used, concerning the number of events, loading curve, duration of events and slip length in an event. The reason was found to be the highly singular driving that only affects the first block. By introducing a finite loading region by modifying the static friction law, it was shown that this problem could be significantly reduced. The finite loading region is a built in feature of (1 + 1)D and three-dimensional models, which then serves as yet another indication of the importance of dimensionality.

As mentioned above, the time dependence of slip was also shown to disagree with experimental results, and this does not improve when using the spring-to-track static friction law. The reason was suggested to lie in the dynamic friction law, and a new viscous law was introduced in order to get a more realistic slip. A slip in quite good agreement with the experimental results was obtained, showing that a pure viscous law with a time dependent viscosity is in fact sufficient to reproduce the measured slip function. However, it proved insufficient to get slow fronts, and other difficulties such as getting a good loading curve arose. This was suggested to originate in the coupling between the static and dynamic friction law, which were here applied independently of each other. The rupture phase is expected to be important to the dynamics, but no good experimental data for this short phase is available. In addition, no slow fronts are observed for precursor events, meaning that the mechanism behind slow fronts may not be present in the experimental slip data available.

A (2 + 0)D model with Amontons–Coulomb friction, where the second horizontal dimension is included instead of the vertical one, was also discussed. The analysis of this model proved to be difficult due to the lack of experimental data focusing on effects in these dimensions. New definitions of measures such as the length of precursors may be needed. It was shown by comparing the length and size of precursors that they can behave quite differently, depending on the driving. In addition, since all block are in frictional contact with the interface, the unphysical scaling with respect to the number of blocks is still present with both side and point driving.

Even though these models were compared to experiments studying friction between two blocks of PMMA, the results presented here should have a more general validity. Spring-block models are not limited to PMMA, but can be used to study other elastic materials as well.

8.2 Alternative approaches and future research

Dimensionality seems to be important to both kinetics and dynamics. In a (1 + 1)D model, it is possible to include much more realistic boundary conditions than in a one-dimensional model, e.g. how the tangential and normal loads are applied. This system has been studied in [56], and a detailed discussion will therefore not be given here. It would, however, be interesting to systematically investigate the consequences to the rupture velocities. The analysis will certainly be more demanding than in a one-dimensional model, but the results given here suggests that it might be essential in order to get realistic dynamics.

Many different friction laws have been used in combination with spring-block models. In the Burridge–Knopoff model, especially slip and velocity dependent friction laws are widely used [21, 22]. The dynamics of the system, including the rupture velocities, are highly dependent on the friction law. Applying different friction laws is therefore one approach that could be taken in future research. What is the effect of different friction laws on the dynamics? What features does a friction law need in order for slow ruptures to occur except a time dependence? Maybe a time dependence is not needed after all? What are the similarities and differences between the slip nucleation front and the slip arrest front?

The local friction law is also important for the time development of slip. From the experimental data, the slip appears to be rather robust, i.e. there are no large variations in the observed behaviour. This robustness should be a property of a future friction law aiming at describing the physical processes causing friction.

The importance of inertia in the model has not been addressed in this work. For example, the length of precursors appears to be dependent only on the normal loading and the local dynamic friction coefficient. The mass of the slider does not seem to be important. Does this mean that a model without inertia would be sufficient to study the length of precursors? Could the length of precursors then be predicted from elasticity theory?

The spring-block approach has proven itself to be applicable to modelling the onset of dynamic friction. It can be used to study both kinetics and dynamics, and it is a rather simple model that is easy to implement on a computer. However, the models used here only relate the mesoscopic scale to the macroscopic scale. It is the local friction law that couples the model to the microscopic processes causing friction, and it has to be imposed explicitly.

As with most Master's theses, no ground breaking new discoveries have been made, but some valuable insights were nevertheless obtained, which can motivate further experimental studies. Firstly, an investigation of how the experimental results depend on the aspect ratio of the slider would be of interest. If the height of the slider is reduced, do the results become more similar to those obtained from the one-dimensional model for e.g. the length of precursors? A second possibility is to investigate how the rupture velocity depends on the local strength of the interface. Thirdly, it would be interesting to see experiments focusing on effects induced by the second horizontal dimension. In experiments so far, this dimension is averaged out, but as demonstrated by the (2 + 0)D model, several new features may be observed.

Using spring-block models are only one of several different approaches. Another possi-

bility is to use Finite Element Methods (FEM), where the elasticity equations for the material are solved for given boundary conditions, but this would not be a radically different approach. Examples of modelling activity not using spring-block models or FEM are that of Reguzzoni et al. [44] and Gerde and Marder [30]. The former uses a molecular dynamics approach, while the latter uses a multiscale analysis technique.

8.3 Conclusions and ending remarks

As mentioned in the introduction to this thesis, friction is a multiscale problem: how effects at different (micro-, meso- and macroscopic) scales relate to each other are still unclear. Determining this is a crucial part of understanding the friction phenomenon. When looking back at the questions posed in the introduction, none of these have been answered in this thesis. What have been done, however, is to shed some light on the recent experimental results: the importance of e.g. dimensionality on kinetics, and prestress, interfacial strength (i.e. the local friction law) and dimensionality on dynamics. This interplay between theory and experiments is what one day hopefully results in a complete understanding of friction.

Working on this thesis for the past year has been a very rewarding experience, and collaborating closely with Jørgen and Kjetil has been a pleasure. Our work has contributed to the article "Transition from static to kinetic friction: insights from a 2D model", now available on arXiv [55], which mostly presents Jørgen's findings in his (1 + 1)D model. It is with both relief and a touch of sadness that I with these words end my Master's thesis.

Appendices

Appendix A

Additional details of the one-dimensional model

A.1 Relative viscous damping

The value of η should be chosen to minimise the undesired oscillations, but it should not alter the dynamics of the system to a great extent. In order to determine what value of η that should be chosen, an analytical analysis of systems with viscous damping is done. The first system studied is a one block system. Concepts introduced there are then used to analyse a chain of blocks. The result is a suggested value of η that should satisfy the above criteria.

A.1.1 Viscous damping in a one block system

The viscous damping terms considered in this thesis are of the simplest form: directly proportional to the velocity of the block. Consider the one block system depicted in Figure A.1. A block with mass m is attached to a wall on each side through springs with spring constants k. There is no friction between the block and the interface, but there is a viscous damping force proportional to the velocity of the block. This can be thought of as either a relative damping or an absolute damping since the walls are stationary.

The equation of motion for this system is given by

$$\ddot{u}(t) + \frac{\eta}{m}\dot{u}(t) + 2\frac{k}{m}u(t) = 0, \tag{A.1}$$

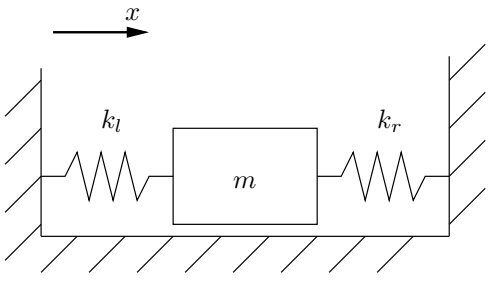

Figure A.1: A simple system consisting of one block connected to a wall at both sides by springs with spring constant k. This system is useful when considering the time step and the viscous damping.

where η is the damping coefficient. This is a homogeneous linear ordinary differential equation that can be solved by using the characteristic polynomial. It can also be solved by assuming a solution on the form

$$u(t) = e^{-\nu t}\left(Be^{i\omega t} + Ce^{-i\omega t}\right), \tag{A.2}$$

where B and C are complex constants, and the real part of $u(t)$ is considered to be the physical solution. Actually, it is enough to consider the less general solution of the form

$$u(t) = e^{-\nu t}e^{i\omega t} \tag{A.3}$$

for the purposes of this calculation. Inserting this solution into equation (A.1) yields the relations

$$\nu = \frac{\eta}{2m}, \tag{A.4}$$

$$\omega^2 = \frac{2k}{m} - \frac{\eta^2}{4m^2}. \tag{A.5}$$

As long as ω is real, the block will oscillate, but if ω is purely imaginary, the system will no longer oscillate. At the intersection between these two behaviours, i.e. at $\omega = 0$, the system is critically damped. No oscillations will occur, but infinitesimally smaller damping will cause oscillations with a very small frequency. The value of the damping parameter η for which the system is critically damped is

$$\eta = 2\sqrt{2}\sqrt{km}. \tag{A.6}$$

This derivation is only valid for a system consisting of one block, but gives valuable insight into how the damping affects the motion of this block. In the following, relative viscous damping in a chain of block is discussed.

A.1.2 Relative viscous damping in a chain of blocks

In this section, the strategy used for finding the value of η for critical damping is applied to an infinite chain of blocks. If friction forces are ignored, the equations of motion for this system are given by

$$m\ddot{u}_n = k(u_{n+1} - 2u_n + u_{n-1}) + \eta(\dot{u}_{n+1} - 2\dot{u}_n + \dot{u}_{n-1}). \tag{A.7}$$

By assuming a solution on the form

$$u_n(t) = e^{-\zeta_\kappa t}e^{i(\kappa n a - \omega_\kappa t)}, \tag{A.8}$$

equations for the characteristic damping time ζ_κ and the angular frequency ω_κ can be found corresponding to equations (A.4) and (A.5) for the one block system. The real solution to equation (A.7) is a sum over all wave numbers κ, but again, only a less general solution is needed here.

Inserting equation (A.8) into equation (A.7), yields the relation

$$m\zeta_\kappa^2 + 2im\zeta_\kappa\omega_\kappa - m\omega_\kappa^2 = k\left(e^{i\kappa a} - 2 + e^{-i\kappa a}\right) - \eta(\zeta_\kappa + i\omega_\kappa)\left(e^{i\kappa a} - 2 + e^{-i\kappa a}\right),$$

which can be simplified to

$$m\zeta_\kappa^2 + 2im\zeta_\kappa\omega_\kappa - m\omega_\kappa^2 = -4k\sin^2\left(\frac{\kappa a}{2}\right) + 4\eta(\zeta_\kappa + i\omega_\kappa)\sin^2\left(\frac{\kappa a}{2}\right),$$

since

$$e^{i\kappa a} - 2 + e^{-i\kappa a} = -4\sin^2\left(\frac{\kappa a}{2}\right).$$

The real and imaginary parts of can now be separated easily, which leads to

$$m\zeta_\kappa^2 - m\omega_\kappa^2 = -4(k - \eta\zeta_\kappa)\sin^2\left(\frac{\kappa a}{2}\right), \qquad 2m\alpha_\kappa\omega_\kappa = 4\eta\omega_\kappa\sin^2\left(\frac{\kappa a}{2}\right).$$

Solving these equations with respect to the characteristic damping time ζ_κ and the angular frequency ω_κ yields

$$\zeta_\kappa = 2\frac{\eta}{m}\sin^2\left(\frac{\kappa a}{2}\right), \tag{A.9}$$

$$\omega_\kappa^2 = 4\sin^2\left(\frac{\kappa a}{2}\right)\left(\frac{k}{m} - \frac{\eta^2}{m^2}\sin^2\left(\frac{\kappa a}{2}\right)\right). \tag{A.10}$$

This means that both the characteristic damping time and the angular frequency depend on the wave number κ. The artificial oscillations that are to be reduced have wavelength $\lambda = 2a$, leading to the wave number $\kappa = 2\pi/\lambda = \pi/a$. Inserting this into equation (A.10), setting $\omega_\kappa = 0$ and solving for η leads to

$$\eta = \sqrt{km}, \tag{A.11}$$

which is the value for the damping coefficient η for which waves of wavelength $\lambda = 2a$ are critically damped. Since $\sin^2$ is always smaller than one, choosing $\eta = \sqrt{km}$ will cause all other waves to be under-damped. However, waves of other wavelengths close to $\lambda = 2a$ will also be highly damped, causing significant changes to the dynamics. Since this is an undesirable effect, a compromise has to be made. As suggested by Knopoff and Ni [33], the value

$$\eta = \sqrt{0.1}\sqrt{km} \approx 0.32\sqrt{km} \tag{A.12}$$

is used in all simulations in this work unless otherwise stated.

A.2 Numerical aspects

In this section, the numerical aspects of solving the equations of motion are discussed. Firstly, how the integration time step is chosen is addressed, leading to the scaling in terms of CPU time of the program. Then the numerical scheme used for starting and stopping blocks moving on a one-dimensional surface is given. In addition, it turns out that by doing a simple calculation beforehand, the CPU time required to solve the equations of motion can be significantly reduced, which will also be discussed.

A.2.1 Integration time step and scaling

It is important to choose the integration time step Δt small enough in order to make the solution accurate and stable. The question is then: What does "small enough" mean? An indication of what the time step should be can be obtained from the solution of the equation of motion for a single block connected to springs on both sides, as shown in Figure A.1.

The springs cause harmonic oscillations with period $P = 2\pi/\omega$, where the angular frequency ω is given by equation (A.5). The integration time step Δt should be chosen much smaller than this period because a much higher time resolution than the period of oscillation is needed in order to resolve it:

$$\Delta t \ll P = 2\pi/\omega = 2\pi\sqrt{\frac{m}{2k}}, \tag{A.13}$$

where the damping term in ω has been ignored since only an upper estimate of ω is needed. Replacing the variables m and k by the total system variables by using the relations

$$m = M/N, \qquad k = (N-1)EA/L, \tag{A.14}$$

provides the scaling of the time step with the number of blocks N. The time step scales as

$$\Delta t \ll 2\pi\sqrt{\frac{LM/N}{(N-1)EA}} \sim \frac{1}{N}. \tag{A.15}$$

This means that the number of time steps needed to obtain the solution for a given time interval scales as N. In addition, at all time steps a loop over all blocks is needed in order to calculate the forces on all blocks. This means that the total computational effort scales as N^2, so if the number of blocks is doubled, four times more CPU time will be needed in order to solve the equations of motion for a given time interval.

A.2.2 How to start and stop a block moving on a 1D surface

According to Amontons–Coulomb's friction laws, a block starts to move when the sum of all forces, excepting the friction force, exceeds the static friction threshold. If the dynamic friction coefficient is smaller than the static one, as is normal, the block will immediately have non-zero acceleration in the direction of the sum of all forces on the block.

When solving the equations of motion numerically, the physical quantities are really only available at integer time steps. This means that in a numerical scheme, a block begins to experience dynamic friction in the time interval following the occurrence of a shear force greater than the static friction threshold. This leads to a small error in the numerical result, but this error will decrease as the integration time step is decreased.

The direction of the dynamic friction force is usually determined by the velocity, but at the time step where the friction law is changed, the velocity is still zero. The direction of the dynamic friction force is then chosen to be opposite of the sum of all other forces.

The criterion for changing from dynamic to static friction, that is how to stop a block already moving, is a little bit more difficult to handle. According to Amontons-Coulomb's

friction laws, a block will start experiencing a static friction force when its velocity is zero. In a numerical calculation, the velocity of a block will practically never be zero, but decrease towards zero and then change sign. Therefore, in a numerical calculation, a block will start experiencing a static friction force when the velocity changes sign between two time steps. This will also cause a slight error in the numerical calculation, but that will also decrease as the integration time step is decreased.

All these checks are done at integer time steps, which means that a block will always start and stop at the time step right after it should have in reality.

A.2.3 Skipping simulation of stick in intervals

When all blocks are experiencing a static friction force, no movement occurs. These time intervals are called stick intervals. The only thing happening is the increased load on the driven blocks due to the driving. In order to improve the efficiency of the program it is therefore advantageous to jump to the time where the first block starts to move because of the increased driving force. There is no point in integrating the equations of motion if it is known that no motion occurs at all.

It will be assumed that all blocks can potentially be driven, and that block n is driven by a spring with spring constant K_n resulting in the driving force

$$F_n^d(t) = K_n(Vt - u_n(t)). \tag{A.16}$$

It will also be assumed that the normal force on each block is given by

$$w_n(t) = w_n^{(0)} + \frac{g}{N}\left(\frac{2n-N-1}{N-1}\right)F_X, \tag{A.17}$$

where

$$F_X = \sum_{n'=1}^{N} F_{n'}^d(t) = \left(Vt\sum_{n'=1}^{N} K_{n'} - \sum_{n'=1}^{N} K_{n'}u_{n'}(t)\right)$$

and $w_n^{(0)}$ is given by equation (4.11):

$$w_n^{(0)} = \frac{F_Z}{N}\left(1 + \frac{2n-N-1}{N-1}\theta\right). \tag{A.18}$$

If all blocks have stopped at a time t^{stop}, the material spring forces are constant until a block starts to move because of the increased driving force. The viscous damping force is zero because all velocities are zero. The time t_n^{start} when block n starts to move because of driving alone can be calculated by using the forces at t^{stop}. At t_n^{start}, the sum of all forces except friction must be equal to the static friction threshold:

$$F_n^k(t^{\text{stop}}) + K_n\left(Vt_n^{\text{start}} - u_n(t^{\text{stop}})\right) = \mu_s w_n(t_n^{\text{start}}), \tag{A.19}$$

where $F_n^k(t^{\text{stop}})$ is the total force from neighbouring blocks on block n at the time t^{stop}. As mentioned, this does not change between t^{stop} and the time when the first block starts moving. Equation (A.17) can now be inserted into equation (A.19) and solved for t_n^{start}, resulting in the relation

$$t_n^{\text{start}} = \frac{K_n u_n(t^{\text{stop}}) - F_n^k(t^{\text{stop}}) + \mu_s\left(w_n^0 - \frac{g}{N}\left(\frac{2n-N-1}{N-1}\right)\sum_{n'=1}^{N} K_{n'}u_{n'}(t^{\text{stop}})\right)}{K_n V - \frac{g}{N}\left(\frac{2n-N-1}{N-1}\right)\mu_s V\sum_{n'=1}^{N} K_{n'}}. \tag{A.20}$$

In any stick interval, i.e. a time interval in which no blocks are moving, equation (A.20) can be used to calculate t_n^{start} for all blocks. The block with the lowest t_n^{start} starts to move first, and the program can then jump to this time and continue the integration of the equations of motion.

Appendix B

Additional details of the (2 + 0)D model

B.1 Calculation of Young's modulus and Poisson's ratio

In this section, equation (7.8) relating Young's modulus and Poisson's ratio to the material spring constants is derived. A force F is applied at the left- and right-hand side in opposite directions on the two-dimensional system depicted in Figure 7.1. The force F is distributed equally among the edge blocks, and a single edge block will then experience two forces of magnitude $F_1 = F/N_y$ directed oppositely of each other. If the system is very large, edge effects can be neglected. A single block inside the system is then affected by two forces of size F_1 in the x-direction with opposite signs. Considering a single block as depicted in Figure B.1, the springs 1, 2 and 8 have to hold a force F_1. Assuming l_1 to be the equilibrium lengths of the springs with spring constant k, this condition can be restated as the equation

$$F_1 = k\Delta x_1 + 2k'(r - \sqrt{2}l_1)\frac{l_1 + \Delta x_1}{r}, \quad r = \sqrt{(l_1 + \Delta x_1)^2 + (l_1 + \Delta y_1)^2}, \tag{B.1}$$

where Δx_1 and Δy_1 is the expansion of the springs in the x- and y-direction, respectively. In addition, there should be no net forces in the y-direction, meaning that the sum of the forces from springs 2, 3 and 4 should be zero. This gives the equilibrium equation

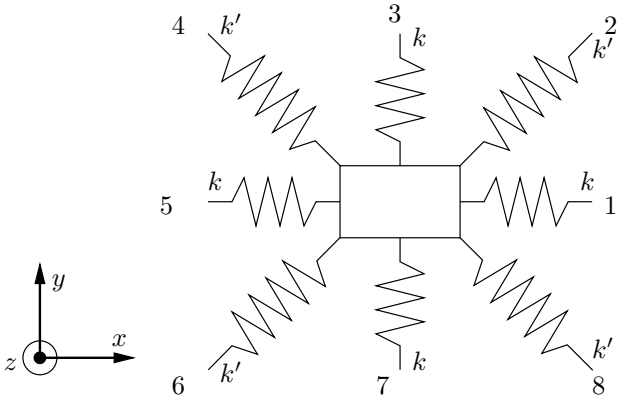

Figure B.1: Each block inside the system depicted in Figure 7.1 is connected to its neighbours by eight springs.

for the y-direction:

$$k\Delta y_1 + 2k'(r - \sqrt{2}l_1)\frac{l_1 + \Delta y_1}{r} = 0. \tag{B.2}$$

In order to find a relation between Young's modulus, Poisson's ratio and the spring constants, equations (B.1) and (B.2) have to be solved for $F_1(\Delta x_1)$ and $\Delta y_1(\Delta x_1)$. This is most easily done by Taylor expanding $r(\Delta x_1, \Delta y_1)$ and $1/r(\Delta x_1, \Delta y_1)$ about $(0, 0)$, assuming that Δx_1 and Δy_1 are small quantities compared to l_1:

$$r(\Delta x_1, \Delta y_1) = \sqrt{2}l_1 + \frac{1}{\sqrt{2}}(\Delta x_1 + \Delta y_1) + \frac{1}{4\sqrt{2}l_1}\left((\Delta x_1)^2 + (\Delta y_1)^2 - 2\Delta x_1 \Delta y_1\right) + \mathcal{O}(\Delta^3), \tag{B.3}$$

$$\frac{1}{r(\Delta x_1, \Delta y_1)} = \frac{1}{\sqrt{2}l_1} - \frac{1}{2\sqrt{2}l_1^2}(\Delta x_1 + \Delta y_1) + \frac{1}{8\sqrt{2}l_1^3}\left((\Delta x_1)^2 + (\Delta y_1)^2 + 6\Delta x_1 \Delta y_1\right) + \mathcal{O}(\Delta^3). \tag{B.4}$$

Inserting equation (B.3) and (B.4) into equation (B.2) yields

$$k\Delta y_1 + 2k'\left[\frac{1}{\sqrt{2}}(\Delta x_1 + \Delta y_1) + \frac{1}{4\sqrt{2}l_1}\left((\Delta x_1)^2 + (\Delta y_1)^2 - 2\Delta x_1 \Delta y_1\right) + \mathcal{O}(\Delta^3)\right] \times (l_1 + \Delta y_1)\left[\frac{1}{\sqrt{2}l_1} - \frac{1}{2\sqrt{2}l_1^2}(\Delta x_1 + \Delta y_1) + \frac{1}{8\sqrt{2}l_1^3}\left((\Delta x_1)^2 + (\Delta y_1)^2 + 6\Delta x_1 \Delta y_1\right) + \mathcal{O}(\Delta^3)\right] = 0. \tag{B.5}$$

Keeping only the first order terms and solving for Δy_1 yields

$$\Delta y_1(\Delta x_1) = -\frac{k'}{k + k'}\Delta x_1 + \mathcal{O}((\Delta x_1)^2). \tag{B.6}$$

Now, inserting equations (B.3) and (B.4) into equation (B.1) in the same way, keeping only first order terms, and solving for $F_1(\Delta x_1, \Delta y_1)$, leads to the relation

$$F_1(\Delta x_1, \Delta y_1) = k\Delta x_1 + k'(\Delta x_1 + \Delta y_1) + \mathcal{O}(\Delta^2). \tag{B.7}$$

Combining equations (B.6) and (B.7), a first order approximation to $F_1(\Delta x_1)$ can be found, resulting in

$$F_1(\Delta x_1) = \left(\frac{k^2 + 2kk'}{k + k'}\right)\Delta x_1 + \mathcal{O}((\Delta x_1)^2). \tag{B.8}$$

In a very large system, the total force is given by $F = F_1 N_y$, and the total displacement in the x-direction is given by $\Delta x = N_x \Delta x_1$. Young's modulus E and Poisson's ratio ν is related to the total force F and displacement Δx by the relations

$$E = \frac{F/(L_y L_z)}{\Delta x / L_x}, \qquad \nu = -\frac{\Delta y / L_y}{\Delta x / L_x}, \tag{B.9}$$

which give the following relations between k, k', E and ν:

$$E = \frac{k^2 + 2kk'}{k + k'} \frac{1}{L_z}, \tag{B.10}$$

$$\nu = \frac{k'}{k + k'}. \tag{B.11}$$

By inserting the relation $k = 2k'$ into equation (B.11), the result from [38] given in equation (7.8) is obtained.

B.2 Numerical aspects

In this section, some numerical details on solving the equations of motion numerically are given. This includes the starting and stopping of blocks, skipping stick intervals, how to choose the time step and the scaling in terms of CPU time.

B.2.1 Integration time step and scaling

The integration time step Δt again has to be chosen much less than the period of oscillation for the system. This is done in the same way as discussed in section A.2.1, where the spring constant in equation (A.15) now has to be approximated. Since only an overestimate is necessary, the sum of k and k' can be used in place of k in equation (A.15).

As seen from equation (7.8), the spring constants k and k' do not scale with the number of blocks N in the two-dimensional system. The mass m in equation (A.15) still scales as $1/N$, or as $1/N_x^2$, where N_x is the number of blocks in the x-direction. The final algorithm will therefore scale as N_x^2, just as the one-dimensional model.

B.2.2 How to start and stop a block moving on a 2D surface

Starting a block on a 2D surface according to the Amontons–Coulomb friction law is done in the same way as for the one-dimensional model, described in Appendix A.2, but where forces and velocities now are vectors and not scalars. This means that it is the length of the total force vector that has to be compared to the maximum local static friction $\mu_s w_n$.

The criterion for changing from dynamic friction to static friction, which was in the one-dimensional case that the velocity of a block changed sign, cannot be applied directly in this two-dimensional model because the velocity now has two components. A numerical scheme that is able to determine if the block velocity should have been zero between two time steps then has to be found.

Several different scenarios are depicted in Figure B.2, where the velocity at the beginning of the integration time step, $\mathbf{v}(t)$, is shown as empty circles, and the velocity at the end of the integration interval, $\mathbf{v}(t + \Delta t)$, is shown as filled circles. A straight line is then drawn between these two velocities as an approximation of the path in the (v_x, v_y)-space the block has followed.

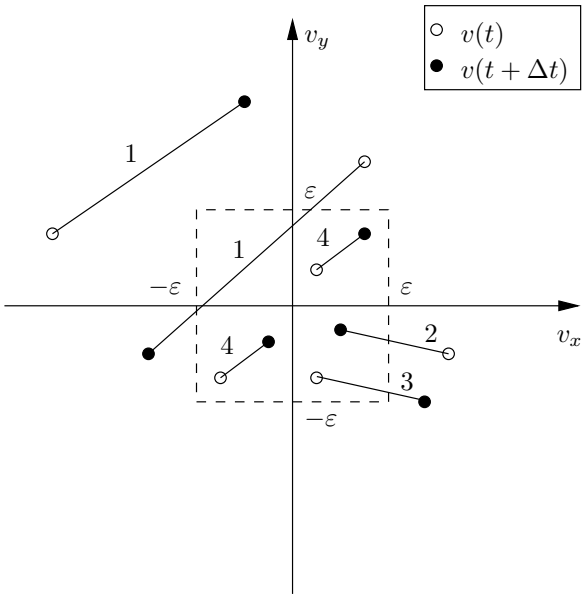

Figure B.2: This figure shows the different possible scenarios for how the velocity of a block can change between two time steps. The square with sides of size 2ε centred in origin represents the tolerance region.

Each of the different scenarios is labelled by a number, and scenarios with equal labels have both points either inside or outside she square with sides 2ε. The different scenarios, and what to do in each of them are given by the following:

1. Both $\mathbf{v}(t)$ and $\mathbf{v}(t+\Delta t)$ are outside the square: Draw a straight line between them. If this line passes through the square, the block is stopped.
2. $\mathbf{v}(t)$ is outside, and $\mathbf{v}(t+\Delta t)$ is inside the square: The block is stopped.
3. $\mathbf{v}(t)$ is inside, and $\mathbf{v}(t+\Delta t)$ is outside the square: The block continues to move.
4. Both $\mathbf{v}(t)$ and $\mathbf{v}(t+\Delta t)$ are inside the square: The block is only stopped if $|\mathbf{v}(t+\Delta t)| < |\mathbf{v}(t)|$ and the sum of all forces (except friction) on the block is less than the maximum static friction.

The reason for why the block in scenario 4 is only stopped if the sum of all forces (except friction) on the block is less than the static friction threshold is to avoid a situation where the block stops in one time step and then starts moving again in the next. The chosen value of the tolerance ε has to be reasonably small compared to the typical velocity of one block. In the results presented here, the value $\varepsilon = 1 \times 10^{-4}$ m/s was used.

The strategy given above is not ideal, and will cause errors in the numerical results. However, reducing the time step in addition to the tolerance ε should decrease these errors, and no large differences were seen in the results when doing this.

B.2.3 Skipping simulation of stick intervals

As for the one-dimensional model, there will be time intervals where no blocks are moving. Again, a formula for when block n starts to move because of driving alone can be obtained. The total force on block n excepting the friction force in a stick interval is given by

$$\mathbf{F}_n^{\text{n.f.}}(t) = \mathbf{F}_n^k(t^{\text{stop}}) + \mathbf{F}_n^K(t), \tag{B.12}$$

where $\mathbf{F}_n^k(t^{\text{stop}})$ is the total force from the material springs on block n at the time t^{stop} where the event ended, and $\mathbf{F}_n^K(t)$ is the driving force on block n given by equation (7.6). Decomposing $\mathbf{F}_n^{\text{n.f.}}$ into a component parallel to $\mathbf{V}$, and a component perpendicular to $\mathbf{V}$, results in

$$\mathbf{F}_n^{\text{n.f.}\parallel}(t) = \left[\mathbf{F}_n^k(t^{\text{stop}}) \cdot \hat{\mathbf{V}} + K_n(\mathbf{V}t + \mathbf{r}_n^0 - \mathbf{r}_n(t)) \cdot \hat{\mathbf{V}}\right] \hat{\mathbf{V}}, \tag{B.13}$$

$$\mathbf{F}_n^{\text{n.f.}\perp}(t) = \mathbf{F}_n^{\text{n.f.}}(t) - \mathbf{F}_n^{\text{n.f.}\parallel}(t) = \mathbf{F}_n^k(t^{\text{stop}}) - \left[\mathbf{F}_n^k(t^{\text{stop}}) \cdot \hat{\mathbf{V}}\right] \hat{\mathbf{V}}, \tag{B.14}$$

when the system is in a stick interval, where $\hat{\mathbf{V}} = \mathbf{V}/V$. As expected, the perpendicular component is independent of the driving force, since the driving force according to equation (7.6) only has a component parallel to $\mathbf{V}$. The time t_n^{start} when block n would begin to move because of the driving alone, can then be calculated from the relation

$$\left(\mathbf{F}_n^{\text{n.f.}\parallel}(t_n^{\text{start}})\right)^2 + \left(\mathbf{F}_n^{\text{n.f.}\perp}(t_n^{\text{start}})\right)^2 = (\mu_s w_n)^2,$$

and using equations (B.13) and (B.14), and solving for t yields

$$t_n^{\text{start}} = \frac{1}{KV}\left[\pm\sqrt{(\mu_s w_n)^2 - \left(\mathbf{F}_n^{\text{n.f.}\perp}(t_n^{\text{stop}})\right)^2} - \left(\mathbf{F}_n^k + K_n(\mathbf{r}_n^0 - \mathbf{r}_n(t^{\text{stop}})\right) \cdot \frac{\mathbf{V}}{V}\right]. \tag{B.15}$$

As discussed for the one-dimensional model, the block with the lowest t_n^{start} determines when the next event starts, and a simulation can therefore jump to this time.

B.2.4 Symmetry and numerical errors

For the driving mechanisms presented in section 7.2, the system is completely symmetric about an axis through the middle of the system parallel to the x-axis. In a real system this is of course not the case, since there will always be some impurities or defects.

In addition, errors caused by the numerical integration scheme will cause the system to loose this perfect symmetry after some time of simulation. This is caused by the fact that starting and stopping blocks is done in a very discrete way. At some point, blocks that should have started or stopped sliding at the exact same time end up doing so at times separated by a few time steps. This error will grow, causing the symmetry in the system to disappear.

Because of this issue, a small randomness in the friction coefficients is introduced. Each time a block starts or stops, a new dynamic or static friction coefficient is drawn from a uniform distribution centred around μ_d or μ_s with bounds ± 0.01. This randomness should then dominate over the errors in the integration scheme, and the system will be almost symmetric. The above scheme for skipping stick intervals can still be applied, but the static friction coefficient for block n has to be used in equation (B.15).

Bibliography

[1] D. J. Andrews. Rupture velocity of plane strain shear cracks. *J. Geophys. Res.*, 81(32):5679–5687, 1976. ISSN 0148-0227. doi: 10.1029/JB081i032p05679. URL http://dx.doi.org/10.1029/JB081i032p05679.

[2] T. Baumberger and C. Caroli. Solid friction from stick–slip down to pinning and aging. *Advances in Physics*, 55(3):279–348, 2006. ISSN 0001-8732. URL http://www.informaworld.com/10.1080/00018730600732186.

[3] T. Baumberger, P. Berthoud, and C. Caroli. Physical analysis of the state- and rate-dependent friction law. II. Dynamic friction. *Phys. Rev. B*, 60(6):3928–3939, Aug. 1999. doi: 10.1103/PhysRevB.60.3928.

[4] T. Baumberger, C. Caroli, and O. Ronsin. Self-healing slip pulses along a gel/glass interface. *Phys. Rev. Lett.*, 88(7):075509, Feb. 2002. doi: 10.1103/PhysRevLett.88.075509.

[5] O. Ben-David, G. Cohen, and J. Fineberg. The dynamics of the onset of frictional slip. *Science*, 330(6001):211–214, Oct. 2010. doi: 10.1126/science.1194777. URL http://www.sciencemag.org/cgi/content/abstract/330/6001/211.

[6] O. Ben-David, S. M. Rubinstein, and J. Fineberg. Slip-stick and the evolution of frictional strength. *Nature*, 463(7277):76–79, Jan. 2010. ISSN 0028-0836. doi: 10.1038/nature08676. URL http://dx.doi.org/10.1038/nature08676.

[7] R. Bennewitz, J. David, C.-F. de Lannoy, B. Drevniok, P. Hubbard-Davis, T. Miura, and O. Trichtchenko. Dynamic strain measurements in a sliding microstructured contact. *Journal of Physics: Condensed Matter*, 20(1):015004, 2008. URL http://stacks.iop.org/0953-8984/20/i=1/a=015004.

[8] P. Berthoud, T. Baumberger, C. G'Sell, and J.-M. Hiver. Physical analysis of the state- and rate-dependent friction law: Static friction. *Phys. Rev. B*, 59(22):14313–14327, June 1999. doi: 10.1103/PhysRevB.59.14313.

[9] E. Bouchbinder, E. A. Brener, I. Barel, and M. Urbakh. Cracklike dynamics at the onset of frictional sliding. *ArXiv e-prints*, Mar. 2011. URL http://arxiv.org/abs/1103.3942v1.

[10] F. P. Bowden and D. Tabor. *The Friction and Lubrication of Solids*. Clarendon Press, Oxford, 2001. First published 1950.

[11] W. F. Brace and J. D. Byerlee. Stick-slip as a mechanism for earthquakes. *Science*, 153(3739):990–992, 1966. ISSN 00368075. URL http://www.jstor.org/stable/1719360.

[12] O. M. Braun and M. Peyrard. Modeling friction on a mesoscale: Master equation for the earthquakelike model. *Phys. Rev. Lett.*, 100(12):125501, Mar. 2008. doi: 10.1103/PhysRevLett.100.125501.

[13] O. M. Braun and M. Peyrard. Master equation approach to friction at the mesoscale. *Phys. Rev. E*, 82(3):036117, Sept. 2010. doi: 10.1103/PhysRevE.82.036117.

[14] O. M. Braun and M. Peyrard. Dependence of kinetic friction on velocity: Master equation approach. *Phys. Rev. E*, 83(4):046129, Apr. 2011. doi: 10.1103/PhysRevE.83.046129.

[15] O. M. Braun and J. Röder. Transition from stick-slip to smooth sliding: An earthquakelike model. *Phys. Rev. Lett.*, 88(9):096102, Feb. 2002. doi: 10.1103/PhysRevLett.88.096102.

[16] O. M. Braun, I. Barel, and M. Urbakh. Dynamics of transition from static to kinetic friction. *Phys. Rev. Lett.*, 103(19):194301, Nov. 2009. doi: 10.1103/PhysRevLett.103.194301.

[17] H. D. Brewer. *Fluid Mechanics*. Oxford Book Company, Jaipur, India, first edition, 2009.

[18] R. Burridge. Admissible speeds for plane-strain self-similar shear cracks with friction but lacking cohesion. *Geophysical Journal of the Royal Astronomical Society*, 35(4):439–455, 1973. ISSN 1365-246X. doi: 10.1111/j.1365-246X.1973.tb00608.x. URL `http://dx.doi.org/10.1111/j.1365-246X.1973.tb00608.x`.

[19] R. Burridge and L. Knopoff. Model and theoretical seismicity. *Bulletin of the Seismological Society of America*, 57(3):341–371, 1967. URL `http://www.bssaonline.org/cgi/content/abstract/57/3/341`.

[20] J. M. Carlson. Two-dimensional model of a fault. *Phys. Rev. A*, 44(10):6226–6232, Nov. 1991. doi: 10.1103/PhysRevA.44.6226.

[21] J. M. Carlson and J. S. Langer. Mechanical model of an earthquake fault. *Phys. Rev. A*, 40(11):6470–6484, Dec. 1989. doi: 10.1103/PhysRevA.40.6470.

[22] J. M. Carlson, J. S. Langer, B. E. Shaw, and C. Tang. Intrinsic properties of a Burridge–Knopoff model of an earthquake fault. *Phys. Rev. A*, 44(2):884–897, July 1991. doi: 10.1103/PhysRevA.44.884.

[23] J. M. Carlson, J. S. Langer, and B. E. Shaw. Dynamics of earthquake faults. *Reviews of Modern Physics*, 66(2):657–670, Apr. 1994. ISSN 0034-6861.

[24] A. Chateauminois, C. Fretigny, and L. Olanier. Friction and shear fracture of an adhesive contact under torsion. *Phys. Rev. E*, 81(2):026106, Feb. 2010. doi: 10.1103/PhysRevE.81.026106.

[25] S. Ciliberto and C. Laroche. Energy dissipation in solid friction. *The European Physical Journal B - Condensed Matter and Complex Systems*, 9:551–558, 1999. ISSN 1434-6028. doi: 10.1007/s100510050795. URL `http://dx.doi.org/10.1007/s100510050795`.

[26] S. Das. Earthquake supershear rupture speeds. *Tectonophysics*, 493(3-4):213 –

215, 2010. ISSN 0040-1951. doi: 10.1016/j.tecto.2010.07.009. URL http://www.sciencedirect.com/science/article/pii/S0040195110002970.

[27] D. Dawson. *History of Tribology*. Professional Engineering Publishing Limited, London and Bury St Edmunds, UK, second edition, 1998.

[28] J. H. Dieterich and B. D. Kilgore. Direct observation of frictional contacts: New insights for state-dependent properties. *Pure and Applied Geophysics*, 143:283–302, 1994. ISSN 0033-4553. doi: 10.1007/BF00874332. URL http://dx.doi.org/10.1007/BF00874332.

[29] A. E. Filippov, J. Klafter, and M. Urbakh. Friction through dynamical formation and rupture of molecular bonds. *Phys. Rev. Lett.*, 92(13):135503, Mar. 2004. doi: 10.1103/PhysRevLett.92.135503.

[30] E. Gerde and M. Marder. Friction and fracture. *Nature*, 413(6853):285–288, Sept. 2001. ISSN 0028-0836. doi: 10.1038/35095018. URL http://dx.doi.org/10.1038/35095018.

[31] J. A. Greenwood and J. B. P. Williamson. Contact of nominally flat surfaces. *Proceedings of the Royal Society of London, Series A, Mathematical and Physical Sciences*, 295(1442):300–319, 1966. doi: 10.1098/rspa.1966.0242. URL http://rspa.royalsocietypublishing.org/content/295/1442/300.abstract.

[32] C. Kittel. *Introduction to Solid State Physics*. John Wiley & Sons, Inc, Hoboken, eighth edition, 2005.

[33] L. Knopoff and X. X. Ni. Numerical instability at the edge of a dynamic fracture. *Geophysical Journal International*, 147(3):1–6, 2001. ISSN 1365-246X. doi: 10.1046/j.1365-246x.2001.01567.x. URL http://dx.doi.org/10.1046/j.1365-246x.2001.01567.x.

[34] L. Knopoff, J. O. Mouton, and R. Burridge. The dynamics of a one-dimensional fault in the presence of friction. *Geophysical Journal of the Royal Astronomical Society*, 35(1-3):169–184, 1973. ISSN 1365-246X. doi: 10.1111/j.1365-246X.1973.tb02420.x. URL http://dx.doi.org/10.1111/j.1365-246X.1973.tb02420.x.

[35] H. Kobayashi, H. Takahashi, and Y. Hiki. Viscosity measurement of organic glasses below and above glass transition temperature. *Journal of Non-Crystalline Solids*, 290(1):32 – 40, 2001. ISSN 0022-3093. doi: DOI:10.1016/S0022-3093(01)00708-6. URL http://www.sciencedirect.com/science/article/B6TXM-43TRMJ4-5/2/966aa4700109c26510194c9ad57238cd.

[36] T. Lindstrøm. *Kalkulus*. Universitetsforlaget, Oslo, third edition, 2006.

[37] S. Maegawa, A. Suzuki, and K. Nakano. Precursors of global slip in a longitudinal line contact under non-uniform normal loading. *Tribology Letters*, 38(3):313–323, June 2010. ISSN 1023-8883. doi: 10.1007/s11249-010-9611-7. URL http://dx.doi.org/10.1007/s11249-010-9611-7.

[38] L. Monette and M. P. Anderson. Elastic and fracture properties of the two-dimensional triangular and square lattices. *Modelling and Simulation in Materials Science and Engineering*, 2(1):53, 1994. URL http://stacks.iop.org/0965-0393/2/i=1/a=004.

[39] C. B. Muratov. Traveling wave solutions in the Burridge–Knopoff model. *Phys. Rev. E*, 59(4):3847–3857, Apr. 1999. doi: 10.1103/PhysRevE.59.3847.

[40] B. N. J. Persson. Theory of friction: The role of elasticity in boundary lubrication. *Phys. Rev. B*, 50(7):4771–4786, Aug. 1994. doi: 10.1103/PhysRevB.50.4771.

[41] B. N. J. Persson. Theory of friction: Stress domains, relaxation, and creep. *Phys. Rev. B*, 51(19):13568–13585, May 1995. doi: 10.1103/PhysRevB.51.13568.

[42] B. N. J. Persson. *Sliding Friction*. Springer, Berlin, 1998.

[43] W. H. Press, S. A. Teukolsky, W. T. Vetterling, and B. P. Flannery. *Numerical Recipes*. Cambridge University Press, New York, third edition, 2007.

[44] M. Reguzzoni, M. Ferrario, S. Zapperi, and M. Righi. Onset of frictional slip by domain nucleation in adsorbed monolayers. *Proceedings of the National Academy of Sciences*, 107(4):1311, 2010.

[45] S. M. Rubinstein, G. Cohen, and J. Fineberg. Detachment fronts and the onset of dynamic friction. *Nature*, 430(7003):1005–1009, Aug. 2004. ISSN 0028-0836. doi: 10.1038/nature02830. URL `http://dx.doi.org/10.1038/nature02830`.

[46] S. M. Rubinstein, M. Shay, G. Cohen, and J. Fineberg. Crack-like processes governing the onset of frictional slip. *International Journal of Fracture*, 140: 201–212, 2006. ISSN 0376-9429. doi: 10.1007/s10704-006-0049-8. URL `http://dx.doi.org/10.1007/s10704-006-0049-8`.

[47] S. M. Rubinstein, G. Cohen, and J. Fineberg. Dynamics of precursors to frictional sliding. *Phys. Rev. Lett.*, 98(22):226103, June 2007. doi: 10.1103/PhysRevLett.98.226103.

[48] S. M. Rubinstein, G. Cohen, and J. Fineberg. Visualizing stick–slip: Experimental observations of processes governing the nucleation of frictional sliding. *Journal of Physics D: Applied Physics*, 42(21):214016, 2009. URL `http://stacks.iop.org/0022-3727/42/i=21/a=214016`.

[49] J. Scheibert and D. K. Dysthe. Role of friction-induced torque in stick-slip motion. *Europhysics Letters*, 92(5):54001, 2010. URL `http://stacks.iop.org/0295-5075/92/i=5/a=54001`.

[50] J. Scheibert, G. Debregeas, and A. Prevost. Micro-slip field at a rough contact driven towards macroscopic sliding. *ArXiv e-prints*, Sept. 2008. URL `http://arxiv.org/abs/0809.3188v1`.

[51] C. H. Scholz. *The Mechanics of Earthquakes and Faulting*. Cambridge University Press, Cambridge, second edition, 2002.

[52] Z. Shi, Y. Ben-Zion, and A. Needleman. Properties of dynamic rupture and energy partition in a solid with a frictional interface. *Journal of the Mechanics and Physics of Solids*, 56(1):5–24, Jan. 2008. ISSN 0022-5096. doi: 10.1016/j.jmps.2007.04.006.

[53] K. Thøgersen. Modeling the onset of dynamic friction: Contact mechanics. Master's thesis, University of Oslo, Oslo, 2011.

[54] S. P. Timoshenko and J. N. Goodier. *Theory of Elasticity*. McGraw-Hill, Singapore, third edition, 1970. First published 1934.

[55] J. Trømborg, J. Scheibert, D. S. Amundsen, K. Thøgersen, and A. Malthe-Sørenssen. Transition from static to kinetic friction: insights from a 2D model. *ArXiv e-prints*, May 2011. URL `http://arxiv.org/abs/1105.3325v1`.

[56] J. Trømborg. Modelling the onset of dynamic friction: Importance of the vertical dimension. Master's thesis, University of Oslo, Oslo, 2011.

[57] M. Urbakh, J. Klafter, D. Gourdon, and J. Israelachvili. The nonlinear nature of friction. *Nature*, 430(6999):525–528, July 2004. ISSN 0028-0836. doi: 10.1038/nature02750. URL `http://dx.doi.org/10.1038/nature02750`.

[58] F. Wu-Bavouzet, J. Cayer-Barrioz, A. Le Bot, F. Brochard-Wyart, and A. Buguin. Effect of surface pattern on the adhesive friction of elastomers. *Phys. Rev. E*, 82 (3):031806, Sept. 2010. doi: 10.1103/PhysRevE.82.031806.

[59] H. D. Young and R. A. Freedman. *University Physics with Modern Physics*. Addison Wesley, San Francisco, eleventh edition, 2004.